Polytechnic University of Marche
Ph.D. School in Engineering Sciences
Curriculum in Civil, Environmental, Building Engineering and Architecture

A proposal of damage identification and quantification for unreinforced and reinforced masonry structures

Ph.D. Dissertation of:

Ersilia Giordano

Advisor:

Prof. Stefano Lenci

Co-Advisor:

Prof. Francesco Clementi

Prof. José Miguel Adam

Prof. Maria Giovanna Masciotta

Curriculum supervisor:

Prof. Francesco Fatone

XXXIII Cycle

Università Politecnica delle Marche

Dipartimento di Ingegneria Civile, Edile ed Architettura

Via Brecce Bianche — 60131 - Ancona, Italy

Abstract

This thesis work presents the research path that allowed to identify a damage index applicable to structures unreinforced and reinforced with TRM.

To achieve this goal, a survey was first conducted on the ability of the TRM to improve the response of masonry structures using both experimental tests and numerical models. The microscopic behaviour of this composite was studied using qualification tests. With these tests, a sensitivity analysis was also carried out to evaluate which modelling approach is the most appropriate to model it on a structure. Subsequently, the efficiency of the reinforcement was investigated through two different experiments:

(i) pseudo-dynamic tests on a U-shaped masonry structure, carried out first on the as-built structure and then on the reinforced structure (tests carried out in the ICITECH laboratory of the University of Valencia)
(ii) pseudo-static tests on differently reinforced adobe arches (tests conducted in the ISISE laboratory of the University of Minho).

Using these experimental results and crossing them with the respective numerical models, an attempt was made to calibrate a damage index. The tests that proved to be most adequate to pursue the aim are those on the arches. They allowed to follow the degradation of the stiffness and simultaneously identify the frequencies variations as the damage increased. The new damage index identified considers the bending moment as the main cause of damage to the arches; Starting from the bending stiffness, therefore, a damage index was developed as a function of the frequencies ratio between damaged and undamaged scenarios. The identified index was validated both through experimental and numerical data.

A proposal of damage identification and quantification for unreinforced and reinforced masonry structures

Abstract

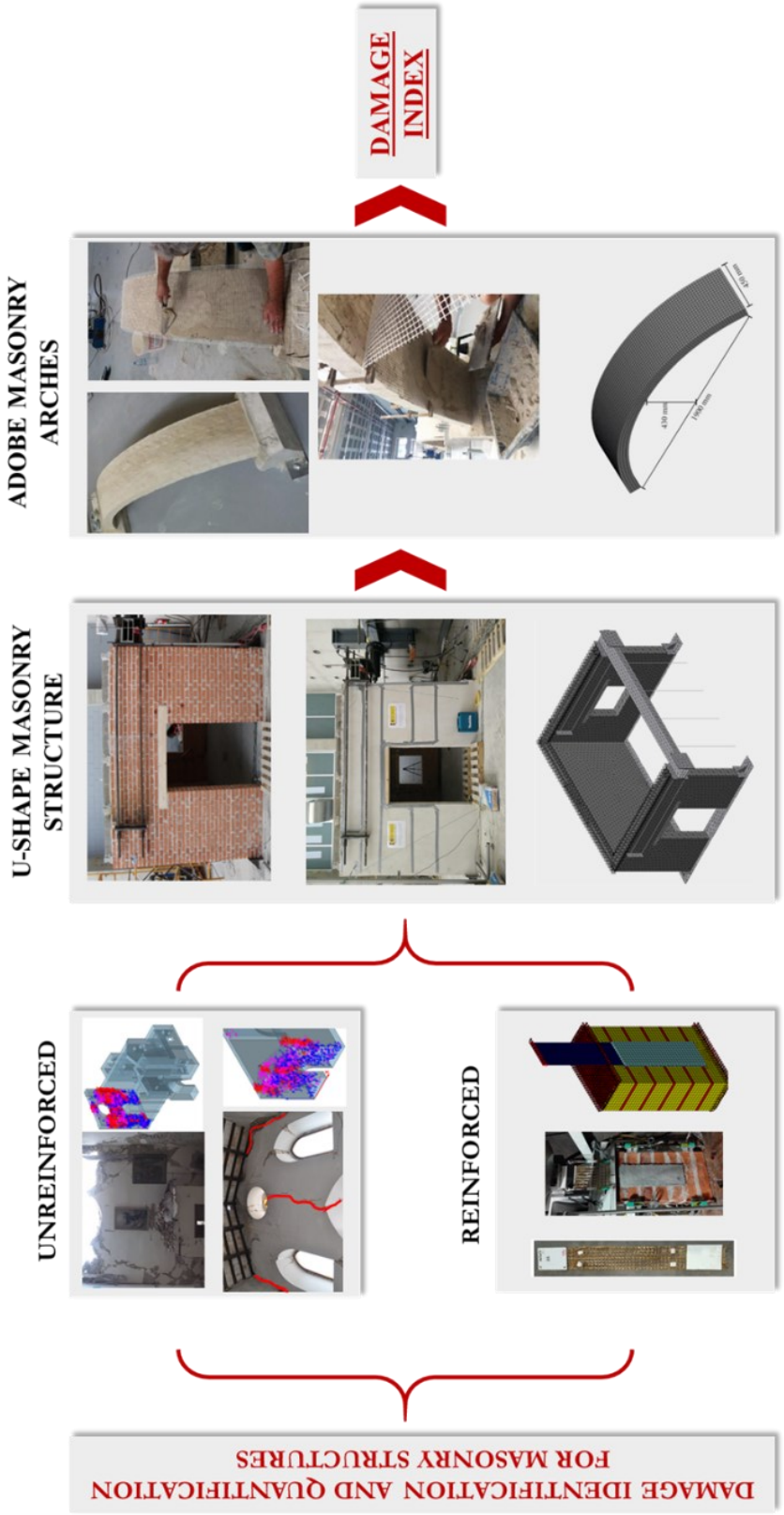

Sommario

Questo lavoro di tesi presenta il percorso di ricerca che ha permesso di individuare un indice di danneggiamento applicabile a strutture non rinforzate e rinforzate con il TRM.

Per raggiungere questo obiettivo, è stata prima condotta un'indagine sulla capacità del TRM di migliorare la risposta delle strutture in muratura utilizzando sia prove sperimentali che modelli numerici. Il comportamento microscopico di questo composito è stato studiato utilizzando test di qualificazione. Con questi test è stata effettuata anche un'analisi di sensitività per valutare quale approccio di modellazione sia il più appropriato per modellarlo su una struttura. Successivamente è stata indagata, invece, dell'efficienza del rinforzo attraverso due differenti sperimentazioni:

(i) prove pseudo dinamiche su una struttura in muratura ad U, realizzate prima sulla struttura as-built e poi sulla struttura rinforzata (prove effettuate nel laboratorio ICITECH dell'Università di Valencia)
(ii) prove pseudo-statiche su archi di mattoni diversamente rinforzati (prove condotte nel laboratorio ISISE dell'Università del Minho).

Utilizzando questi risultati sperimentali e incrociandoli con i rispettivi modelli numerici si è cercato di calibrare un indice di danno. Le prove che si sono rivelate più adeguate a perseguire lo scopo sono quelle sugli archi, in quanto consentivano di valutare il degrado della rigidezza e contemporaneamente identificare le variazioni delle frequenze all'evolvere del danno. Il nuovo indice di danno individuato considera il momento flettente come la principale causa di danneggiamento degli archi; A partire dalla rigidezza flessionale, quindi, è stato sviluppato un indice di danno funzione del rapporto delle frequenze tra scenari danneggiati e non danneggiati. L'indice individuato è stato validato sia attraverso dati sperimentali che numerici.

Acknowledgments

This thesis is the result of the collaboration between three European universities, the DICEA department of the Polytechnic University of Marche, the ICHITEC department of the Polytechnic University of Valencia, and the ISISE department of the University of Minho. In the first, I did most of my doctorate while the others hosted me in my experiences abroad. This Ph.D. has allowed me to meet many people that have helped me to grow both on a human and academic profile. Among all the people I met in these three years I would like to express my gratitude to:

- Professor Stefano Lenci for allowing me to participate in this doctorate
- Professor Francesco Clementi for believing in my abilities, for pushing me beyond my limits and for the interesting discussions
- Professor José Miguel Adam for welcoming me to the Polytechnic University of Valencia in the ICHITEC department and allowing me to analyze the data of a large-scale experiment
- Professor Maria Giovanna Masciotta for having acted as an intermediary for my second experience abroad at the University of Minho and helping me in the study of arches.
- To the Researchers Elisa Bertolesi and Manuel Buitrago for helping me in the elaboration of the data of the experimental and numerical tests on the U-Shape masonry structure and for making me discover the real Spain.
- To Researcher Nuno Mendes of the University of Minho for guiding me with patience and passion in the analysis of the experimental tests on masonry arches and for welcoming me into the great family of the UniMinho
- Professor Daniel V. Olivera and Professor Bahman Ghiassi for their support in the review of the final draft of this Dissertation and their useful advice to improve its quality
- To my office friend Angela Ferrante for sharing the joys and sorrows of this journey
- To all the Ph.D. colleagues who have followed one another in recent years for making all moments of conviviality pleasant and cheerful
- Finally, my family who continues to support and encourage me in my every decision

Index

List of figures

List of tables

Chapter 1: Introduction

1.1 General Framework and Motivation

Observing the damage suffered by many historical and monumental structures after the last seismic events, it is evident how the preservation of built heritage has become a fundamental issue [1,2]. Earthquakes turn out to be the main cause of serious damage, but not the only one, indeed even the exposition to environmental factors or new loading conditions can originate small cracks (at different levels) that can worsen into significant and irreversible damages. Thus, it is essential to elaborate easy and fast methods able to analyses in real or nearly-real time the structural capacity, to intervene promptly in case of damage onset, thereby avoiding expensive belated restoration works. A further essential requirement is that these methods must be minimally invasive to respect the historical value of the buildings. The technique that is becoming increasingly popular, to achieve this goal, is that of dynamic tests since the dynamic parameters of a structure are highly sensitive to mass and stiffness variations induced by damage [3]. The dynamic monitoring is normally performed using accelerometric sensors placed on significant points that record the vibrations of the structures under the environmental excitations. The signals thus acquired are subsequently cleaned, filtered, and analysed, or in the time or frequency domain, to extract the vibrational characteristics. Dynamic monitoring, if repeated over time, is called Structural Health Monitoring, since if a variation of these parameters is observed, it could be that the structure has suffered damage. Numerous researchers have researched a correlation between dynamic parameters and damage in all areas of engineering, eventually finding different modal-based damage indexes [4–7]. Damage Identification (DI) is a process of increasing complexity that entails four main levels: Detection, Localization, Assessment, and Prediction [8].

While the existence of damage (Detection) can be assessed by tracking the frequency values estimated from the vibration signals measured just by a reduced number of sensors, additional modal parameters like mode shapes are necessary to infer the position of damage (Localization), thereby a higher sensor density is demanded. Moreover, when frequency drops are considered, it is essential to get rid of possible temperature and humidity effects which can mask changes due to damage. Their influence can be removed using appropriate statistical tools applied to the recorded data [9,10]. The greater difficulty for the third level of DI (Assessment) lies in the necessity of accurate benchmark studies of similar elements/structures showing analogous vulnerabilities to

effectively infer a correlation between damage extent and dynamic parameters' variation. Finally, as far as the last level of DI is concerned, the complexity of the identification process increases owing to the need for analytical models that take into account the actual state of the structure as well as probabilistic models representative of the evolution of the structural behaviour considering the most likely damages that might occur.

The first applications of DI techniques were on steel and Reinforced-Concrete (RC) elements [11–14]. However, the last decade has been marked by an increasing interest to extend their applicability to masonry constructions [10,15–20]. The majority of studies conducted on real structures focused their attention on Level 1 DI methods, given the difficulties to perform extensive controlled testing campaigns and the consequent uncertainties for the application of higher-level DI methods. Laboratory tests can provide great advantages in this regard since it allowing to acquire a larger and replicable number of measurements in controlled environmental conditions for testing and validating even high-level DI methods.

The aim of this work is to enrich the database of vibration-based damage identification methods (VBDIMs) for masonry structures unreinforced and reinforced by elaborating an index that allows to globally identify and quantify the damage in masonry structures using only a few sensors. The main features that must distinguish the researched index from the others available in the literature are the simplicity of its formulation and the replicability, even by users without specific knowledge in the field.

To achieve the goal, two experimental tests were used: pseudo-dynamic tests of a U-Shape structure and pseudo-static tests on masonry arches, both performed on both non-reinforced and reinforced masonry with TRM (Texile-Reinforced-Mortar). The first test was used to investigate the ability of this type of reinforcement in improving the performance of masonry structures when subjected to seismic forces, while the second allowed, given the lack of complexity, to identify a damage index applicable to masonry arches.The arches are damaged up to collapse using pseudo-static test cycles carried out by applying progressive controlled displacements at third span. The test records allow to follow the stiffness degradation of each arch by plotting the relative force–displacement curves, as well as to track their frequencies variation during the damage evolution by means of dynamic identification tests performed at the end of each cycle. The new index considers the bending moment as the main cause of damage for the analysed arches;

therefore, starting from the bending stiffness, a damage indicator was developed and experimentally validated, as function of the frequency reduction, respect to the undamaged scenario. Finally, the index is also validated for different types of arch collapse mechanisms through Finite Element Modellings

1.2 Thesis structure

The thesis is organised in six Chapters, including this brief introduction:

• **Chapter 2** presents a brief summary of the mechanical characteristics of the masonry and of the behavior of unreinforced masonry structures under seismic loads. The different intervention techniques that can be used to improve the seismic response are also presented, starting from the most common ones up to the new development techniques that involve composite materials with cement mortar (TRM). Finally, the state of the art of vibration-based damage identification techniques is presented.

• **Chapter 3** presents a study aimed at identifying the most appropriate modelling of the TRM when it is applied to large-scale constructions. To pursue this aim, some qualification tests of the TRM with PBO fiber were used

• **Chapter 4** presents the description of the experimental tests and the numerical models of a U-Shape masonry building tested with pseudo-dynamic cycles of increasing displacements and frequencies. The sample was built at the ICITECH laboratory of the Universitat Politècnica de València to analyse the efficiency of TRM to improve the structure behaviour, indeed, the tests were done in two configurations without and with the reinforcement [21]. The results obtained underlined how the introduction of the TRM is able to significantly improve the seismic capacity of masonry structures. The experimental data were used to update a numerical model in order to identify a damage-index able to find and quantify the damage. However, the chapter shows that it was not possible due to many variables. “The experimental work described in this Chapter was funded by the Spanish Ministry of Economy, Industry and Competitiveness, Project BIA 2014-59036-R.”

• **Chapter 5** presents the process that allowed to identify a damage index for adobe arches. The data used to elaborate and validate the damage index were collected during eight pseudo-static displacement-controlled tests on the six adobe arches, carried out at the Structural Laboratory of the Civil Engineering Department of the University of Minho

(Portugal) [37]. The chapter describes the geometry of the specimens and the testing campaign and details the Ambient Vibration Tests (AVTs) performed to track the frequency variation after each induced damage scenario. The formulation of the damage index is also presented, demonstrating its direct relationship with the stiffness degradation of the arches obtained from the analysis of the experimental force-displacement curves. Finally, to verify the replicability and wide applicability of the proposed damage index, several numerical non-linear static analyses are performed and discussed, considering different types of arch collapse mechanisms.

• **Chapter 6** presents the main conclusions from each chapter and a proposal for future works.

Chapter 2: Literature review

2.1 Seismic behaviour of historical masonry structures

Buildings are subjected to natural and human hazards. The costs generated by disasters in the last 50 years have grown exponentially, this has repercussions on society, as in cases of major disasters there is a need for large investments which must therefore be obtained through the increase in taxes. The earthquake is not the most expensive disaster, but it is the one that kills the most people in the world, just think that 40% of disaster deaths occur due to earthquakes. It should be emphasized that 60% of these deaths derive from the collapse of unreinforced masonry structures [22]. Looking at our monumental heritage, most of it is in unreinforced masonry, since it is the most common construction typology in the world, but it is also the one that produces the greatest number of deaths during natural disasters. When it talks about buildings of monumental heritage, two aspects must be considered: the importance of these on society and the economy. Heritage structures, in fact, are the identity of a State since they represent its past and if there is no past cannot be a future. While speaking from an economic point of view, it should be noted that many countries of the world base their economy on tourism, just think that 10% of Europe's gross domestic product is based on it, this is evident by the UNESCO World Heritage sites distribution (Figure 2.1). For these reasons, it is very important to identify methodologies to monitor their state of health and new minimally invasive methods to increase their capacity.

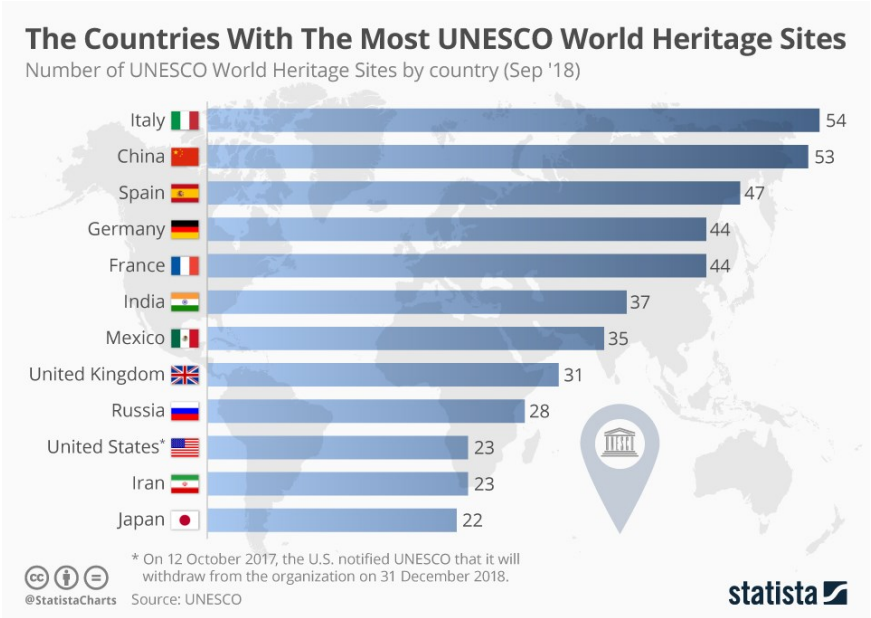

Figure 2.1 Number of UNESCO heritage sites by country

2.1.1 The masonry: mechanical characteristic

The mechanical response of historical masonry structures is a function of its components but also of the arrangements, the type of blocks, the construction techniques, and the state of conservation.

In a masonry wall, two elements are distinguishable: the units and the mortar. The units can be made of stone (granite, travertine, lime, etc), adobe, concrete blocks, or solid clay blocks, whereas the mortar is a mixture of water, sand, binder, and sometimes additives. If tested individually the bricks show a brittle behaviour with high resistance, meanwhile, the mortar has a ductile response but low resistance. The combination of these elements produces walls that are less resistant to bricks but more ductile able to support stress greater than only the mortar. This phenomenon is since the mortar has higher deformability than the blocks. If this were not confined, it would show greater deformations due to its lower elastic modulus and the different Poisson's ratio. However, when it is inside a wall its deformations are prevented by the friction between mortar and blocks that produces tensions on the mortar-block interfaces that restore the congruence of the deformations Figure 2.2.a. These tensions are of horizontal compression on the mortar; therefore, they increase its resistance having a confining function, and of horizontal tensile on the blocks, which decrease its compressive strength Figure 2.2.b. From this, it follows that the tension on the blocks is a function of the ratio of the elastic modulus, the Poisson's ratio, and the ratio between the thickness of the mortar and the thickness of the blocks. In fact, the largest thickness of the mortar translates into higher traction on the blocks. [23]

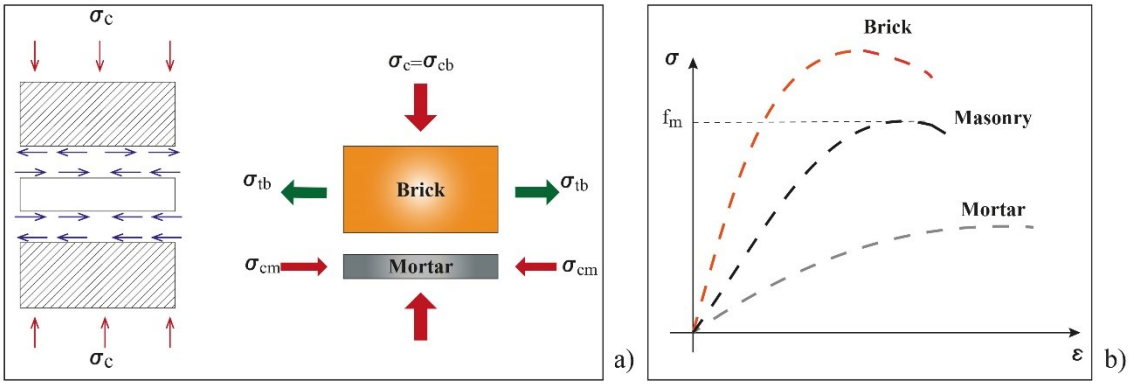

Figure 2.2 a)Inner tensions of the masonry; b) σ-ε diagram for brick, mortar, and masonry

If the state of compression in the masonry does not act in the normal direction to the mortar joints, or if the state of tension is not uniaxial, the texture of the masonry becomes a further element in the evaluation of the compressive strength of the material.

The characterization of a new masonry follows meticulous indications as reported in the Italian Code [24,25] and the Eurocode 6 [26]**.** The compression and the tension stress are normally derived or by tests on masonry panels or the intersection of the singular component's characteristics.

The characterization of historical masonry is harder because, even if it is possible to use in-situ tests, destructive or non-destructive, or extract undisturbed samples, there is no guarantee that they are representative of the entire structure. After all, there can be significant variations in resistance from zone to zone. For this reason, the Italian Code in table C8.5.I suggests values that can be used for this masonry that can be suitably adjusted based on specific characteristics as the thickness of mortar, inner core, etc. using the value in table C8.5.II. Observing the table C8.5.1 (Table 2.1) for each type of masonry two values of its mechanical characteristics are provided; the choice of the value to be used depends on the level of knowledge reached.

Table 2.1 Values suggested in the Italian code for historical masonries

Masonry typology	*fcm* (MPa) *mix* *max*	τ_0 (Mpa) *mix* *max*	f_{vo} (Mpa) *mix* *max*	E (Mpa) *mix* *max*	G (MPa) *mix* *max*	w (kN/m³)
Irregular stone	1.0 2.0	0.018 0.032		590 1050	230 350	19
Uncut stone masonry with facing walls of limited thickness and infill core	2.0	0.035 0.051		1020 1440	340 480	20
Cut stone masonry with good bonding	2.6 3.8	0.056 0.074		1500 1980	500 660	21
Soft stone masonry	1.4 2.2	0.028 0.042		900 1260	300 420	13
Irregular soft stone masonry	2.0 3.2	0.04 0.08	0.10 0.19	1200 1620	400 500	16
Dressed rectangular stone masonry	5.8 8.2	0.09 0.12	0.18 0.28	2400 3300	800 1000	22
Full brick masonry with lime mortar	2.6 4.3	0.05 0.13	0.13 0.27	1200 1800	400 600	18
Hollow brick masonry (percentage of perforation <45%)	5.0 8.0	0.08 0.17	0.2 0.36	3500 5600	875 1400	15

2.1.2 Behaviour under dynamic loads

The seismic behaviour of ancient masonry buildings depends on several factors, namely the properties of the materials, the geometry of the structure, the connections between structural and non-structural elements, the stiffness of the horizontal diaphragms, and building condition. As the quakes showed the historical masonry structures can exhibit three different behaviour under seismic loads:

- Masonry disaggregation, Figure 2.3.a;
- Local mechanisms, Figure 2.3.b;
- Global behaviour, Figure 2.3.c;

Figure 2.3 Different behaviours of historical masonry under seismic loads: a) Masonry disaggregation, b) Local mechanism, c) Global behaviour

The latter is the most desirable but rarely occurs in historical constructions because they often have complex geometries, poor quality materials, and may have undergone many transformation processes over time. The disaggregation is the worst behaviour, it happens when the masonry has not been built according to the state of the art [27]. In the past, there were no written rules that indicate how to build a good construction, but indications deduced by the observation of the behaviour of existing structures were handed down. The main characteristics that masonry must have to be of good quality are:

- The wall must have 2/4 transverse blocks per square meter. In fact, if the longitudinal blocks are used to counteract the seismic action in the plane, the transversal blocks are necessary to counteract the orthogonal actions
- The mortar must enclose each block to have stony compactness
- Each 60/100 cm of wall's hight must realize horizontal surface to have a good stress transmission
- The large blocks must be preferred since in this way fewer sliding planes are created, the greater the size of the blocks and the greater the diffusion of the vertical load, the greater the block and the greater the portion of the masonry that opposes seismic actions
- The empty spaces must be closed with block flakes to increase the contact surface between the blocks and limit the amount of mortar
- The blocks must be stagger so that the loads are distributed over a larger surface and the chain effect is activated

When these characteristics fail, it can not speak of monolithic walls, in these cases, the structure cannot resist the earthquake and before a mechanism is activated it collapses due to the disgregation of the masonry. If the walls-walls and the wall-floors connections exist and are efficient then the structures show a global behavior under the seismic action

"box-like behavior". An important feature for the structure to have a box-like behavior is that the floors, in addition to being well connected, must also be sufficiently rigid to redistribute the forces based on the walls stiffnesses. Figure 2.4.

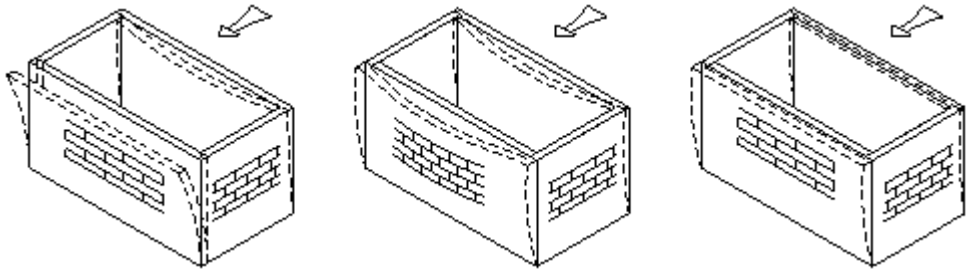

Figure 2.4 Behavior of the wall box: "a" non-clamped walls, "b" clamped walls with deformable floors, "c" clamped walls with rigid floors

This, however, is difficult to see in heritage constructions since the presence of typical and specific vulnerabilities causes that the structure is divided into different macro elements, each of which reacts differently during a seismic event.

The aims of retrofitting and strength intervention are to avoid the macro-elements formation preferring a box behaviour and increase the walls' capacity in their plane.

2.1.3 Local analysis

To study the behavior of macroelements, static, linear, or non-linear analyzes can be used, but the most suitable analyzes in these cases are kinematic ones. The macro-elements can be considered as a labile set of rigid bodies, that form a kinematic chain, that can rotate among themselves due to the low tensile strength of the masonry. The hypotheses underlying this type of analysis are that the masonry:

- Is comparable to assembly of rigid blocks;
- Has zero tensile strength;
- Has infinite compressive strength;
- There is no sliding between the joints.

At each block are assigned the vertical loads acting and the horizontal forces proportional to them through a multiplication factor. The operation consists of finding the multiplicative factor that brings the system to the equilibrium limit. This operation at the seismic level is justified by the fact that it mobilizes the horizontal inertia forces. To determine the multiplicative coefficient, the principle of virtual works is used, placing the work of external forces equal to the work of internal forces, the latter considered in most

cases to be null since the effect of friction and the various internal constraints (Eq. (2.1)). The displacements of the different applied forces are determined based on an initially assigned rotation.

$$\alpha_0\left(\sum_{i=1}^{n} P_i\delta_{x,i} + \sum_{j=n+1}^{n+m} P_j\delta_{x,j}\right) - \sum_{i=1}^{n} P_i\delta_{y,i} - \sum_{h=1}^{o} F_h\delta_h = L_{fi} \qquad \textbf{(2.1)}$$

Once the multiplier has been found, it must be converted into the capacity of the macro element considering the weight forces, the confidence factor, and the mass participating in the mechanism Eq. (2.2).

$$\alpha_0^* = \frac{\alpha \sum_{i=1}^{n+m} Pi}{M^* FC} \qquad \textbf{(2.2)}$$

The capacity must be compared with the seismic demand or the maximum acceleration expected in a given place. This acceleration is a function of the nominal life and class of use of the building, spectrum amplification factor, start the period of the constant speed section of the accelerating spectrum, the subsoil category, and topographic category.

The local mechanisms that most commonly occur are:

- Simple overturning (Figure 2.5.a);
- Compound overturning (Figure 2.5.b);
- Vertical bending (Figure 2.5.c);
- Horizontal bending (Figure 2.5.d);

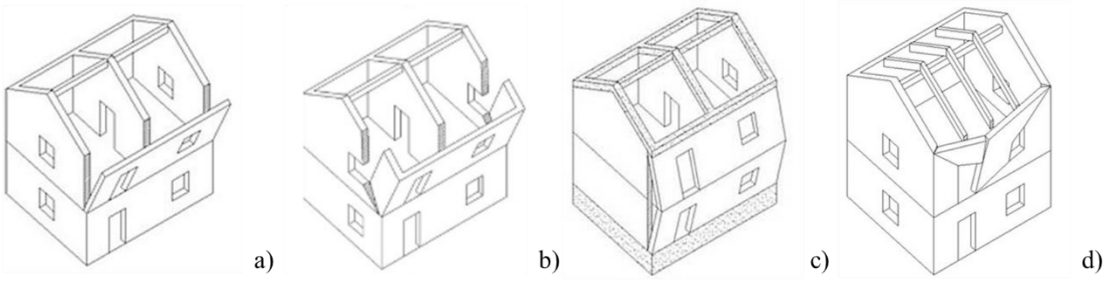

Figure 2.5 Local mechanisms: a) Simple overturning, b) Compound overturning, c) Vertical bending, d) Horizontal bending.

2.1.4 Numerical model

The global analyzes of masonry buildings in the engineering practice are carried out by simplifying the structures with equivalent frames. In the equivalent frame modeling the masonry building is represented by a set of one-dimensional vertical and horizontal elements, connected in the nodes, forming a finite element lattice, in a completely similar way to the schematization of the frames in steel or reinforced concrete. In particular, if the geometry of the wall and openings is sufficiently regular, it is possible to idealize the structure using pier elements (with vertical axis), spandrel elements (with horizontal axis), and rigid nodes elements. This type of analysis can return reliable results as long as the structure is regular, in other cases, it is safer to prefer finite element modeling.

The fundamental concept underlying finite element modeling is the subdivision of the geometry of the structure (domain), characterized by infinite degrees of freedom, into a finite number of elements of elementary geometry Figure 2.6 (subdomain), therefore a finite number of degrees of freedom. These subdomains can be of several types:

• 1D truss and beams;

• 2D shell, plane stress;

• 3D solid;

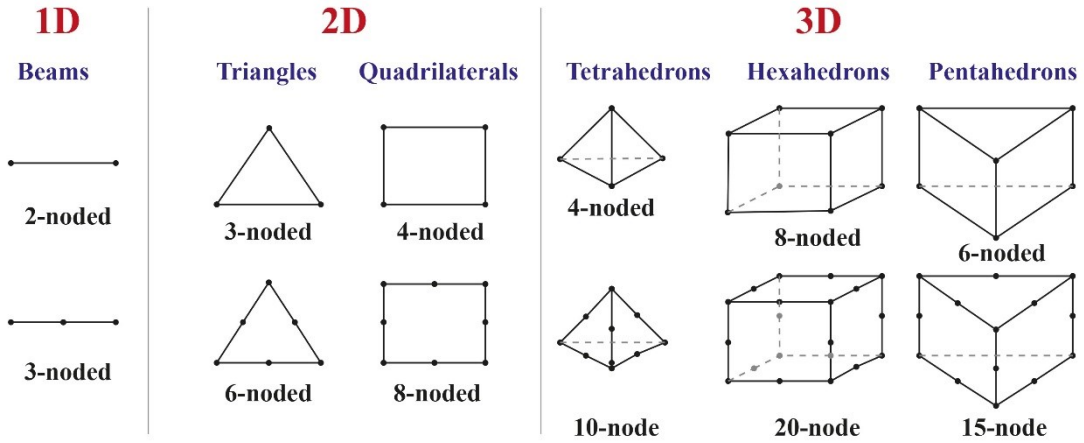

Figure 2.6 Types of meshes available for the Finite Element Modelling

Each of these elements is characterized by a certain number of nodes and a certain number of degrees of freedom, but as much as the discretization is detailed this process allows to reduce reality to a finite number of unknowns. The unknown field is then defined with a series of shape functions within each element.

Three types of modeling can be distinguished [28]:

• detailed discontinuous models: mortar joints and bricks are represented distinctly, and their interaction is considered through an interface Figure 2.7.b;

• simplified discontinuous models: the mortar is not modeled but is incorporated into the block element, the interaction between the blocks is considered with an interface Figure 2.7.c;

• continuous models (or "macro-models"): no distinction is made between bricks and mortar, masonry is considered as a homogeneous, anisotropic, and continuous material Figure 2.7.d.

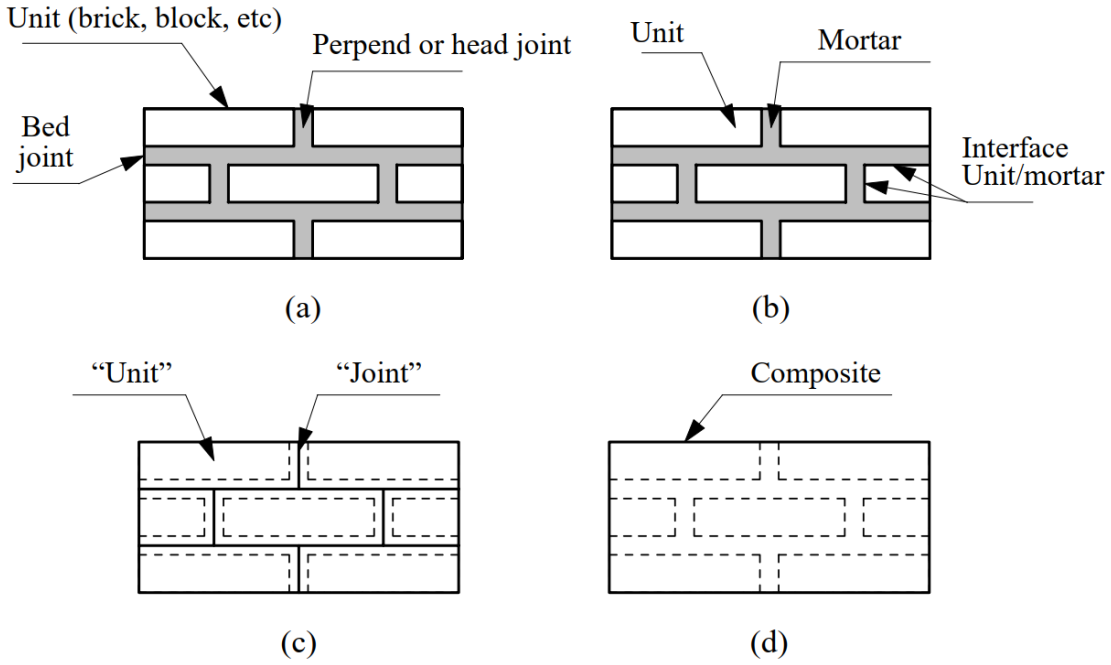

Figure 2.7 Different types of masonry modeling a) real wall; b) detailed discontinuous models; b) simplified discontinuous models; c) continuous models. [28]

The choice of the type of modeling is linked to the type of study to be done. The micro-modeling is suitable when it wants to study a small portion of the structure. On the contrary, macro-modeling is more appropriate when the building is made up of large elements where the transfer of stresses occurs uniformly. In practice, macro-modeling is always chosen, since it requires less modeling and computational time. Micro-modeling, besides the problem of modeling and computational time consiuming, also has the problem of having to define numerous parameters to accurately characterize the

properties of each of its components, which must therefore be derived from experimental tests on them to be appropriate.

In this thesis, it will use macro modeling. In this case, considering the homogeneous material requires the definition of intermediate properties between those of the constituents of the masonry. For the representation of non-linear behavior there are different techniques, one of the most used is the Total Strain Crack Model (TSC). This was introduced to represent the non-linear behavior of concrete, but it has proved suitable to represent also the masonry behavior. The basic concept of the TSC is that stresses are calculated based on the fracture directions and that different modes of crack propagation are foreseen. In the TSC, two types of constitutive reactions can be chosen: the rotating-crack model and the fixed crack model. In the first case, the constitutive reactions are evaluated in the main directions of the stresses while in the second case the constitutive reactions are evaluated in a coordinate system that remains unchanged after having reached the breaking point. When a fracture is created, the tensions progressively reduce as the opening increases, and this behavior is described in the model by a softening curve. This represents the possibility of the material to dissipate a certain amount of energy before reaching the ultimate deformation. The energy required to perform this deformation work is called fracture energy and through its definition, the model can reproduce the non-linear behavior of the material. The possible types of diagrams that describe the compression and tensile behavior are many and can vary according to the modeling needs. [28]

2.2 Retrofitting technique to improve the seismic capacity of masonry structure

During the centuries different techniques were developed to improve the seismic response of historical structures [29]. The intervention can be divided in three main groups:

- **Intervention to increase the monolithic behaviour:**
  - Artificial transversal blocks to connect the curtains of cavity walls;
  - When the poor-quality masonry is in a limited area, local tie-roads can be used
- **Interventions to increase the masonry strength:**
  - Injection of binder mixtures Figure 2.8.a;
  - Re-pointing of the joints [30] Figure 2.8.b;

  - Tie rods opposing to both deforma-tion and disconnection of wall panels [31] Figure 2.8.c;
  - Insertion of stainless steel cords in the mortar joints [32] Figure 2.8.d;
  - Reinforced concrete Figure 2.8.e;
  - Coating with textile or limited in composite elements;
  - Demolition and reconstruction of a portion of the wall "Scuci e cuci" Figure 2.8.f;
  - Steel perforation;
- **Intervention to improve connections;**
  - Metallic chains;
  - Tie-rods;
  - Beams connects to the wall;
  - Top curbs;
  - External wrapping;
- **Intervention to reduce the flexibility of the floor:**
  - The floors have a fundamental role in the box behaviour of masonry structures. Their stiffness must be improved both in the plane that is out of the plane

Most of these interventions can be performed using composite materials such as Fiber Peinfoce Polymer (FRP) or Textile Reinforced Mortar (TRM). For example, the metal chains, used to avoid overturning out of plane and to make the walls collaborate with each other, can be replaced by horizontal bands of these composite materials glued to the walls. Other possible applications are: inserting FRP cables in the mortar joints during repointing, using strips of composite to increase the bending or shear strength of the masonry walls, using strips to increase the capacity of the arches / vaults or improve the stiffness in the plane of the floors. These materials, especially TRM, have recently been introduced in the field of reinforcement, for this reason, many studies are still underway to understand their durability and compatibility with different surfaces. Below is a brief introduction on composites followed by the comparison between FRP and TRM focusing on the latter since, to date, it seems to be the most advanced technology for the reinforcement of masonry structures.

Figure 2.8 Some interventions to increase the masonry strength:a) Injection of binder mixtures; b) Re-pointing of the joints; c) Tie rods opposing to both deforma-tion and disconnection of wall panels ; d) Insertion of stainless steel cords in the mortar joints ; e) Reinforced concrete; f) "cuci-scuci".

2.3 Composite Materials from FRP to TRM

2.3.1 Principal characteristics of composite materials

The need to have materials light, strong and stiff pushed the people to mix different materials to combine their capacity and limit their vulnerability. The difference between the composite materials and the metallic alloys consists that each material in it has a different chemical, fiscal and mechanical properties. The first examples of composites in building engineering were born with the combination of mud and straw fibers to realize the adobe blocks. One of the most famous composites in constructions is the Reinforced Concrete (R.C.) that uses the tensile strength of the steel to improve the concrete capacity.

Nowadays the word composite, in the building field, is referred principal for advance composites. These composites are characterized, normally, by two components: the matrix and the reinforcement. The latter is the stronger and stiffer material, meanwhile,

the matrix is the less strength element that permits to protect and keep in its position the reinforcement and it has the task of transmitting the stresses. The reinforcement is the discontinuous phase of the composite, it can be in the form of particulates, fibers, or strips. The particulate, respect the other types, is less resistant and stiff, and they are normally 40% of the material. The fibers have a length greater than the diameter, they can be continuous (for example unidirectional, woven cloth, and helical wound) or discontinuous (chopped fibers and random mat) Figure 2.9. The continuous fibers are expensive compare to the discontinuous fibers, for this reason, they choose only when are needed high-stress resistance and stiffness, in all other cases, the others are preferred.

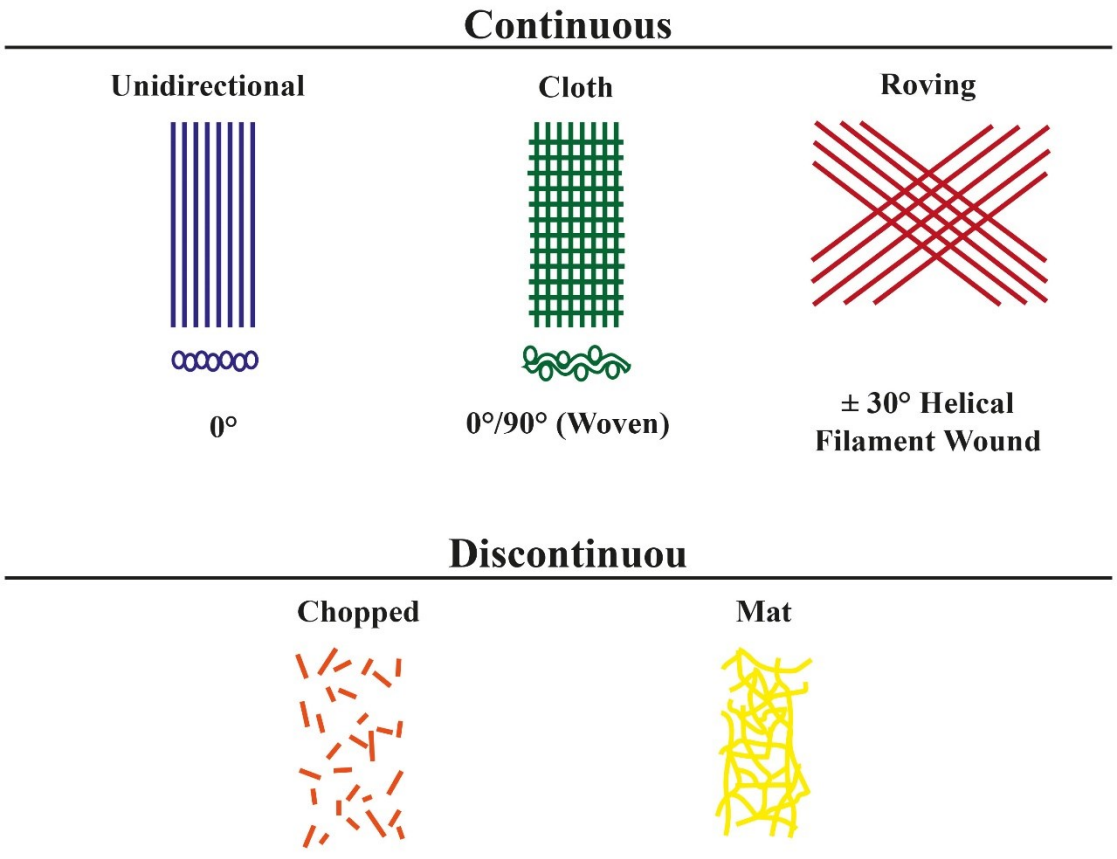

Figure 2.9 Fibers in composite materials

The composites that have fiber as reinforcement have an orthotropic behaviour, in other words, since they have three symmetric planes orthogonal to each other, only the coupling between stretches and their transversal stresses are permitted, as in the isotropic material, ad exception that, the orthotropic materials have different properties in each direction.

This explains as the strength is connected to the fiberers' orientation, indeed, the fibers work when the load is applied along their principal directions. There are different types

of composites: the lamina, where the fibers are only in one direction, and the laminate, where the layers of the fibers have a different degree of orientation. Of this last group the best one is the quasi-isotropic laminate where the fibers are in 0°,45°,-45° and 90°. [33]

The fibers most used to produce composite materials are glass, carbon, and aramidic. (CNR-DT200/2004 2005) However, today a new type of fiber is emerging, PBO (phenylene benzobisoxazole), which has a resistance comparable to that of carbon but is less expensive.

The filiform geometry is very versatile for the realization of composites, gives these materials characteristics of stiffness and resistance much higher than those possessed by the same materials when they used in the three-dimensional configuration: this is due to the lower density of defects that typically belongs to the one-dimensional configuration with respect to the latter. The fibers are made up of very thin continuous filaments and therefore difficult to manipulate individually. For this reason, they are commercially available in many forms Figure 2.10.

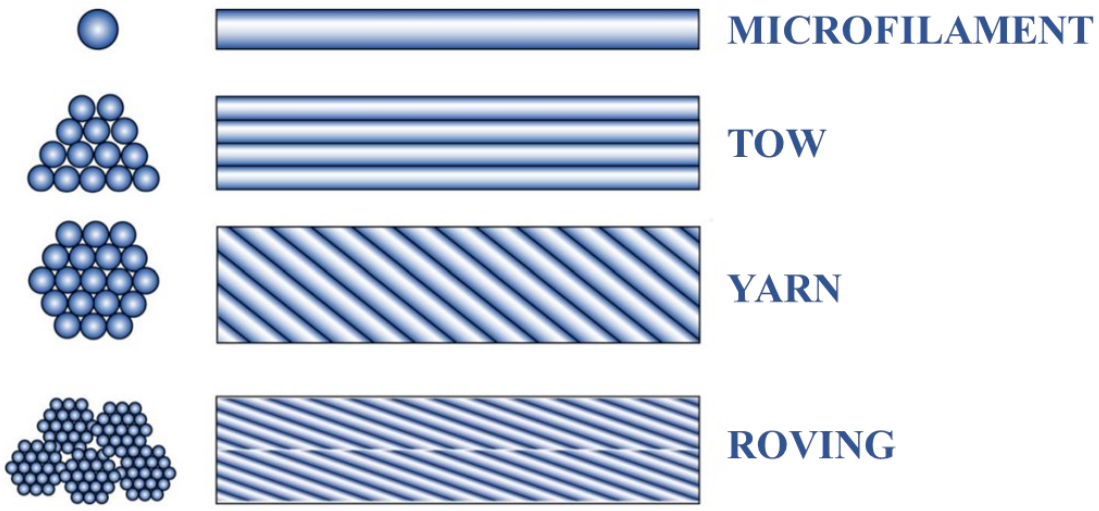

Figure 2.10 Configuration of the fibers in composite materials [34]

Whereas, the most used matrices for the fabrication of fiber-reinforced composites are polymeric ones based on thermosetting resins. These resins are available in a partially polymerized form and are liquid or pasty at room temperature. In recent years, however, interest in inorganic matrices has been growing. These consist of a pozzolanic hydraulic binder and specific additives that favor the development of mechanical and physical characteristics, such as fluidifying, accelerating, aerating, and thixotropic agents.

2.3.2 Fiber Reinforce Polymer (FRP)

The first studies on the composite materials with polymers matrix were done after the II World War to find a new material strong and light to build more efficient airplanes and ships. The first application of FRP was made of glass fibers immerse on the polymeric matrix. After these first applications, it started to be used also in other industrial areas like the automotive. Starting from the 80's they started to be used also in the construction field thanks to the cost reduction and optimization of the production process. The first application in the civil construction was the realization of Radomes during the II Word War since it was looking for a material able to not interfere with the radio waves. The glass fiber reinforces polymer (GFRP) proved to be optimal for this purpose.

In the 1970 architects and civil engineers started to consider this material as a building material and began to project with it. The first application on the civil structures was made using them as the semi-load bearing and infill panels, some examples are the Covet Garden Market in London, Amex House in Brighton, and the Mondial House, London. After these applications, only for architecture needs, in 1980 the engineers started to use it also for structural elements since they were looking for a material able to resists also aggressive and hostile conditions [38]. With the cost reduction and the increase of the need for new technology to repair the existing structures in the 1990s, the FRP started to be used in the strengthening interventions. The first application on RC constructions, for this scope, was the restoration of Ibach bridge Canton of Lucerne in Switzerland [39]. At the start of the 1990s started also the study to understand the applicability of FRP to repair and reinforce masonry buildings. Today it is one of the most used technology to improve the capacities of the historical masonry buildings especially in Italy, Portugal, and Greece. One of the first important examples is the basilica of San Francesco Church in Assisi repaired with aramid and Glass FRPs after the devasting 1997 Earthquake. The quake provoked the collapse of two church's vaults. The collapse of these vaults was provoked by the combination of the fill on the "reni", amassed during the centuries, and the transversal dynamic component of the earthquake, that moving the fill provoked high pressure. The high monumental and historical value of these vaults forbade to re-establish the original curvature and to give them back their bearing capacities because these interventions would have ruined the frescos. The best intervention found to preserve the frescos and guarantee the structure stability was the use of composite materials. The FRP strips were used to realized little thin ribs on the extrados that followed the typical shapes

of the Gothic vaults. The ribs were reinforced using unidirectional aramidic fiber bars in the intrados and glass fiber bars at the extrados since glass is more performance under compression Figure 2.11. [40].

Figure 2.11 Collapse and reinforcement of Gothic vaults of San Francesco Church in Assisi

FRP composites are made up of fibers and polymer resins as their name indicates. The most commonly used fibers are carbon, glass, basalt, and aramid, they can be in the form of foil, pultruded strip, tendons, reinforcing bars, or meshes. On the basis that the fibers are placed in one direction or several directions, the result is an orthotropic or anisotropic material. As explained above, the coupling between fibers and matrix allows obtaining a material with high mechanical capabilities able of improving the response of the support on which it is applied. FRP materials have low thicknesses of about 1 mm. This small and cohesive thickness of epoxy resin, in which the long tensile resistant fibers are immersed, causes the loss of strength of the material to occur due to detachment with support. The constitutive bond is therefore comparable to an almost elastic behavior until it breaks with a crack due to sudden detachment, therefore of a fragile type. FRP has a linear behavior up to failure where the maximum resistance is a value lower than that of the fiber but higher than that of the matrix, while the ultimate deformation at break is equal to that of the matrix Figure 2.12. Exceeded this limit the stresses between fiber and matrix are no longer transmitted.

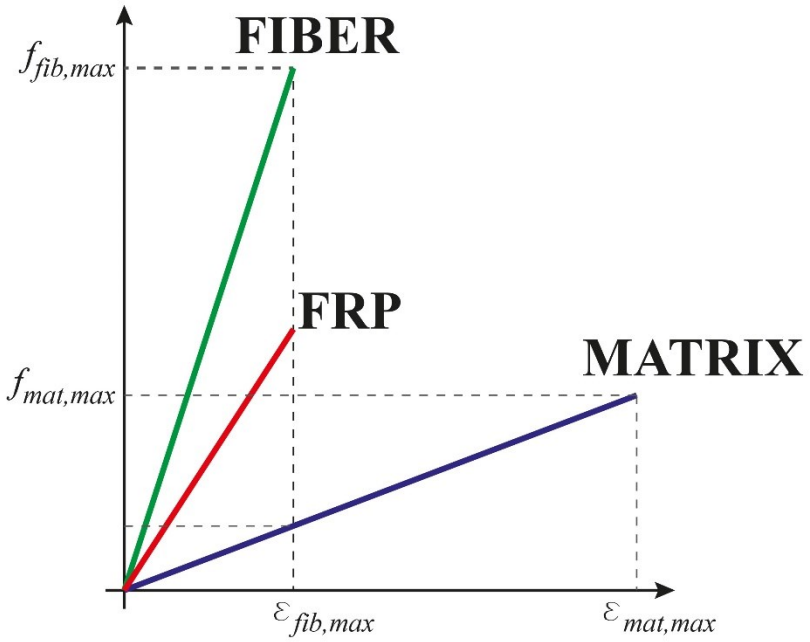

Figure 2.12 Tensile behavior of the FRP

FRP composites are normally used on masonry to:

- increase the resistance of panels, arches or vaults;
- confine the columns to increase their compressive strength and ductility;
- connect the elements that collaborate to resist external action (chains of vaults and walls, connections between orthogonal walls, etc.);
- transform non-structural elements into structural elements, by conferring stiffness and resistance;
- limit the opening of cracks.

Numerous experimental tests have shown that the most common failure mode for FRP is the loss of adhesion between matrix and support. This can happen in two ways or with the detachment of a large thickness of masonry or with the detachment of a thickness equal to the depth of glue penetration. This indicates how the substrate greatly affects, and therefore its quality cannot be neglected when the FRP is designed.

Unfortunately, the use of FRP also has many disadvantages given the use of epoxy resins:

- Working hazard; there is a high potential of harm for workers if the epoxies resins are not worked carefully.
- Damp incompatibility; it is not possible to apply epoxies resins on humid surfaces whereas freeze problems may appear from isolated water.

- Lack of vapor permeability; organic matrices are not permeable, hence frescoes existing at the opposite side of the walls may be damaged.
- Thermal compatibility problems; different thermal coefficients with masonry substrate cause strain incompatibilities; moreover, it is difficult to apply epoxies at low temperatures.
- Lack of fire resistance; polymer composites exposed to fire have no protection.
- Irreversibility; polymeric resins cannot be detached from masonry substrates.
- High cost; the cost of epoxies is relatively high.
- Poor bond to rough masonry surfaces; the substrate roughness and irregularity may cause premature

2.3.3 Fiber Reinforce Cementitious Mortar (FRCM or TRM)

To overcome the limits of the FRP, in recent years the FRCM has been introduced especially for carrying out structural interventions. The substantial difference, which distinguishes it from FRP, is the replacement of the polymer resin with an inorganic matrix, which even if it has less adhesive power and a fragile behavior, allows the vapor permeability and physical/chemical compatibility with masonry substrates and almost total reversibility of the intervention, fundamental characteristics for monumental buildings.

The idea of using resistant elements in a cement matrix dating back to 1840 when Joseph-Louis Lambot, a source of the growing interest in reinforced concrete, proposed to use iron fibers immersed in a cement matrix to reinforce boat hulls, water tanks, etc. Later this idea was taken up by Pierluigi Nervi with the introduction of ferrocement (patent registered in 1943) [41]. The ferrocement consisted of layers of small diameter metal mesh on which a thin layer of cement was applied, the combination of these materials guaranteed ductility and crack resistance. This technology allowed Nervi to cover large spans with thin shell structures. The first major work he created in this material is the barrel vault of the Turin Exhibition Complex (94 m of span) built in 1948 [42].Figure 2.13

Figure 2.13 Ferrocement barrel vault of Turin Exhibition Complex built

In more recent times, always inspired by the same technology, a material called Textile Reinforced Concrete (TRC) was developed, in this material the metallic meshes were replaced with alkaline fibers of glass, carbon, or aramid combined with high-performance fine-grained concrete. This material is now known as FRCM (Fiber Reinforced Cementitious Mortar) or TRM (Textile Reinforced Mortar).

The TRM, contrary to what has been seen for the FRP, generally presents the detachment by unthreading of the fibers within the matrix, thus generating a ductile behavior. Analyzing its tensile behavior, three phases are distinguished, the first where both the matrix and the fiber contribute, in this phase the slope can be considered as that of an equivalent section where the fiber and matrix are perfectly connected. The second phase begins with the formation of the first crack in the matrix and ends when this becomes completely non-reactive, in this phase the fibers begin to flow inside the matrix. This particular phenomenon, which distinguishes TRM from FRP, is generated by the fibers that are grouped in small bundles separated from each other and rationally distributed in the cement matrix layer. This configuration permits to transfer the tensions between the fiber and the matrix along the perimeter of the single bundle as it normally occurs in reinforced concrete between rebar and mortar. At the end of the second section, the matrix is completely cracked and the only reacting part is the fiber, in fact, the post-elastic section has a slope comparable to that of the fiber while the ultimate deformation is a function of the maximum resistance of the fiber and its effective area. Figure 2.14

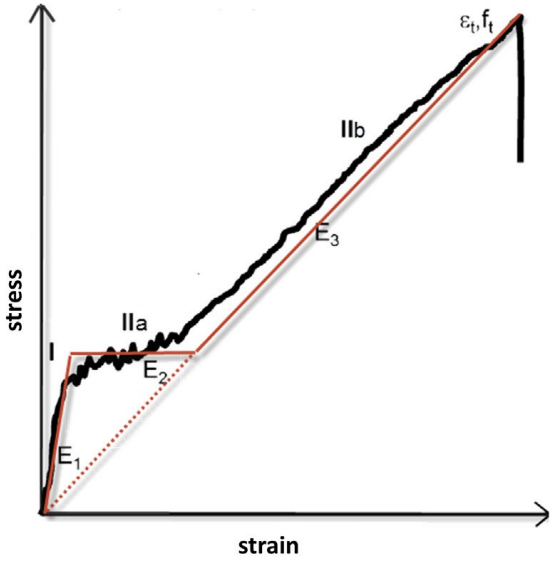

Figure 2.14 Tensile behavior of the TRM

This constitutive law, however, fails to fully represent the behavior of the TRM, which can fail due to the establishment of various collapse mechanisms as shown in Figure 2.15. Failure mode A usually occurs when a strong matrix is bonded to a weak substrate. Failure mode B usually takes place on relatively smooth surfaces and/or may be associated with limited substrate preparation or unfavorable curing conditions. Failure mode C is governed by the amount of the mortar through the voids between fiber bundles or cords and is often exhibited by TRM systems comprising textiles with small grid/cord spacing. Failure mode D usually takes place when dry fiber bundles (not provided with coating or impregnation) or smooth ropes, characterized by a relatively weak bond/interlocking with the matrix, are used. Finally, TRM systems comprising relatively weak textiles with small equivalent thickness may exhibit failure mode E1 (generally when fiber bundles are provided with pre-impregnation or coating) or failure mode E2 (when dry textiles are used). [43]

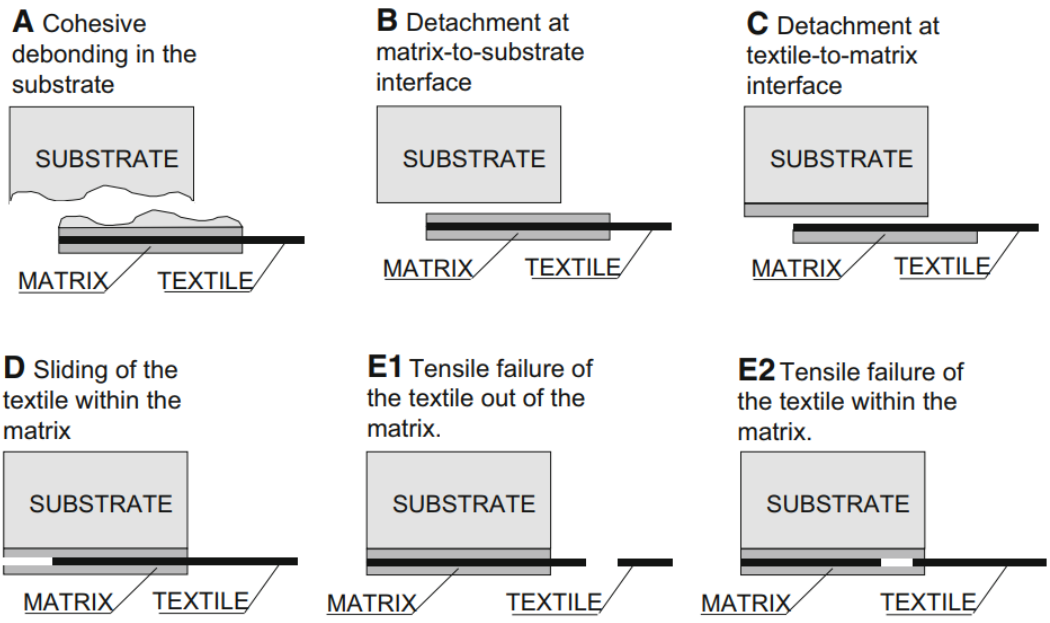

Figure 2.15 Different failure mode of the TRM [43]

Given the several advantages, the TRM in recent years has aroused the interest of many researchers, thus making several reinforcement systems available today. The applications are many, ranging from the reinforcement of bridges to reinforcements of reinforced concrete beams. Even if its use is becoming more and more prevalent, there is still a lot to know both in terms of its mechanical characteristics and its durability over time. [44]

2.3.4 Principal difference between FRP and TRM

Although the functions of the FRP and the TRM are the same, there are significant differences between them. The substantial difference lies in adherence. FRP is composed of a fiber and an epoxy resin, which creates a strong bond with the fiber that prevents it from slipping. Most of the breaking phenomena of the FRP occur at the interface between the resin and the substrate due to the exceeding of the tensile strength of the latter. Instead, in TRM the fiber mesh is immersed in an inorganic matrix that is not able to impregnate the entire yard but only the outermost layer, this means that under excessive stress this bond breaks, and the fabric is subjected to the so said telescopic effect Figure 2.16. The detachment in this material occurs in the fiber-matrix interface, therefore with a mechanism that allows the dissipation of energy. This phenomenon is also closely related to the fiber content because a low content allows greater adhesion, which results in a possible breakage to achieve tensile strength, while for another content this phenomenon is more favored.

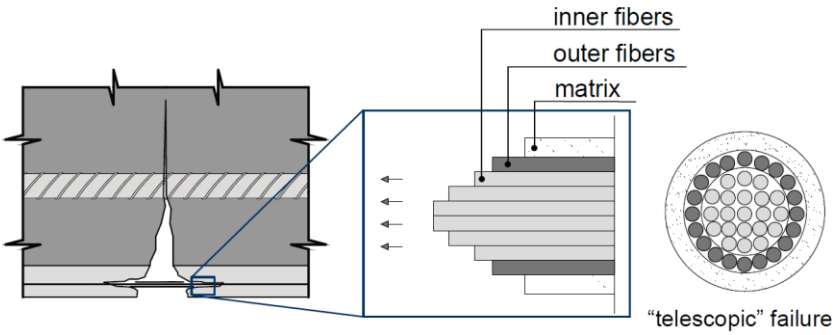

Figure 2.16 Telescopic failure of TRM fibers

The obvious difference between FRP and TRM is that the latter feature open mesh nets in uncommon fabrics. TRM composites bring an important evolution to the technology of reinforcements with composites, as they allow to overcome the problems related to the vulnerability of FRPs to heat thanks to the replacement of the highly flammable polymer matrix with inorganic materials. For TRM materials the matrix is mainly made up of hydraulic mortar, its resistance to environmental attacks is slightly greater than the commonly used mortar since in most cases fine particles are used, so it has a very closed and less attackable structure. On the contrary, given the polymeric nature of the FRP matrix, it is not comparable to any type of material present in construction, for this reason, the standards tend to reduce the initial values of their mechanical strengths more than the TRM. FRPs have been seen over the years to be very vulnerable when placed in humid environments and heat sources. A fundamental aspect when using these materials is to evaluate the compatibility between the materials that come into contact.

Another big difference between TRM and FRP is the installation time. In both cases, there must be a preparation of the support to eliminate the outermost part that has undergone degradation due to environmental effects in order to have a substrate that ensures adhesion. This phase is then followed by the reconstruction of the substrate. If an FRP reinforcement is used, its installation can only take place after the curing phase of the hydraulic mortar has taken place as the epoxy resin cannot be placed on damp surfaces at risk of losing the effectiveness of the adhesion, while the TRM can be applied immediately. Table 2.2

Table 2.2 Comparison between FRP and TRM

Property	FRP	TRM
Deterioration of the matrix	Yes	no
Resistance to heat sources	no	Yes
Flammability	High	Low
Reactions to thermal variations	Not consistent with support	Consistent with support
Regularization of the bonding surface	Yes	no
Workforce requirements	Specialized workers	Qualified workers
Overall times	Awaiting curing of reconstruction mortar	Without waiting for the reconstruction mortar to dry

2.3.5 Experimental Test to study TRM

Given their recent use and the many fibers and matrices that can be used, the research has carried out and is carrying out numerous laboratory tests, on small, medium, and large scale, both to evaluate their mechanical and environmental characteristics.

The codes specify two types of tests to perform for the TRM qualification: mechanical ones and durability ones.

Based on the codes indications, Rilem TC 250-CSM (Composites for the Sustainable Strengthening of Masonry) and Assocompositi (Italian Industry Association for Composite Materials) performed a Round Robin test on TRM samples. This test was involved 19 institutes scattered in 7 countries of the European Union.[45] The tests involved 28 samples made by 11 industry partners. Table 2.3

Table 2.3 Institutions involved in the test and fibers analyzed [45]

Institution		Textile material					
Name	**Country**	**Aramid**	**Basalt**	**Carbon**	**Glass**	**PBO**	**Steel**
University of Aachen	Germany				G5[a]		
CertiMaC	Italy		B1	C5			S4
Cracow University of Technology	Poland		B1, B4[c]	C2*, C6[c]	G8*	P1	S2
Milan University of Technology	Italy			C3	G3*, G5*	P1	
University of Minho	Portugal		B2		G1, G2		S1
University of Bologna	Italy			C2	G1, G8		S1, S2
University of Chieti-Pescara	Italy	A1*, A2*	B2				S3
Uni E-campus	Italy			C3		P1	
University of Firenze	Italy				G1		S2
University of Lyon 1	France		B1*	C6[c]		P1	
University of Naples	Italy		B2*		G2*		S3*
University of Perugia	Italy				G9[d]		
University of Padova	Italy		B3	C7[c]	G1, G4*		S1
Roma Tre University	Italy		B3*	C1, C3*	G1*, G7*	P1*	S1*, S2*, S4*
University of Salento	Italy			C4*	G6*, G9[d]		
University of Sannio	Italy		B2		G2		S3
University of Trieste	Italy				G10[d]		
University of Patras	Greece		B4[c]	C1*, C5*	G7		
University of Ljubljana	Slovenia				G3, G5[b]		
		1 Supplier	3 Suppliers	5 Suppliers	8 Suppliers	1 Supplier	3 Suppliers
		2 Systems	4 Systems	7 Systems	10 Systems	1 Systems	4 Systems
		Test series	11 Test series	13 Test series	22 Test series	5 Test series	13 Test series
SUMMARY		7 Countries, 19 Laboratories, 11 Suppliers					
		6 Textile materials, 28 Systems, 66 Test series					

[a]*Only direct tensile tests.*
[b]*Only shear bond tests. This institution is the only one that used a double-lap setup for shear bond tests.*
[c]*Test results unreliable for this system. Excluded from the statistics in this paper.*
[d]*Composite Reinforced Mortar systems. Excluded from the statistics in this paper.*
Results included in the statistics presented and discussed in this paper.

Tests have shown that TRMs can be classified into three groups based on their strength and stiffness:

1. Low strength (f_{tm} =325–2163 N/mm^2; f_{bm} = 351–1,583 N/mm^2) and low fiber elastic modulus (E_f = 45–137 kN/mm^2): aramid, basalt and glass system;
2. Hight strength (f_{tm} =1,045–3,468N/mm^2; f_{bm} = 939–3,023 N/mm^2) and intermediate elastic modulus (E_f = 129–192 kN/mm^2): PBO and steel system;
3. Hight tensile strength (f_{tm} = 1,043–2,832 N/mm^2) and highest elastic modulus (E_f = 197–240 kN/mm^2): Carbons system.

The choice on which to use must be guided by the type of use to be made. For example, if you intervene on non-reinforced masonry, which has very low tensile strength, there is no need to use high-performance materials, but Low strength is enough. On the contrary, if you must intervene on elements carried in concrete it is better to rely on high stiffness and high strength. The study also identified that a wider spell allows for greater adhesion to the substrate as the mortar surrounds the fiber mesh better.

This experimental campaign highlighted a weakness in the tests, namely, that there was a big difference between the tests of the different laboratories due to many factors: curing conditions, manufacturing conditions, types of grips, misalignment of the fibers concerning the loading direction. From this arises a clear need to develop uniforms rules for performing tests.

Most of the experiments found in the literature mainly concern the fiber and its coupling with the matrix. On the other hand, few studies have focused precisely on the latter. One of these is [46], the authors try to identify the parameters necessary for correct numerical modeling of the matrix. Although for the fiber it is acceptable to consider a brittle-like behavior, given the high strength and stiffness of the material, for the mortar this is not possible and it is necessary to define laws that need more parameters than those declared by the manufacturers. In the article, the authors perform two types of tests: direct shear and three-point bending. Through these tests, they can obtain the tensile strength values and the flexural strength values with the relative bonds. The authors point out how the tensile bond can be used for the calibration of the tensile softening law when modeling finite element reinforcement. Another study, also focusing on the matrix, was conducted by A. Dalalbashi et al. [47], the authors studied the effects of matrix aging on adhesion properties by taking into consideration two lime-based matrices and two types of fibers (bidirectional glass and in unidirectional steel). From the experimental tests, it emerged that the curing time of thirty days, normally used for cementitious mortars, is not suitable for lime-based mortars which require several days to fully exploit their capacity. However, the same study showed that it is not possible to identify a unique period for this type of mortar but rather it is necessary to rely on the results of bending tests.

Researchers are also doing studies on how to increase the bond strength between mortar and matrix being this, as it have seen above, a weakness of TRMs compared to FRPs. A possible solution could be the impregnation of the fabric before being immersed in the matrix. The authors Donnini and Corinaldesi [48] have carried out various tensile shear and pull out tests, on TRM systems differently impregnated and treated with quartz and sand. The tests showed that a greater impregnation with epoxy resins reduces or even removes the telescopic effect that is inserted between the filaments, this allows an increase in the mechanical strength of the composite. A further result was that a medium-high level of impregnation allows increasing the adhesion with the matrix by passing from a sliding collapse mechanism to the fiber breaking mechanism, however in this case the

fibers must be treated with sand so that there is friction between them and the matrix and the ductile mechanism is triggered.

Another question left open looking at the guidelines is the phenomenon of grip on curved surfaces. This phenomenon needs to be carefully studied because very often TRM fibers are used to reinforce circular arches or columns. In the literature, there are, for now, few studies. [49,50]. In these two works, it was found that when the fiber is placed on a convex surface its detachment force increases (Figure 2.17), this is because compressive stresses are triggered which improve the friction between matrix and substrate, this phenomenon is all the more developed the greater is the anchoring length of the fiber [50]. On the contrary, when this is placed on a concave surface as the curvature increases, the force, and the ultimate displacement decrease. This behavior is also due to the establishment of normal tensions which in this case, instead of compressing the material, oppose its adherence. In this experiment the break occurred due to the loss of adhesion between the fiber and the matrix, leaving the innermost layer of mortar attached to the specimens.

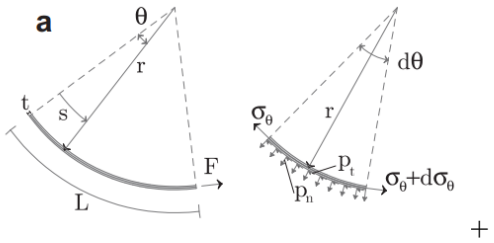

Figure 2.17 Normal-tension of TRM on concave surface[50]

Moving from small to medium scale in literature it finds tests on masonry panels and arches.[21,51–55].

Alecci et al. [51,53] investigated the effectiveness of TRM reinforcements in reinforcing masonry arches. They made masonry arches in the laboratory and reinforced them on the extrados with different fibers, bringing them to break through an incremental vertical load. The comparative reinforcements were PBO-TRM, basalt TRM and FRP, applied to the extrados. From the results, it emerged that both TRM composites allow an increase in strength and ductility compared to the non-reinforced arch, however, when compared to the carbon fiber C-FRP they have a much lower strength. Basalt allows for a breaking load similar to PBO and greater ductility, this difference may be due to different fiber-matrix bonds that are generated. The same authors did other tests by applying this time PBO-TRM, C-TRM and C-FRP to the intrados of the arches [52]. Also in this case it was

found that the TRM can implement the strength and ductility of the arch. PBO fiber compared to carbon fiber and FRP allows for more ductility. Comparing the two articles with each other, it is noted that however, the reinforcement on the intrados is less effective, the PBO reaches a maximum force of 4000 N when applied to the extrados against 1000 N when applied to the intrados due to the phenomenon of normal stresses which they are generated in the arches mentioned above.

Always remaining on the arches topic Berolesi et al. [56] investigated the ability of glass fiber G-TRM to improve the structural response of cross vaults built in the Catalan manner. After having made two vaults in the laboratory these were brought to break causing a collapse of a pier. The vaults were then repaired and reinforced on the extrados with TRM and retested. From the experimental results, it emerged that the TRM can restore the stiffness of damaged vaults, is able to increase the elastic phase and the ultimate displacement, and reduces the damage of the vaults. Another interesting study is the on-site study of arches and vaults carried out by Carozzi et all [54]. One of these vaults was reinforced with glass fibers immersed in an inorganic matrix applied to the intrados.

Other medium-scale tests are those performed on masonry panels. A very recent work, among these, is by L. Garcia-Ramonda [57] where the efficiency of the TRM in improving the strength in the plane and the ductility of the walled panels was investigated varying the distribution of the reinforcement. The walls thus created were tested with diagonal shear tests. The results showed that all these approaches can improve the structural response of the panel without adding an increase in stiffness. Of all the solutions, continuous reinforcement is certainly the fastest while the least invasive is the one that involves the application of the fiber only in the mortar joints.

Tests on large-scaled are instead still very few [21,58,59]. The experiment by de Santis et al. [58] was carried out at the ENEA research center in Rome. The researchers tested the effectiveness of the TRM reinforcement by creating a U-Shape structure in tuff, with a plan size of 3.30 m x 2.3 m and a height of 3.60 m, whose facades featured a window, a door, and a solid wall respectively. The structure was subjected to shaking table tests using a vibrating table with which the earthquakes of the last earthquakes in Italy were applied. After an initial test, the structure was repaired and reinforced, only in the two damaged facades with TRM in fiberglass and hydraulic lime mortar, and retested Figure 2.18. The experiment by Bertolesi et al [21] equally concerned a U-shape structure, but

in solid bricks, with dimensions 3.11 x 4.19 x 2.12 m^3. Also, in this case, the test was first carried out on the unreinforced structure, which, after being repaired and reinforced, positioned the TRM only on the external walls, was tested again. This experiment will be illustrated in detail in Chapter 4:

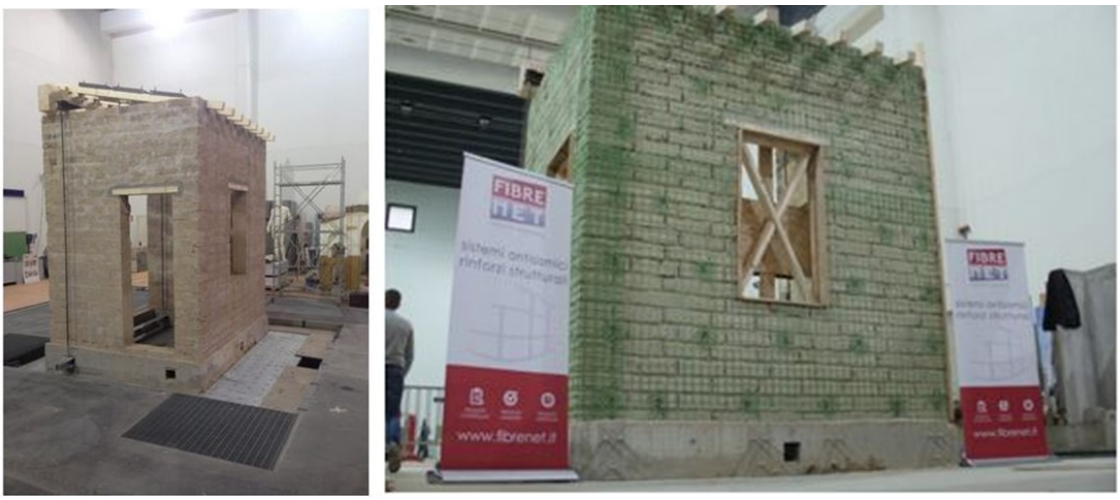

Figure 2.18 Shaking table tests on unreinforced and reinforced U-shape tuff structure [58]

2.3.6 Numerical Models to study TRM

Being a relatively new material, there is still no clear approach as to what the best strategy is to simulate it in a finite element model. In literature, this material is studied with different numerical approaches see Figure 2.19.

Starting from the simplified approaches, there are models where the composite is simplified with 1D schemes composed of non-linear translational springs [60]. Each of these springs represents a component of the composite: matrix, reinforcement, and interface. The stiffness of the matrix and fiber springs are related to their axial deformations, while the interface ones have zero length and are activated by relative displacements between mortar and fiber. Another simplified model consists of the use of 2D elements for the matrix and truss elements for the fiber, the latter with a thickness equal to the sum of the rows in the composite, as in the case of the article by Bertolesi et al [61].

In fact, in this study, this type of modeling is used to analyze the factors that affect the results' dispersion in experimental tests by reproducing different material and geometric imperfections: non-aligned yarns, initial deformations of the specimens, already cracked specimens.

In the literature there are also studies where a macro-modeling of the reinforcement is made, i.e. there is no distinction between mortar and matrix, some examples are [62–64]. The F.S. Murgo and C. Mazzotti study [62] concerns the influence of the confinement of the TRM on a masonry column subject to axial stress. In this case, the model thus made was used to make a comparison with an analytical 1D model. On the contrary, the second [63] examines the modeling of the TRM on a pavilion vault to quantify the effectiveness of this intervention and identify the best location to place the sensors for future continuous monitoring to keep the state of health under control. Another example of macro-modeling is that reported in the works of Oliveira et al. and X. Wang et al.[65,66] in these cases the TRM is modeled with 8-node shell elements inside which there is an equivalent grid that represents the fiber without the possibility of slippage.

Moving on to a greater scale of detail, some authors model TRM using 3D elements for the matrix and 2D elements for the mortar interposed or not by interface elements. An example of this type of modeling is used by A. Monaco et al. [67] to analyze the influence of the interface on the composite response. An extension of this model involves modeling the fiber with Truss elements or fully immersed armature in the matrix or with the bond-slip interface is associated [57,68–70]. In other cases, only the matrix is modeled and the fiber is taken into account only through the use of an interface as in the paper by L. Ricci et al. [71] in which the efficiency of using TRM with PBO mesh is assessed in strengthening masonry arches if applied to the extrados. In this case, the authors employed a 2D micro-modeling where the TRM is represented using 2D plane stress elements for the matrix and an interface, based on the discrete crack model, to consider the presence of the fiber.

In the literature, there are also more detailed models such as those of G. Mazzucco et al. and F. G. Carozzi et al [72,73]. In G. Mazzucco's article, both the matrix and the fiber's mesh are modeled with hexahedral elements, to study the bonding behavior in detail. Whereas F. G. Carozzi uses 3D elements with 8-nodes infinitely rigid interconnected with inelastic interfaces for the substrate and the matrix of the composite and non-linear truss elements for the fiber that interacts with the matrix through an interface. This study aimed to verify if this type of modeling and the 1D modeling were able to retrace the experimental results.

It is evident that even if a micro-modeling might seem more adequate, as it considers not only the properties of every single component but also the possible interface links between them. It is difficult to apply in common practice since it requires, first of all, the knowledge of numerous parameters, often difficult to obtain, and a huge waste of time both in the modeling phase and in the numerical analysis. From the examination of these different numerical models it appeared that in the case of debonding experiments, therefore of traction of the fiber inside the matrix, it is essential to consider the interface, whereas in all other cases this is negligible, as shown also by Larinaga et al [57]. Many models show realistic behavior in considering perfect adhesion when both the mortar and the matrix are subjected to the same stresses. (Figure 2.19) [69,74–76]

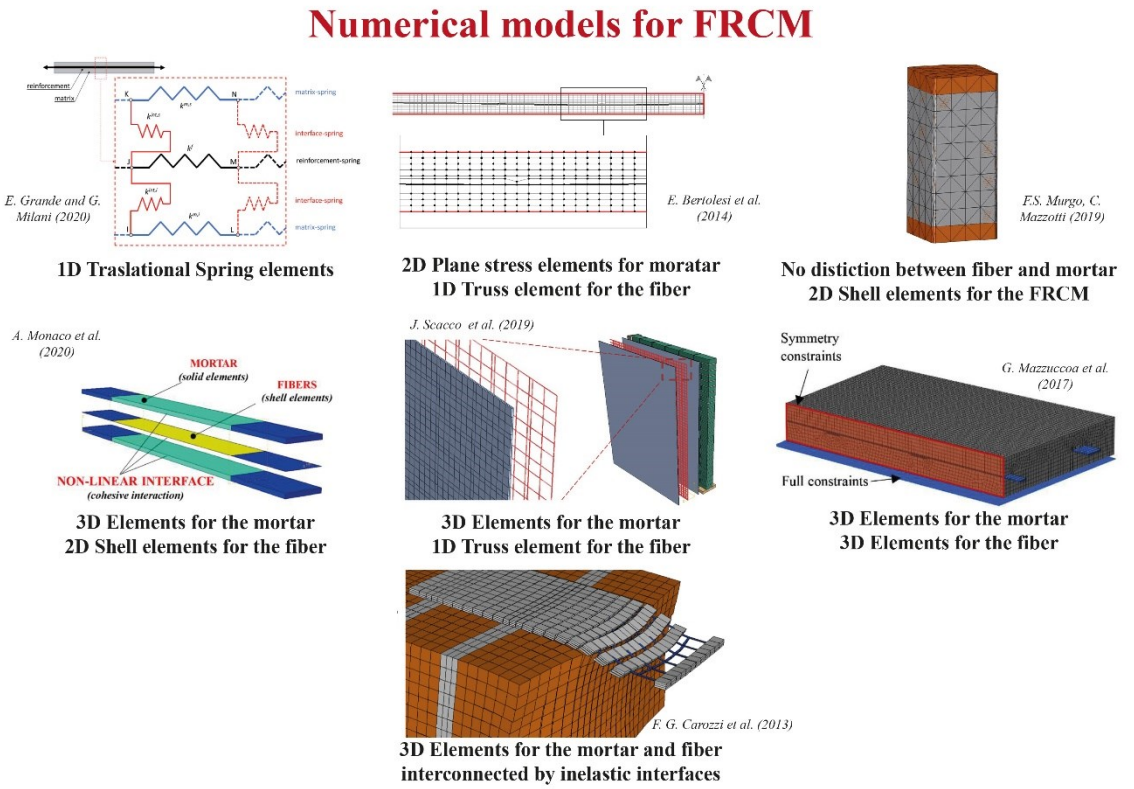

Figure 2.19 Some numerical strategies for TRM in literature

2.4 Vibration-based Damage Identification Methods

As mentioned in the introduction, preserving structures, especially historical ones, must be a primary goal. During their life, all buildings are subjected to various environmental or human hazards that can compromise their structural capacity. For this reason, it is essential to identify methods to monitor their state of health in real-time to intervene promptly before expensive interventions are required or sudden collapses occur. Especially for heritage structures, this must be done by choosing minimally invasive

techniques to follow the principles of conservation. A technique that has recently undergone great development is that of monitoring the dynamic characteristics of structures under only ambient noise (environmental and operational). The wide interest in the use of dynamic properties derives from the fact that they are related only to the intrinsic characteristics of the structures, which do not undergo alteration except for entire changes to the artifact. Knowledge of dynamic behavior can be pursued in two ways with an analytical or experimental approach. The first technique consists of obtaining the mass, stiffness, and damping matrices from the knowledge of the structure and then solving an eigenvalue problem for determining the modal parameters of the structure. On the contrary, the experimental approach calculates the frequency response functions and estimates the other parameters starting from the measurement of the dynamic input. This last procedure is called an inverse problem since the response of the structure and what produces it is known.

2.4.1 Experimental modal Identification

For the dynamic monitoring of structures, three different techniques are identified:

- Input-output test where the reaction of the structure and the cause that produced it are known
- Output only test, where only the reaction of the structure is known
- Test in free vibration, the systems are stressed with an initial deformation and released quickly.

The most used technique for monitoring civil structures is that of output-only, also known as Operation Modal Analysis (OMA), where the response is measured during normal use of the building assuming that the excitations are of random nature in time and physical space of the structure. The fundamental hypothesis is that ambient excitations can be considered as Gaussian white noise. The data thus measured included ambient forces, structural response, and noise from external sources. To separate these components there are several techniques that can be grouped into two groups: techniques in the frequency domain (Peak Picking, Frequency Domain Decomposition. Enhanced Frequency Domain Decomposition, etc.) and techniques in the time domain (Random Decrement, Recursive Techniques, Stochastic Subspace Identification Methods, etc.). The easiest to use are those in the frequency domain, however, they have problems in identifying values of nearby frequencies.

The instrumentation needed to perform the monitoring usually consists of excitation mechanisms (useful only for input-output), response transducers, capable of transforming physical quantities into electrical signals, and a data acquisition system. The transducers normally used in the civil sector are based on the measurement of the acceleration both for their small size and because through simple mathematical processes it is possible to obtain other quantities such as velocities and displacements from them.

2.4.2 Damage detection

The idea of identifying damage from vibration measurements dates to 1800 when railway workers used to evaluate the condition of train wheels by hitting them with a hammer and listening to the resulting sound. This technique was introduced in the civil sector only in 1980 thanks to advances in computing and detection technologies. [3,6]

In the literature, there are different classifications of damage identification methodologies based on vibrations. The most famous is undoubtedly the one proposed by Rytter in 1993[8]. This classification is made up of four hierarchical levels of increasing difficulty:

- Level 1 (Detection) – the method gives qualitative indication about the occurrence of damage in the structure;
- Level 2 (Localization) – the method provides spatial information about the possible damage location;
- Level 3 (Assessment) – the method gives an estimate of the size of the damage; Level 4 (Prediction) – the method offers information about the actual safety of the structure, estimating the remaining service life.

The hierarchy is because to move on to the next level it is necessary to know the previous one. For this reason, in 2004, to simplify the predicting and damage assessment, a further level was introduced, the classification, between localization and assessment.

Another possible classification of the techniques can be made according to the effects that the damage produces on the structure. In other words, if it is assumed that during monitoring the cracks remain open, the structural response is linear, therefore a function of only the mass and stiffness of the system (Linear Methods). Instead, if it is assumed that these cracks close then it means that there may be a recovery of stiffness, in this case, it is talking about non-linear methods. Most of the methods avaliable in the literature are linear ones which are based on the change of the modal parameters (modal-base), but

there are other methods as well non-Modal-Base. The Modal-base methods can be based on recordings only or use numerical models. Figure 2.20.

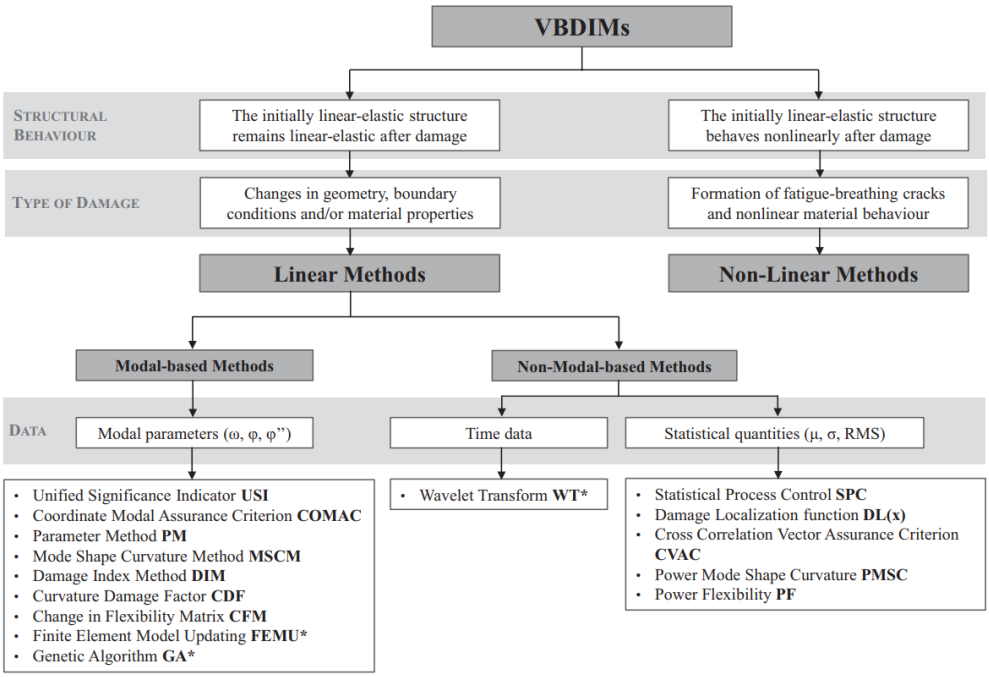

Figure 2.20 Classification of Vibration-based Damage Identification Methods [77]

To date, there is no method that manages to capture all the levels described by Rytter. In the literature, there are many literal reviewers on several methods for identifying damage [3,78,79].

In this thesis, to identify the damage index, it was assumed that the closing effects of the cracks are negligible and that therefore the dynamic identification can be carried out with linear dynamic analyzes in conditions of low levels of environmental excitation. For this reason, only the linear methods present in the modal-based literature will be illustrated below.

Modal-base methods

Modal-based methods use dynamic parameters to identify the presence of damage, these parameters being frequencies, modal shapes, curvatures, and stiffnesses.

The frequencies have the advantage of being immediately available and of not requiring many sensors, however, they are not able to give information on the location of the damage being global parameters. Damages in different positions may produce the same

frequency variation. Another disadvantage of using frequencies is that they are heavily influenced by environmental conditions such as temperature and humidity [80].

On the contrary, the modal shapes are parameters that depend on the coordinates of the system. This feature makes them more sensitive to damage. Another important feature is that they are less affected by environmental effects. However, they have the disadvantage that, to be accurately deduced, it be must use many sensors and that the damage, being a local phenomenon, most of the time affects the high modes which are difficult to identify with accuracy.

To overcome this last problem, another parameter that can be used is the curvature. Unlike the other parameters listed, this is not directly available but must be obtained starting from the modal shapes.

Another parameter used for the damage identification is the flexibility matrix which is estimated from the normalized modal shapes with the corresponding mass and frequencies. Table 2.4 illustrates some of the modal-base indexes avaliable in the literature.

Table 2.4 Some of the modal indexes presented in literature

Authors	Modal parameters	Index	Damage detection level
Cawley &Adams (1979) [81]	Frequencies	$\delta\omega_i/\delta\omega_j$	Detection
Narkis 1994 [82]	Frequencies	$e=\frac{1}{\pi}\,a\cos\left(1-\frac{R_{ij}}{2}\right)$ $R_{ji}=\frac{\frac{\Delta\omega_j}{\omega_j}}{\frac{\Delta\omega_i}{\omega_i}}$	Localization
Silva and Gomes (1994) [83]	Frequencies	$R=\sqrt{\frac{1}{m}\sum_{i=1}^{m}\left[\frac{(Q_i)x-(Q_I)A}{(Q_i)x}\right]}$ $Q_i=\frac{\omega_i^d}{\omega_i^u}$	Localization
Brincker et al. (1995) [12]	Frequencies	$(S_f)i=(\omega_i^u-\omega_i^d)/\sqrt{(\sigma_\omega^u)^2-\left(\sigma_\omega^d\right)^2}$	Detection
Messina et al. (1998) [84]	Frequencies	$\{\delta D\}=\frac{\left\|\{\Delta f\}^T\{\delta f(\{\delta D\})\}\right\|^2}{\left(\{\Delta f\}^T\{\Delta f\}\right)\cdot\left(\{\delta f(\{\delta D\})\}^T\{\delta f(\{\delta D\})\}\right)}$	Localizatopm
Kim and Stubbs (2003) [85]	Frequencies	$SDI_j=\left[\sum_{i=1}^{NM}e_{ij}^2\right]^{-1/2}$	Localization and quantification
	Modal Shape	$MAC_{u,d}=\frac{\left\|\sum_{i=1}^{n}\varphi_i^u\varphi_i^d\right\|^2}{\sum_{i=1}^{n}(\varphi_i^u)^2\sum_{i=1}^{n}(\varphi_i^d)^2}$	Detection
Ewins (1986) [86]	Modal Shape	$COMAC_{i,u,d}=\frac{\left\|\sum_{j=1}^{m}\varphi_{i,j}^u\varphi_{i,j}^d\right\|^2}{\sum_{j=1}^{m}(\varphi_{i,j}^u)^2\sum_{j=1}^{m}(\varphi_{i,j}^d)^2}$	Localization
Dong et al. (1994) [87]	Modal Shape and frequencies	$\Delta\varphi=\sum_{j=1}^{m}\left[\varphi_j^d\left(\frac{\omega_j^u}{\omega_j^d}\right)-\varphi_j^u\right]$	Localization
Pandey et al. (1991) [88]	Curvature	$\Delta\varphi''=\sum_{j=1}^{m}\left\|\varphi_{d,j}''-\varphi_{u,j}''\right\|$	Localization
Stubbs et al. (1992) [89]	Curvature	$\beta_{i,j}=\frac{\left[\int_a^b(\varphi_j^{d''})^2dx+\int_0^L(\varphi_j^{d''})^2dx\right]}{\left[\int_a^b(\varphi_j^{u''})^2dx+\int_0^L(\varphi_j^{u''})^2dx\right]}\cdot\frac{\int_0^L(\varphi_j^{u''})dx}{\int_0^L(\varphi_j^{d''})dx}$ $\beta_i=\sum_{j=1}^{m}\beta_{i,j}$ $\beta_{i,k}=\frac{f_{i,k,j}^d}{f_{i,k,j}^u},$	Localization
Abdel Wahab and De Roeck (1999) [90]	Curvature	$CDF=\frac{1}{N}\sum_{n=1}^{N}\left\|\varphi_{u,i}''-\varphi_{d,i}''\right\|$	Localization and quantification
Pandey and Biswas (1994) [91]	Flexibility Matrix	$\beta=diag\left\{\mathbf{F}^d-\mathbf{F}^u\right\}$	Localization and quantification
Y. Zhang et al. (2012) [92]	Modal Shape	$\Delta_i=\left\|\mathrm{MOSS}_i^u-\alpha\mathrm{MOSS}_i^d\right\|$	Localization
S.H. Sun, et al. (2013) [93]	Mode shapes	$\mathrm{NF}_i(i)=\frac{\overline{\overline{\mathbf{M}}_0(i)}}{\overline{\mathbf{M}_0(i)}}\cdot\frac{\mathbf{M}(i)-\overline{\mathbf{M}_0(i)}}{\sigma(\mathbf{M}_0(i))}=\boldsymbol{\kappa}(i)\cdot\mathrm{Z}_i(i),$	Detection and quantification

Another method that is part of the modal-based group is a numerical model updating. This methodology consists of realizing an accurate numerical model of the case study and calibrating its linear characteristics, such as Young's modulus, Poisson's modulus, and density, to obtain the same frequencies and modal shapes recorded on site. This model, once updated, can be used to make predictions on possible damage or be taken as a reference scenario for possible long-term monitoring. The calibration of the model can be done either manually or with automatic algorithms [7,19,94–98]. On the contrary, non-modal methods use the statistical properties of vibration signals, mean values, variance, mean square deviations, etc.

Chapter 3: Numerical modelling of qualification tests of specimens in TRM

3.1 Introduction

This chapter describes some qualification tests carried out on a TRM with PBO fibers and the respective numerical models. In the first phase, the TRM was modeled by distinguishing fiber and matrix, representing the first with 2D plane stress elements and the latter with 3D solid elements. The reliability of this modeling is proved by the ability of these to reproduce the experimental stress-strain curves. Subsequently, this type of modeling was compared with two other models, in which the geometry was reproduced with different degrees of approximation, to evaluate the differences in terms of global and local response.

3.2 Characteristics of the FRCM system

The TRM analyzed is a structural reinforcement system consisting of a bidirectional PBO fiber mesh and a stabilized inorganic matrix, containing a pozzolanic hydraulic binder compatible with the masonry substrate (PBO-MESH GOLD 22/22 and PBO-MX GOLD MURATURA). The mesh, woven according to a weft and a warp, has sufficiently large meshes to allow immersion in the inorganic matrix. The composite is produced by the company RUREDIL S.p.a. The characteristics shown in the technical data sheet are presented in Table 3.1.

Table 3.1 Values declared by the manufacturer for the PBO-TRM

Fiber properties		**Mesh properties**	
Tensile strength	5.8 GPa	Weight of PBO fibers in the mesh	44 g/m^3
Elastic Modulus	270 GPa	Equivalent thickness a 0° e 90°	0.014 mm
Density	1.56 g/cm^3		
Elongation	2.2-2.8%		
Inorganic matrix			
Compressive strength	>20 MPa		
Flexural strength	>3.5 MPa		
Elastic Modulus	>7.5 GPa		

The characteristics of the matrix have been verified through compression and three-point bending laboratory tests on 40x40x160 mm^3 specimens. Table 3.2 shows the results obtained from the tests after a curing period of 28 days.

Table 3.2 Mechanical characteristics of the matrix obtained from compression and three-point bending tests

	$f_{t,mat}$	$f_{c,mat}$
Average value [MPa]	6.2	35.8
Characteristic value [MPa]	4.3	26.4
Standard deviation	0.98	4.86

3.3 Qualification tests

The qualification tests considered to realize the numerical models are:

- Direct tensile test on PBO fiber;
- Direct tensile test on TRM composite;
- Shear bond test of TRM to clay brick substrate;

3.3.1 Fiber tensile test

Tensile tests on the mesh are used to determine its stiffness and strength. These must be performed on at least nine specimens in an environment with a temperature of 20±5 °C and relative humidity between 40-70%. The length of the specimen must be at least five times the width. The mesh is interposed between two heels which must allow the distribution of efforts.[99].

In the analyzed test ten specimens measuring 100x760 mm^2 were brought to rupture by traction. To carry out the tests and uniformly distribute the stresses at the ends of each sample fiberglass heels of dimensions100x130 mm^2 and 3 mm thick were glued with two-component mortar. These samples were then placed in a test machine which transmitted the tensile stresses at a constant speed of 0.5 mm/sec.

The capacity curves were obtained through a transducer inside the test machine, that measured the displacement, two linear potentiometers arranged on the internal fibers of the specimen at 400 mm (POT1-POT0 Figure 3.1), and two linear potentiometers arranged on the heels (POT2-POT3 Figure 3.1). To simplify the potentiometers placement arranged on the individual yarns and allow the connection with the fibers,

additional PVC heels (dimensions 10x10x2 mm^3) were applied, fixed to the yarns by epoxy resin.

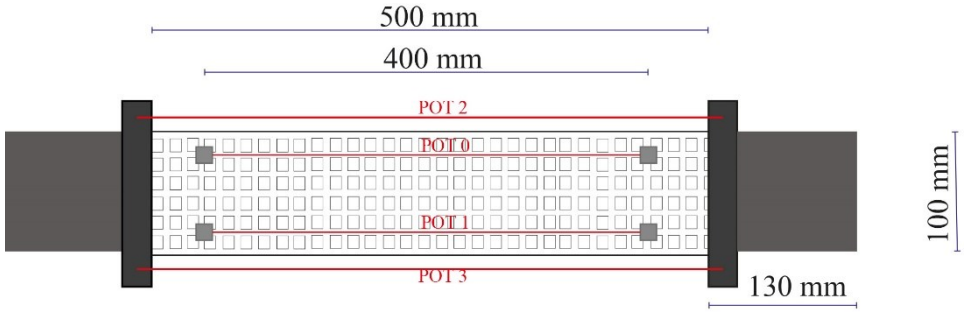

Figure 3.1 Scheme of fiber tensile test

The stress-strain curves (σ-ε) of each test are shown in Figure 3.2, the were strains considering the displacements read on the machine.

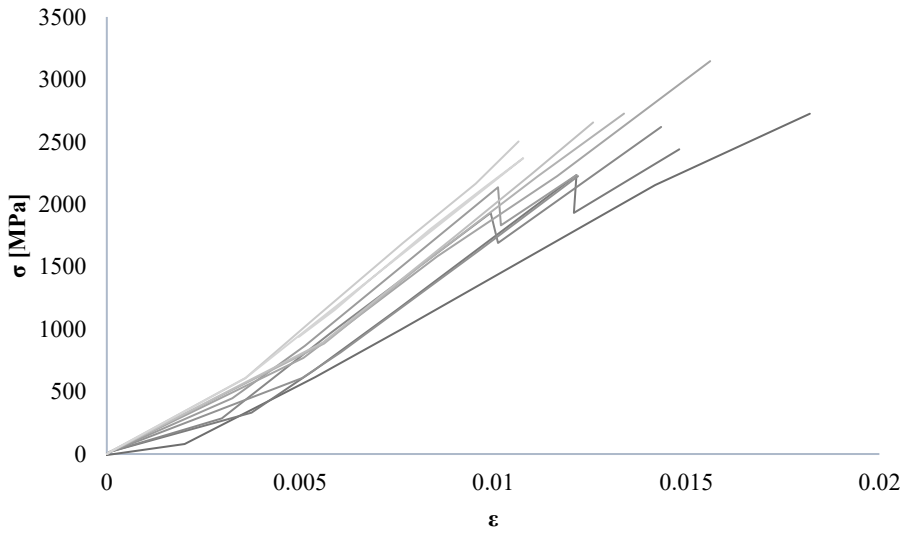

Figure 3.2 Experimental stress-strain curves obtain from the PBO tensile tests

From these results, it was possible to derive the mechanical parameters reported in Table 3.3. The maximum stress (σ_{max}) is given by the ratio between the maximum recorded force and the cross-section of the PBO fiber, while the deformation ε is given by the ratio between the displacement recorded by the machine (d_m) when the maximum force is reached and the length of the sample (L).

Table 3.3 Mechanical characteristics of the PBO fiber

	σ_{max} [MPa]	$\varepsilon(\sigma_{max})$ [%]	E_f [MPa]	E_0 [MPa]
value	3208	1.35%	282047	199963
coefficient of variation	11.83%	17.26%	7.48%	11.88%
formula	F_{max}/A_{res}	$\frac{d_m}{L}$	$\frac{\sigma_{50\%} - \sigma_{10}}{\varepsilon_{50\%} - \varepsilon_{10\%}}$	$\frac{\sigma_{max,n}}{\varepsilon\ (\sigma_{max})}$

3.4 Direct tensile test on TRM composite

The TRM tensile test must be performed on at least 9 specimens which have a maximum length-to-thickness ratio of 5:1. The minimum recommended dimensions are 500 mm long, 60 mm wide and 6 mm thicker. The length where the measurement is made must be 200 mm. The direction of the fibers must be parallel to the longitudinal direction of the sample. The sample must be left to cure for seven days before testing. The sample is blocked by two rigid grips that have neoprene in the middle. The load is transferred by friction to the specimen. The result of this test is a tensile stress-strain curve [100].

The tensile tests of the TRM used in this study involved 14 specimens with dimensions of 560 x 100 mm^2, at the ends of which, as before, are glued fiberglass heels with dimensions of 80 x 100 mm^2 and thickness of 3 mm.

The tensile load was applied in displacement control in the following ways:

- Speed 0.2 mm /min in the first elastic phase until the crack pattern is stabilized.
- Speed 0.5 mm /min from the end of the cracked state until the specimen breaks.

The deformations were recorded with the transducer inside the machine and with two linear potentiometers placed near the heels (POT 0-POT1) Figure 3.3.

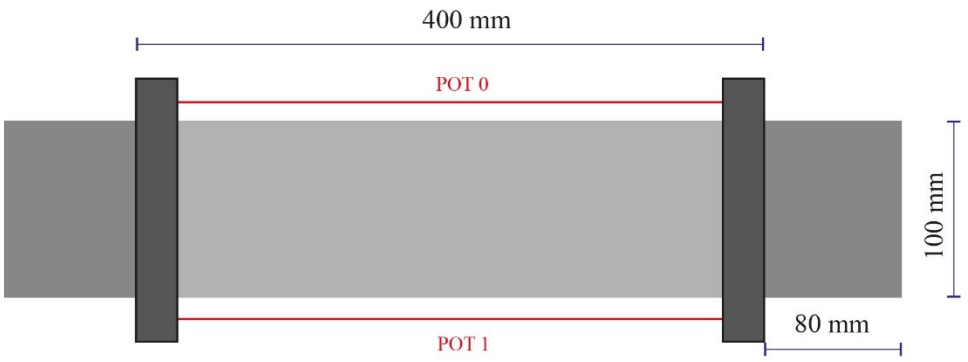

Figure 3.3 Scheme of TRM tensile test

The resulting stress-strain (σ-ε) curves obtain by the displacement recorded by the machine are shown in Figure 3.4.

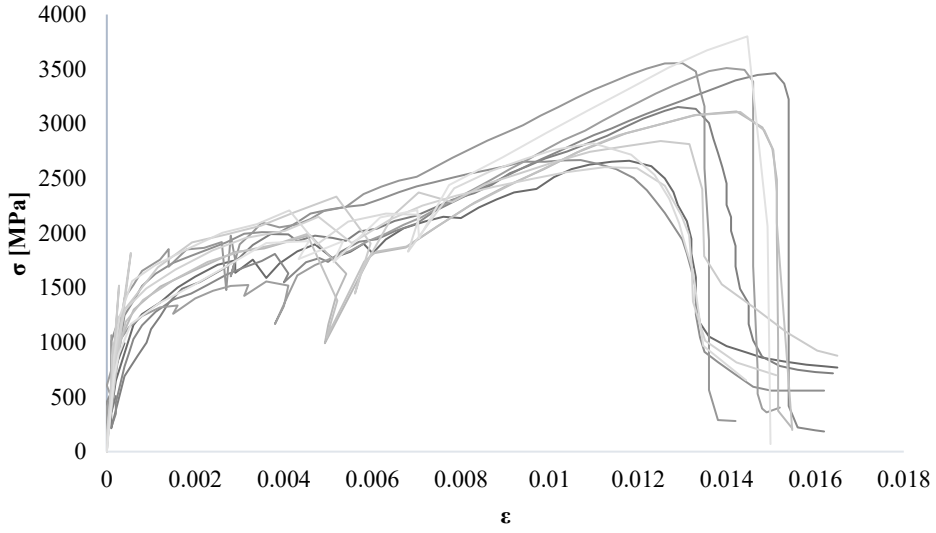

Figure 3.4 Experimental stress-strain curves obtain from the TRM tensile tests

From which the mechanical characteristics shown in Table 3.4 were obtained.

Table 3.4 Mechanical characteristics of the TRM

	σ_{max} [MPa]	$\varepsilon(\sigma_{max})$ [%]
value	3065	1.21
coefficient of variation	12%	14.10%
formula	F_{MAX}/A_{PBO}	$\frac{d_m}{L}$

3.5 Shear bond test to clay brick substrate

The detachment test requires that the TRM system is tested on different types of substrates such as bricks, tuff, concrete, etc. The fiber is placed in the center of the support with a direction of the fibers parallel to the longitudinal axis of the sample. The thickness of the matrix is normally 10 mm unless there are different indications from the manufacturers. The width of the reinforcement must be multiple of the spacing between the fibers and contain at least 3 yarns, normally it is around 40 mm. The length, on the other hand, is normally 300 mm so that the adhesion forces are fully developed. To reduce possible edge noise, the fiber should be at a distance greater than 20 mm from the sides and 30 mm from the top. Finally, it is recommended to leave a free fiber length of at least 400 mm to reduce the normal stresses between the reinforcement and the substrate. After laying, it is advisable to wait 28 days for curing and keep the specimens in suitable

conditions of humidity and temperature. The result obtained from this test is the stress-slip axial relationship. [43]

The shear bond tests examined in this study were carried out on nine clay brick supports made of seven bricks of 250 x 120 x 60mm^3 interposed by six mortar layers of 10 mm. The compressive strength of the bricks is 22.8 N/mm^2, whereas the compressive strength and the tensile strength of the mortar are 5.50 N/mm^2 and 1.74 N/mm^2, respectively. The TRM was applied to the long side of the supports. The bonded length was 300 mm for all tests and started 50 mm apart from the edge of the prism at the loaded end. The bonded width was kept equal to that of the coupons used in direct tensile tests. Fiberglass plates were glue to the end of the bare fiber strip to improve gripping with the testing machine Figure 3.5. The tensile load was applied on the free net under displacement control with a speed of 0.2 mm/min.

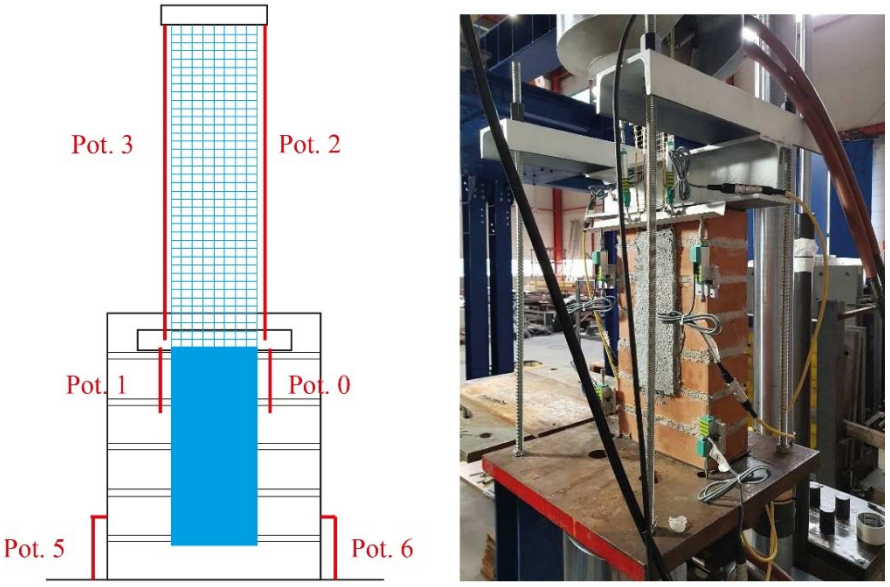

Figure 3.5 Bond test of TRM on clay bricks

The load applied to the sample and the displacement of the crosshead were recorded by the machine. The slip between the fibers and the substrate was measured by displacement transducers fixed to the masonry prism and in contact with a metallic plate (Pot.1-Pot.0 Figure 3.5); this last was fixed to the textile close to the loaded end of the bonded area of the TRM. Furthermore, the possible raising of the samples was measured by two other transducers fixed to support plane and in contact with the base of the samples (Pot.5-Pot.6

Figure 3.5). During the test, 77.8% of the samples showed the tensile failure of the fiber while the remaining 22.2% showed the sliding of the fiber in the mortar bed.

Figure 3.6 shows the force-displacement curves, in which the forces have been recorded by the load cells of the machinery while the displacements have been read using the transducers Pto.1-Pto.0. Observing the experimental curves, anomalous behaviors are highlighted in most of the specimens, these could have been provoked by a non-uniform load on the fiber. In this study, it used only the curves less affected by problems and that corresponded to the braking mechanism of the fiber traction. (The red curves in Figure 3.6)

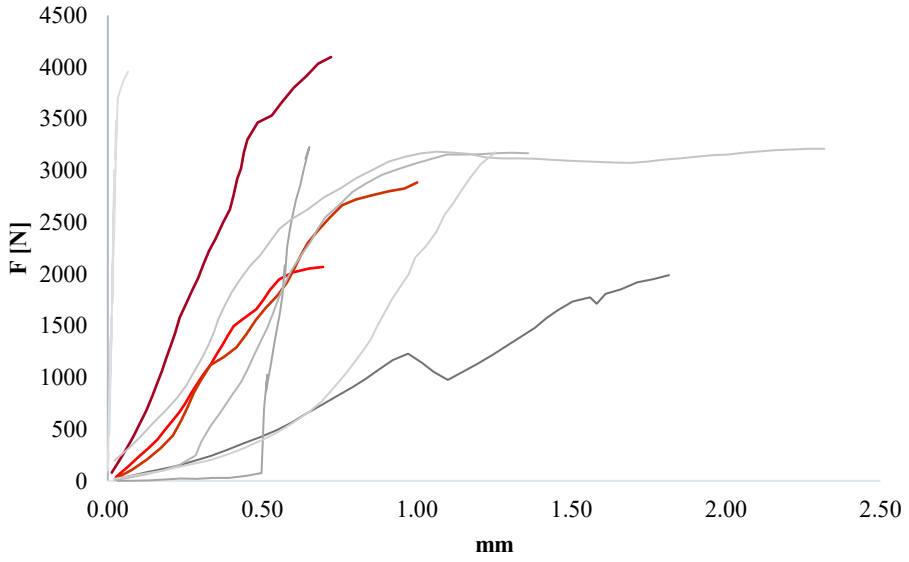

Figure 3.6 Experimental curves of bond test on clay bricks specimens. The results considered for the following analyzes are in red

The mechanical characteristics obtained are shown in Table 3.5.

Table 3.5 Mechanical characteristics of the debonding test on clay bricks support

	σ_{max} [MPa]	$\sigma_{lim.c}$ [MPa]	$\varepsilon(\sigma_{lim,c})$ [%]
value	2322	1662	0.59
coefficient of variation	14.2%		
formula	F_{MAX}/A_{PBO}	$\sigma_{max} - k_n stnd$	$\frac{\sigma_{lim,c}}{E_f}$

3.6 Numerical models

Three different numerical models were therefore created to reproduce the tests showed in the previous chapter (Figure 3.7). The Midas FEA NX © software [101] was used to make them.

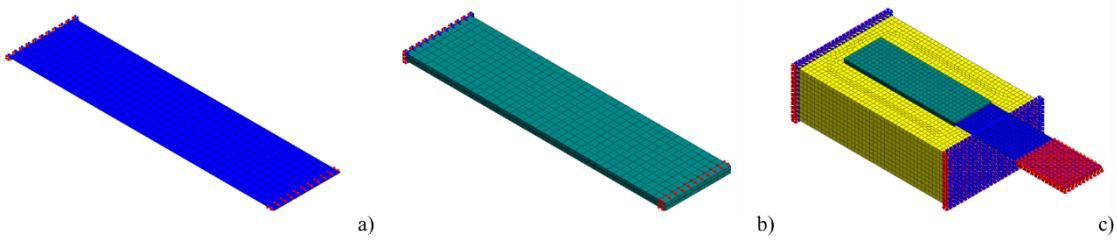

Figure 3.7 Numerical models: a) PBO tensile test, b) TRM tensile test, c) debonding test from clay bricks support

2D elements, plane stress, were used to discretize the fiber and 3D hexahedral elements to represent both the mortar and the support.

The three different models are composed of:

- *Fiber tensile test Model*: 500 elements, 561 nodes and 1683 degrees of freedom (Figure 3.7.a);
- *TRM tensile test Model:* 1200 elements, 1353 nodes and 4059 degrees of freedom (Figure 3.7.b);
- *Debonding Model*: 16565 elements, 13817 nodes and 43464 degrees of freedom (Figure 3.7.c);

The experimental tests were reproduced by applying incremental displacements through nonlinear static analyzes, in displacement control, and using the Newton Rapson as iterative procedure. The non-linearity of the materials was attributed using the Concrete Smeared Crack model implemented on the Midas FEA NX, assigning respectively a

brittle tensile law (Figure 3.8.a) to the fiber, and a parabolic compression law (Figure 3.8.b) and an exponential tensile law (Figure 3.8.c) to the mortar and support.

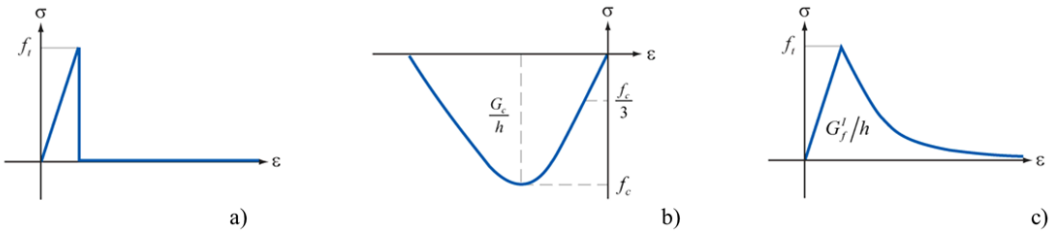

Figure 3.8 Constitutive laws used in modeling: a) brittle tensile law, b) parabolic compression law, c) exponential tensile law

The first analysis concerned the study of the tensile test of the fiber to calibrate its mechanical parameters. The model has been assigned the elastic modulus E_0 and the maximum tensile strength σ_{max} defined experimentally in Table 3.3. Looking at the results, Figure 3.9, notes that the numerical model fully represents the experimental test.

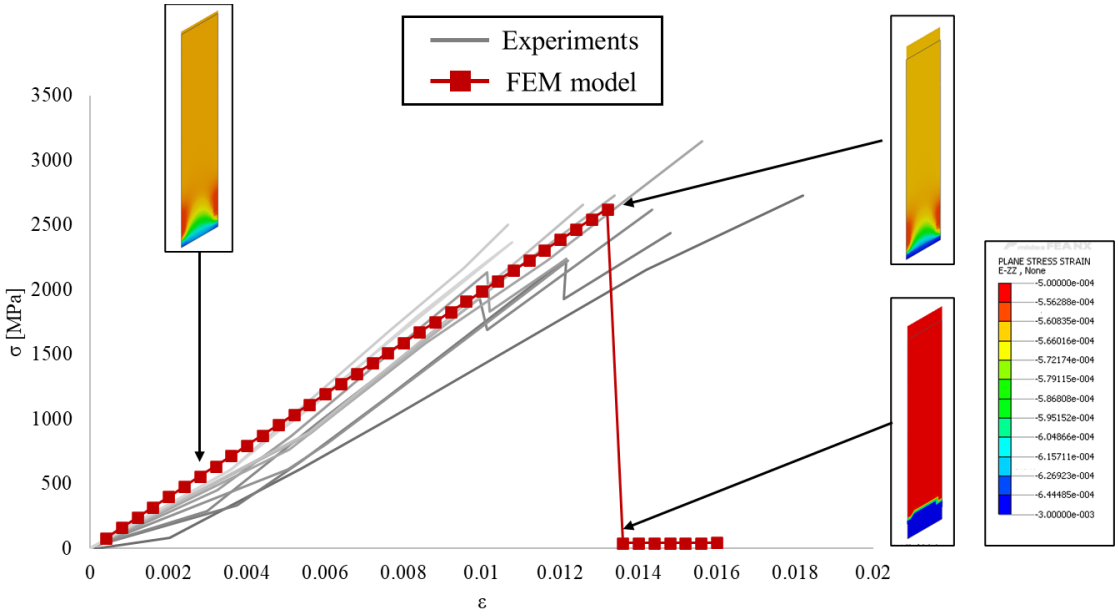

Figure 3.9 Numerical fitting of tensile test on the PBO fiber

Checked that the fiber modeling was adequate, it moved on to the tensile test of the TRM composite. The materials parameters just verified were attributed to the fiber and the values obtained from the experimental tests were assigned to the matrix (Table 3.2). The compressive and tensile fracture energies, G_c and G_f, were estimated using the formulations of Model Code 90 [102] for the concrete.

The results of the model thus made showed excessive resistance in the first branch. (Figure 3.10 blue line). Given that the elastic branch is a function of both the strength of the fiber and that of the matrix, to be able to follow the experiment it was necessary to reduce the tensile strength of the matrix to a value of 2.2 MPa (Figure 3.10 orange line).

Probably the specimens examined here were not kept in constant humidity conditions, which considerably reduced the tensile strength of the matrix.

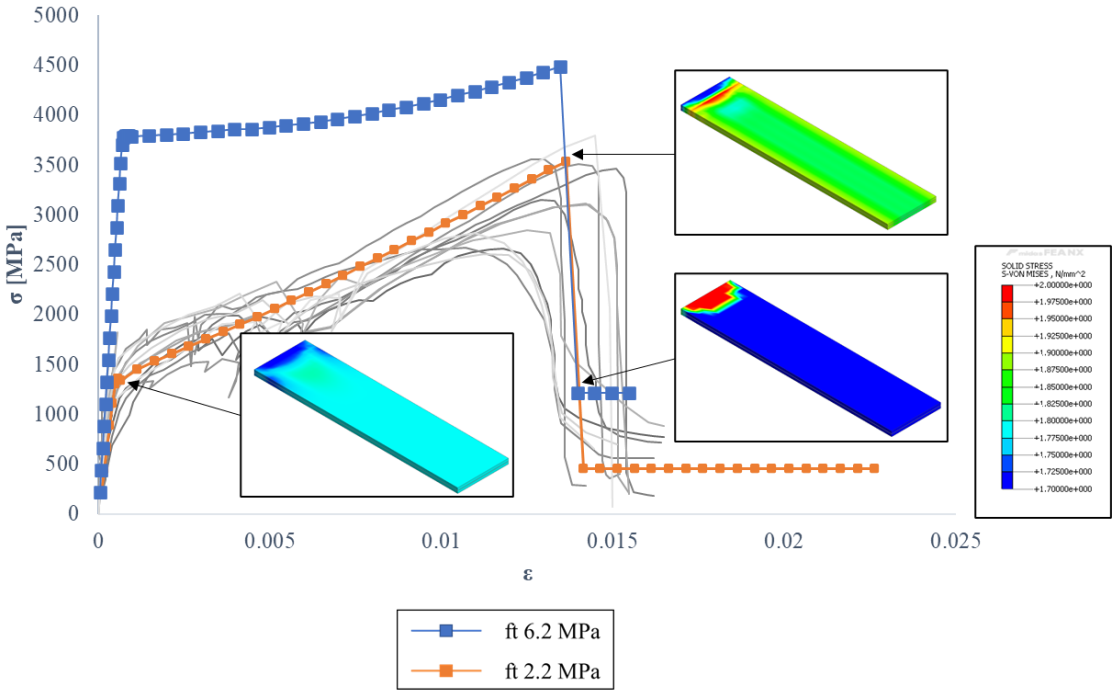

Figure 3.10 Numerical fitting of tensile test on the TRM composite

As a final analysis, the debonding test on clay brick support was reproduced. The model consists of a homogeneous block that represents the masonry on which the reinforcement is glued. The nodes at the base and the top of the specimen were fixed, while an incremental displacement was applied to the free end of the fiber.

To compare the numerical results with the curves of Figure 3.6, the forces were read in the nodes of displacement application, while the displacements were taken in the first node available on the free fiber after the end of the matrix.

The results obtained from this modeling are not as satisfactory as the previous ones there is an excessive stiffness of the response compared to the real behavior Figure 3.11 (blue line).

Similar tests available in the literature are evidence that the debonding failure occurs at the matrix-fiber interface, for the majority of the TRM systems, and is characterized by large fibers-to-matrix slippage. The study of the debonding process is, generally, performed by fracture mechanics Mode-II condition that presupposes the detachment of the composite at the interface given the shear stresses associated with slip between the faces of the interfacial crack. The relationship between the interfacial shear stress, τ, and the relative slip, s, is represented by cohesive material law.

Therefore, to reproduce the experiment, it was introduced an interface of zero thickness between the matrix and the fiber, which as mentioned above is the weak point of this material. To assign the interface it was necessary to modify the previous numerical model, modeling the fiber with 3D elements instead of with 2D elements. The new model consisted of 1200 elements, 4059 degrees of freedom, and 1353 nodes.

In the literature, different types of interfaces have been studied, the most used are the discrete crack model and the bond-slip model. In this work, it was decided to test the latter that is based on the theory of total deformation, in which the tension is expressed as a function of the total relative displacement. In FEA NX for the bond-slip model, the relation between the normal traction and the normal relative displacement is assumed to be linear elastic, whereas the relation between the shear traction and the slip is assumed as a nonlinear function. (Eq. (3.1))

$$t_n = k_n \Delta u_n \qquad t_t = f_t(dt) \tag{3.1}$$

The normal and tangent stiffnesses to define the interface (k_n and k_f) were chosen to provide reasonable stiffness, but small enough to avoid numerical errors. not having enough experimental data, the τ-slip curve was identified through a calibration process. The values of the interface and the τ-δ curve used to fit the experimental data are shown in Table 3.6.

Table 3.6 Bond slip interface parameters

k_n [N/mm³]	k_t [N/mm³]	τ-slip curve
10000	3000	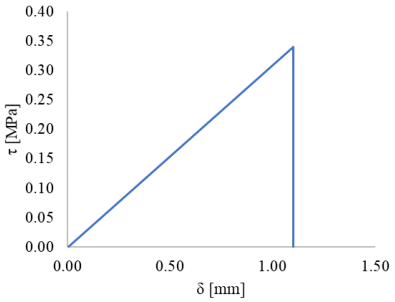

The load-slip curve from the numerical model falls within the envelope of the test data of the experiments and show a good agreement with the experimental results not only in terms of the peak load but also the stiffness and type of failure of the samples, the red line in Figure 3.11. The results imply that the proposed constitutive law with the corresponding parameters can capture the global response behavior of the TRM strengthened masonry elements in the pull-out test.

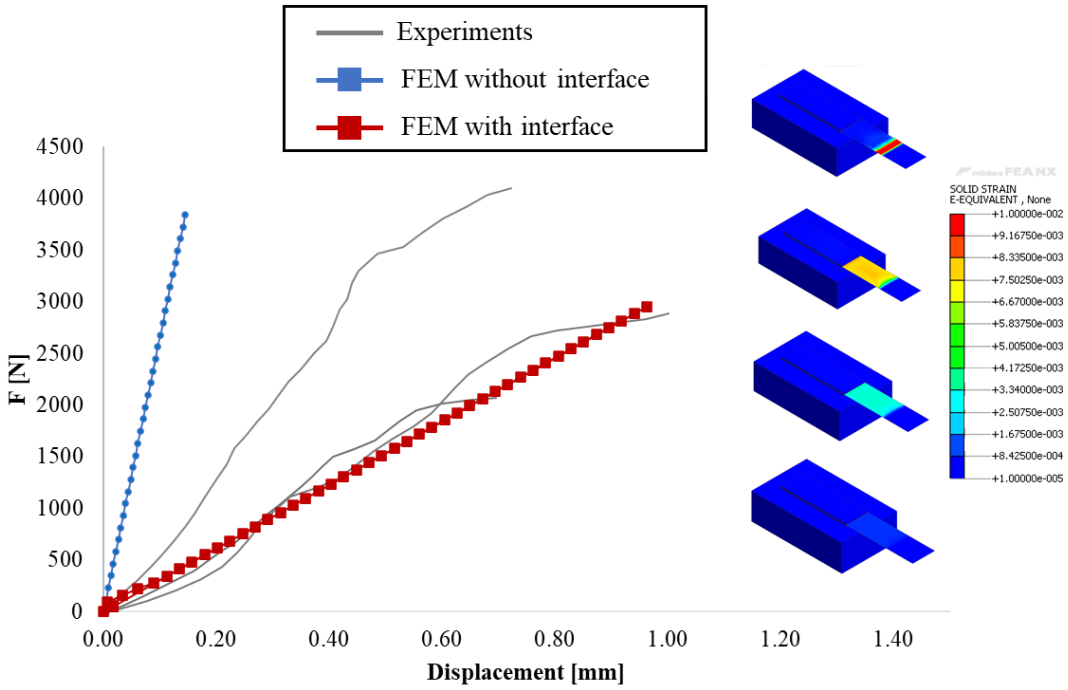

Figure 3.11 Numerical fitting of debonding test

3.6.1 Sensitivity analysis on fiber modeling

Finally, sensitivity analyzes were carried out in order to assess whether the discretization of the fiber with 2D elements was the most appropriate.

The test considered to carry out this analysis is the tensile test of the TRM. The test was therefore represented with two other numerical models. Figure 3.12

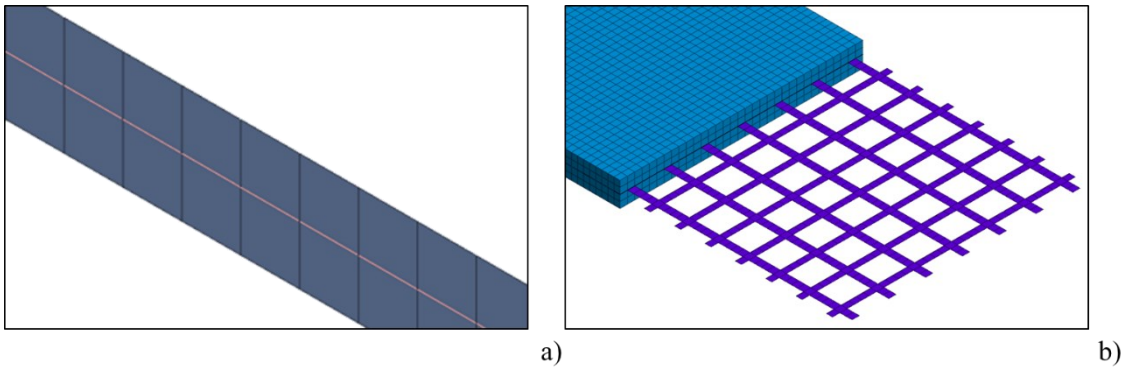

Figure 3.12 Numerical models of tensile test on TRM, a) using 2D elements for the mortar and truss element for the fiber, b) using 3D elements for matrix and fiber

In one of these models, the matrix was represented with 2D elements, with a uniform thickness of 100 mm, while the fiber was reproduced with an embedded truss element with a rectangular section 100 x 0.014 mm^2 Figure 3.12.a. The model is therefore composed of 240 elements, 243 nodes, and 729 degrees of freedom. As previously, the matrix has been attributed a non-linear behavior with the Concrete Smeared Crack model, while the non-linearity of the fiber has been assigned with the Von Mises plasticity model by defining a stress-strain curve.

The other model instead provides accurate modeling of the fiber geometry Figure 3.12.b. To create it, 3D elements were used for both the fiber and the matrix for a total of 26400 elements, 32844 nodes, and 98532 degrees of freedom. The non-linearity of both the fiber and the matrix was defined using the concrete smeared crack model, assigning, as previous, at the fiber a brittle tensile law and at the mortar an exponential and a parabolic law in compression and tension, respectively.

As for the previous model of the TRM tensile test, also these were brought to collapse by applying an incremental displacement to one end of the composite. The results of all three models are represented in Figure 3.13

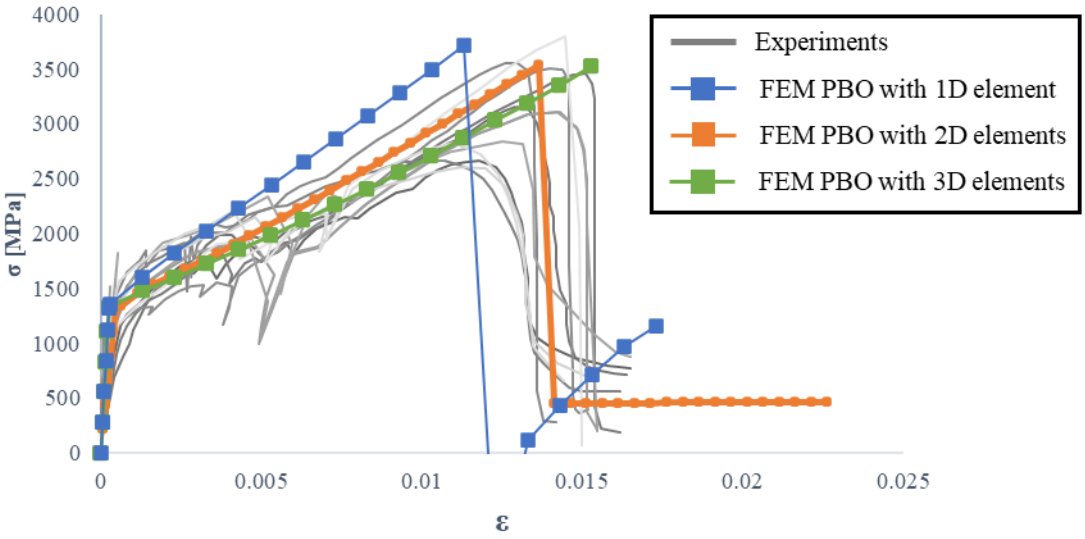

Figure 3.13 Comparison between different types of modeling;

The comparison showed that the elastic stretch and the maximum branch are perfectly reproduced by all three models. On the contrary, small differences were identified in terms of ductility the model with the geometry of the fiber reproduced accurately (blue line in Figure 3.13) underestimates it by 27%, while that with the fiber modeled as the truss element (green line in Figure 3.13) overestimate it by 12%. The graph shows that the model with the truss element is the only one that fails to reproduce the decay of force.

Making a comparison between the Equivalent Strains it is evident that a distribution of the tensions more conforming to reality is obtained only with the accurate modeling of the fiber, see Figure 3.14 Equivalent strains of the three models.

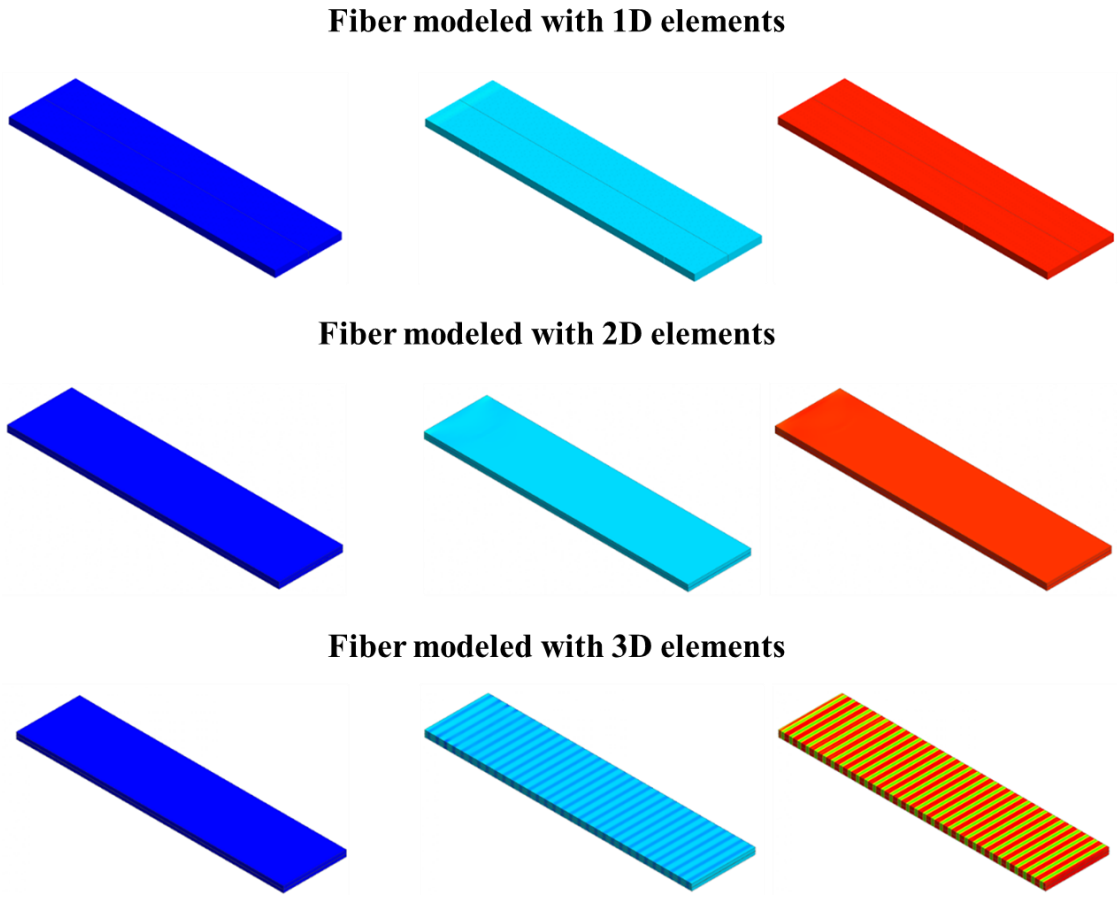

Figure 3.14 Equivalent strains of the three models

3.7 Conclusions

In this case, the modeling of the TRM reinforcement was examined in depth starting from the qualification tests carried out in the laboratory. The tests examined involved a tensile test of a PBO fiber, a tensile test of a composite of TRM with PBO fiber, and a shear bond test on clay brick supports.

Modeling of the fiber with plane elements and of the matrix with 3D elements without interface was found to be adequate for the first two tests, on the contrary, it was not suitable for the modeling of bond tests because in these cases, a slipping phenomenon occurs between fiber and matrix. The only solution that made it possible to reproduce this type of test involved the introduction of interface elements between fiber and matrix, to take this phenomenon into account

Finally, for the tensile test of the fiber, different models were compared which allowed establishing that the model that discretizes the fiber with plane elements can sufficiently reproduce the response of the composite in terms of stress-strain without an excessive

expenditure of time both modeling and calculation phase. However, the best results, if it wants to investigate the stress state of the composite, are obtained only with detailed modeling of the fiber.

Therefore, starting from these observations in the following chapter, the reinforcement applied on a masonry structure will be modeled using plane stress elements for the fiber and 3D elements for the matrix, without introducing any interface since all the reinforcement will be subject to uniform stresses in each its part.

Chapter 4: Experimental tests and numerical models of a U-Shape masonry structure unreinforced and reinforced with TRM

4.1 Introduction

This chapter presents the experimental tests and the FEM models of a 2/3 in-scale structure built in one of the ICITECH' laboratories located at the Universitat Politècnica de València (Spain). The structure has a U-Shape with the bearing structure realized with clay bricks. The tests were performed to evaluate the efficiency of TRM to improve the capacity of unreinforced masonry buildings. With this aim, the structure was first tested without the reinforcement and subsequently, after being repaired, re-tested. The tests consisted of pseudo-dynamic cycles of increasing displacements and frequencies applying on the top with a hydraulic jack [21]. Before and after the tests, environmental vibration tests were carried out to understand how the damage and the TRM influenced the dynamic behavior.

This experiment was studied in order to analyze the ability of the TRM to improve the seismic behavior of masonry structures and to evaluate the possibility of developeing a damage index. As will be read in the following paragraphs, this latter was not possible due to a large number of variables and insufficient dynamic data.

"The experimental work described in this chapter was funded by the Spanish Ministry of Economy, Industry and Competitiveness, Project BIA 2014-59036-R."

4.2 Construction of the U-Shape structure

The structure was of solid two-headed brick English bond masonry. The 0.11 x 0.05 x 0.23 m^3 bricks were interspaced with approximately 10 mm thick layers of lime mortar. The structure was designed with a U configuration with global dimensions of 3.11 x 4.19 m^2 and a height of 2.12 m, with a continuous façade, while the transverse walls had a window and a door, respectively (see Figure 4.1.a). Wooden lintels were placed over the openings, while the slab was prefabricated and simply supported by reinforced concrete beams and hollow concrete blocks. The structure rested on steel plates attached to the laboratory floor. These plates had brackets at the corners of the building to prevent sliding (Figure 4.1.b).

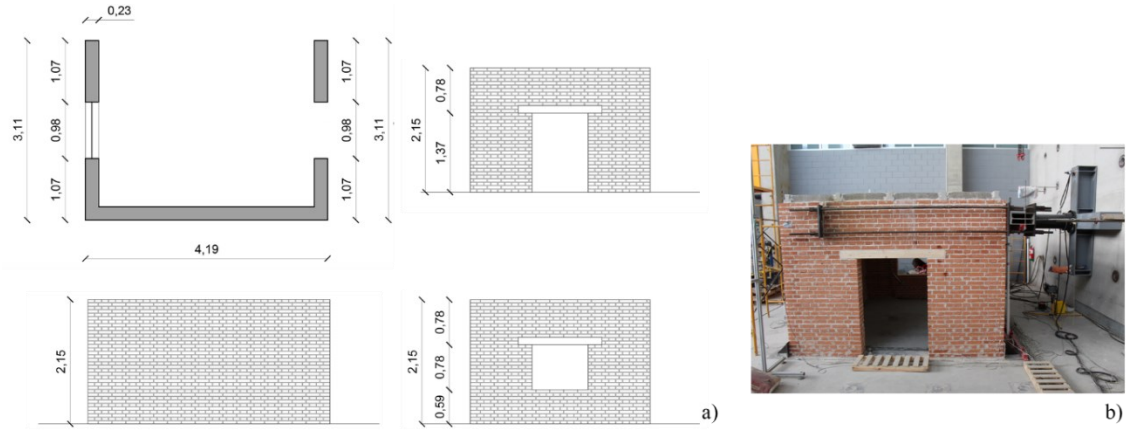

Figure 4.1 a)U-shape geometry (the dimensions are in meters) ; b) Final building and thrust system.

4.3 TRM application

After the firsts test on the unreinforced structure, the cracks were repaired to restore the load-bearing capacity. The cracks were closed following these steps: (i) masonry drilling with 20-40 mm wide holes for a thickness equal to approximately 2/3 of the wall thickness, (ii) positioning of the plastic injectors (iii) filling of the external cracks to avoid the leak of the slurry (iv) injection with a super-fluid injection slurry and finally (v) removal of the plastic injectors. After this operation the TRM was applied only on the external walls face following these phases: : (i) cleaning of the masonry support with water to remove the dust and avoid weak adhesion, (ii) application of 5 mm thick layer of cementitious mortar to ensure the adhesion of the textile to the masonry support, (iii) positioning of the glass textile and finally (iv) application of the last 5 mm thick cementitious mortar layer. (Figure 4.2)

Figure 4.2 Construction phases of TRM application. a) Cleaning of the masonry support; b) Application of the first layer of mortar; c) Positioning of the glass textile and finally; d) Application of the second layer of mortar.

4.4 Material characterization of the components

The constituent materials involved in the construction and repairing of the masonry prototype were tested. In particular, the constituent materials composing the masonry support (lime mortar and solid bricks) as well as the cementitious mortar of the TRM strengthening have been analysed using a series of three points bending and compressive tests.

4.4.1 Masonry substrates

Clay Bricks

Four bricks randomly selected into the ones adopted for the construction of the masonry building have been used to perform a series of tests. The laboratory investigation has been developed on full bricks in order to characterize the flexural strength (three-point bending tests) of the clay brick material. Figure 4.3 depicts the experimental set-up adopted to perform the three-point bending test and the compressive one. From the halves obtained at the end of the three-point bending test, four specimens have been obtained to be tested in a direct compression test. In addition, Figure 4.3 shows the force-displacement curves obtained at the end of the laboratory campaign. The prismatic specimens obtained at the

end of the three-point bending tests have been also used for the identification of the elastic modulus. Two Linear Variable Displacement Transducers (LVDT) have been positioned between the two stiff steel plate adopted to uniformly apply the vertical compressive load on the brick specimens. In each test, three compression cycles have been performed, according to EN 14580[103]. Results are shown in Figure 4.3.

Sample	F max [kN]	σ_{max} [MPa]
Sample 1	4.293	4.330
Sample 2	4.876	4.920
Sample 3	3.230	3.259
Sample 4	5.102	5.148
Mean	**4.375**	**4.414**
CoV	**0.19**	**0.19**

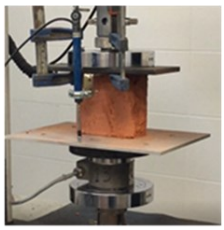

Sample	E [MPa]	F max [kN]	σ_{max} [MPa]
Sample 1	800.128	68.332	11.380
Sample 2	1332.675	89.399	14.890
Sample 3	999.449	96.200	16.035
Sample 4	989.303	81.835	13.639
Mean	**1030.389**	**83.942**	**13.986**
CoV	**0.21**	**0.14**	**0.14**

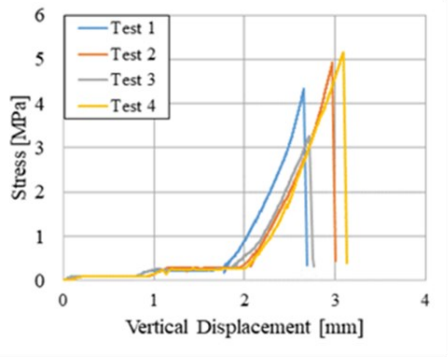

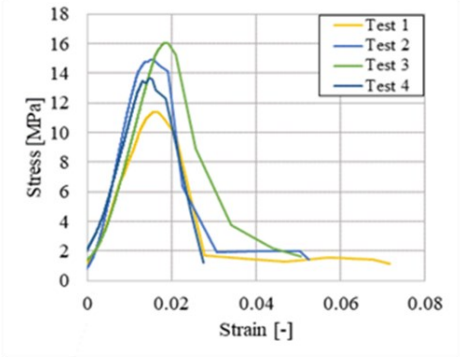

Figure 4.3 Results of three-point bending tests and compressive tests of clay bricks

Lime Mortar Specimens

Six prismatic specimens with dimensions equal to $40 \times 40 \times 160\ mm^3$ have been poured on custom-made iron mold. Four of them have been tested in three-point bending tests and compression tests after 28 days of curing, while the other two have been characterized after 108 days (adopted ages are coincident with the pseudo-dynamic tests on the building). It is worth mentioning that three-point bending tests have been performed according to EN 13412 [104] and EN 1015-11 [105], while compression tests have been conducted following the EN 1015-11 [105]. The determination of the Elastic Modulus has been obtained following the recommendations of EN 14580 [103]. Figure 4.4 shows the experimental set-up adopted to perform the laboratory tests on lime mortar specimens

as well as the force-displacement curves obtained at the end of the investigations. In this case, compression tests have been performed on cubic specimens with dimensions equal to $40 \times 40 \times 40\ mm^3$. Similarly, to clay bricks, the elastic modulus of lime mortar specimens has been calculated.

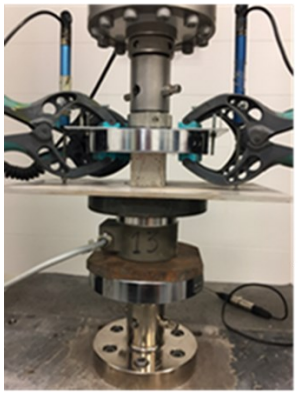

Compression test

Test at 28 days

Sample	E [MPa]	F max [kN]	σ_{max} [MPa]
Sample 1	789.977	6.184	4.105
Sample 2	810.826	5.892	3.899
Sample 3	728.348	7.039	4.658
Sample 4	578.172	6.590	4.333
Mean	**726.831**	**6.426**	**4.249**
CoV	**0.14**	**0.08**	**0.08**

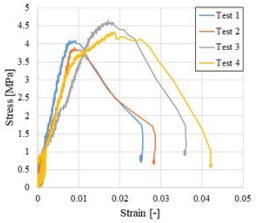

Test at 108 days

Sample	E [MPa]	F max [kN]	σ_{max} [MPa]
Sample 1	922.02	7.40	4.90
Sample 2	1202.06	10.60	7.07
Mean	**1062.04**	**9.00**	**5.98**
CoV	**0.19**	**0.25**	**0.26**

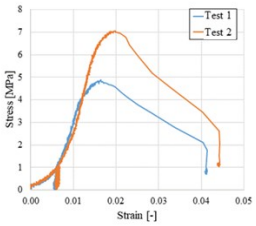

Three points bending test

Test at 28 days

Sample	F max [kN]	σ_{max} [MPa]
Sample 1	0.440	1.110
Sample 2	0.650	1.615
Sample 3	0.708	1.765
Sample 4	0.563	1.417
Mean	**0.590**	**1.477**
CoV	**0.20**	**0.19**

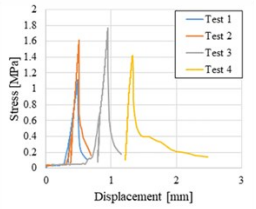

Test at 108 days

Sample	F max [kN]	σ_{max} [MPa]
Sample 1	0.43	1.07
Sample 2	0.49	1.25
Mean	**0.46**	**1.16**
CoV	**0.09**	**0.11**

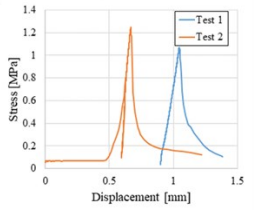

Figure 4.4 Results of three-point bending tests and compressive tests of lime mortar

4.4.2 Textile Reinforced Mortar (TRM) Material

Glass textile

The Textile Reinforced Mortar material adopted during the strengthening of the masonry prototype is composed of a balanced glass grid and two 5 mm thick layers of a cementitious mortar. The glass textile consisted of a 25 mm spacing grid with an equivalent thickness equal to 0.035 mm. The mechanical properties of the textile adopted in the present investigation have been reported in Table 4.1, as declared by the manufacturer [106].

Table 4.1 Mechanical characteristics of glass fiber

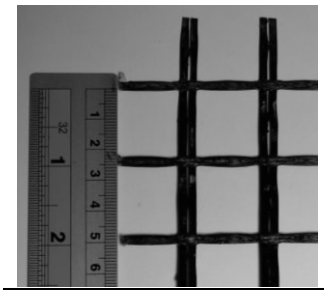	**Mesh size**	25 x 25	[mm]
	Weight	225	[g/mm^2]
	Density of fibre	2.5	[g/cm^3]
	Tensile strength	45	[kN/m]
	Modulus of elasticity	72	[GPa]
	Resistant Area	35.27	[mm^2/m]

Cementitious Mortar

The mechanical properties of the cementitious mortar binder have been characterized by performing a series of laboratory tests, as three-point bending tests and compression tests. Similarly, to the lime mortar, the cement matrix has been poured on an iron mold with dimensions equal to $40 \times 40 \times 160\ mm^3$ and $40 \times 40 \times 40\ mm^3$, respectively considering the three-point bending test and the compression test. The following standards have been used to perform the tests: EN 1015-11 [27] and EN 13412 [26] have been used to perform the three-point bending tests, while compression tests have been developed following the EN 1015-11 [27]. As mentioned above, the calculation of the elastic modulus has been performed following EN 14580[25]. Set up of test were like that adopted for the lime mortar Figure 4.5 shows the force-displacement curves obtained.

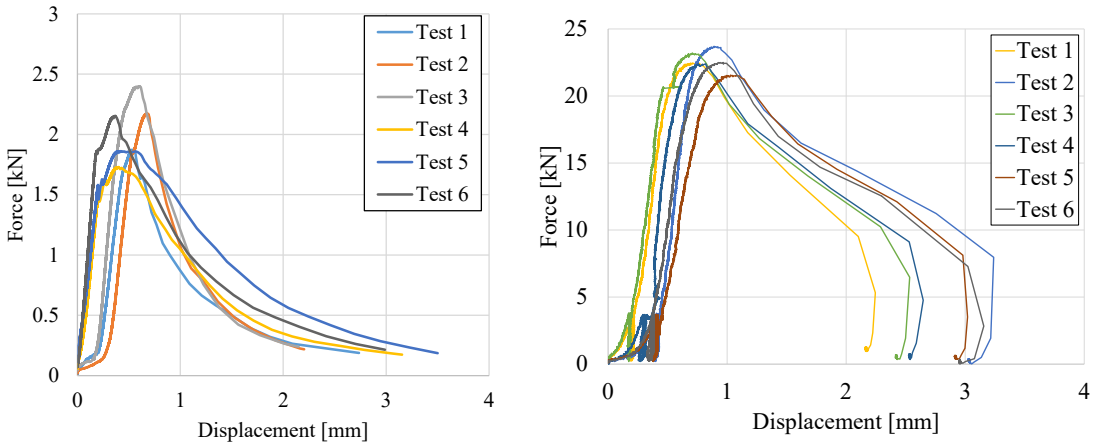

Figure 4.5 Results of three-point bending tests and compressive tests of cementitious mortar

4.4.3 Summary of the results

The experimental outcomes obtained at the end of all the series of laboratory investigations comprising three-point bending tests and compression tests are listed in Table 4.2. In detail, $\sigma_{t,\,max}$ is used in what follows to identify the peak tensile strength

calculated from the ultimate bending moment assuming an elastic behaviour. Concerning the compression tests, $\sigma_{c,\,max}$ has been calculated as the peak compressive strengths obtained dividing the peak experimental force by the loaded surface of the tested specimens [107]. Finally, the Elastic Modulus (E) has been evaluated from the third loading cycle of the stress-strain curves obtained at the end of the compression tests.

Table 4.2 **Mechanical properties of clay bricks, lime mortar, and TRM cementitious mortar.**

CLAY BRICK					
	Three-point bending test		***Compression test***		
		$\sigma_{t,max}$ [MPa]	**Test n.**	**E [MPa]**	**$\sigma_{c,max}$ [MPa]**
	Test 1	4.33	**Test 1**	800.13	11.38
	Test 2	4.92	**Test 2**	1332.68	14.89
	Test 3	3.26	**Test 3**	999.45	16.04
	Test 4	5.15	**Test 4**	989.30	13.64
LIME MORTAR					
At 28 days	**Test 1**	1.11	**Test 1**	789.977	4.11
	Test 2	1.62	**Test 2**	810.826	3.90
	Test 3	1.76	**Test 3**	728.348	4.66
	Test 4	1.42	**Test 4**	578.172	4.33
At 108 days	**Test 1**	1.05	**Test 1**	922.02	4.900
	Test 2	1.23	**Test 2**	1202.06	7.070
TRM CEMENTITIOUS MORTAR					
At 63 days	**Test 1**	4.71	**Test 1**	3949.47	17.10
	Test 2	5.52	**Test 2**	3032.25	17.45
	Test 3	5.79	**Test 3**	3592.14	17.50
	Test 4	4.65	**Test 4**	1573.70	17.25
	Test 5	5.07	**Test 5**	4513.32	16.60
	Test 6	6.15	**Test 6**	2416.45	17.04

A summary of the experimental outcomes is reported Table 4.3. As clearly visible, Table 4.3 lists the average of the peak tensile and compressive strengths obtained experimentally as well as the average of the Elastic Modulus calculated as mentioned above.

Table 4.3 Summary of the mean properties obtained testing clay bricks, lime mortar, and TRM cementitious mortar. In brackets the CoV values.

	E_{mean}[MPa]	$\sigma_{c,max}$ [MPa]	$\sigma_{t,max}$ [MPa]
Clay Brick	1030.39 (0.21)	13.99 (0.14)	4.42 (0.19)
Lime mortar (28 days)	726.83 (0.14)	4.25 (0.08)	1.48 (0.19)
Lime mortar (108 days)	1062.04 (0.19)	5.98 (0.26)	1.14 (0.11)
TRM Cementitious mortar (63 days)	3179.56 (0.65)	17.16 (0.22)	5.32 (0.20)

4.4.4 Tests set up

The masonry structure has been subjected to a series of pseudo-dynamic cycles through a servo-hydraulic jack positioned on the free edge of the U-shape masonry construction, it generated the cycles by imposing positive (Push) and negative (Pull) displacements. To analyse the effect of the dynamic excitation on the masonry construction, the horizontal loads have been applied using a stiff steel beam connecting the two lateral walls and the horizontal jack. The torsional effect of the masonry building due to the different stiffnesses of the lateral walls has been also considered placing a cylindrical hinge between the steel beam and the hydraulic jack. The load during tests was recorded using a load cell between the hydraulic jack and the hinge. A total of 26 and 19 series of dynamic excitations, lasting 10 seconds each one, have been applied to the masonry prototype considering respectively the unreinforced (URM) and TRM strengthened construction (RM). Table 4.4 summarizes the two experimental investigations developed as well as all the series of dynamic excitations carried out. Furthermore, it describes the maximum displacement imposed by the hydraulic jack and the corresponding frequency of the excitation during each test.

Table 4.4 Summary of the dynamic excitations applied on the as-built and TRM reinforced construction.

URM Structure			TRM Structure		
Series of dynamic excitation	**Maximum displacement [mm]**	**Maximum frequency [Hz]**	**Series of dynamic excitation**	**Maximum displacement [mm]**	**Maximum frequency [Hz]**
1	+/- 0.2	1.8	1	+/- 0.2	2
2		3.6	2		3.5
3		5.3	3		5.1
4		5.9	4		5.7
5		7.7	5		7.5
6		9.1	6	+/- 0.5	1.8
7	+/- 0.5	1.8	7		3.4
8		3.5	8		5.8
9		4.3	9	+/- 1.0	1
10		5.4	10		2.2
11		5.7	11		3.3
12		6.0	12	+/- 2.0	1
13	+/- 1.0	1.0	13		1.8
14		1.7	14	+/- 4.0	0.7
15		2.8	15		0.9
16		3.4	16	+/- 6.0	0.6
17		3.4	17	+/- 8.0	0.5
18	+/- 2.0	1	18	+/- 10.0	0.4
19		1	19	+/-12.0	0.3
20		1.8			
21		1.8			
22	+/- 4.0	0.7			
23		1.0			
24	+/- 6.0	0.7			
25	+/- 8.0	0.5			
26	+/- 10.0	0.4			

Many sensors were installed on the structure: 8 piezoelectric accelerometers, 28 Linear Variable Displacement Transducers (LVDTs), and 3 optical displacement sensors. The sensors' locations are shown in Figure 4.6**,** the LVDT's are put where the cracks common appeared on openings' corners and between the transversal walls and the façade. Four LVSTs are also on the upper corners of the structure to control the global behaviour of as well as the possible torsional effect during the dynamic excitation.

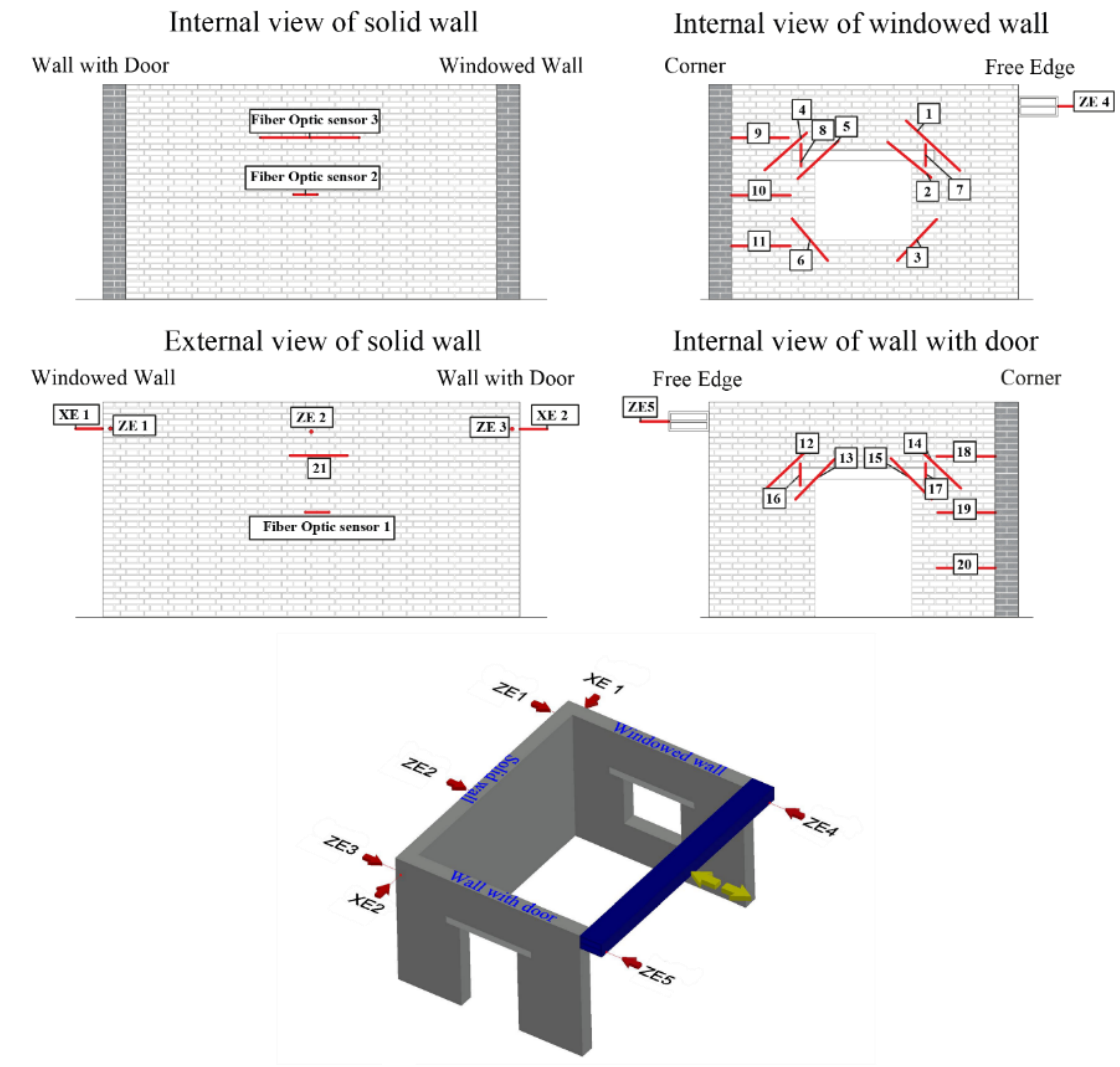

Figure 4.6 Location of the 28 LVDTs and the three fiber optic sensors

4.5 Experimental results

The improvement given by the TRM is evaluated comparing the experimental results using frequencies and modal shapes variation, Force-Displacement curves, Secant Stiffness Degradation and Crack mechanism.

4.5.1 Dynamic characterization tests

In a previous work [108], ambient vibration tests were performed to investigate the dynamic characteristics of the structure in different scenarios (i.e. as-built before and after damage, and repaired and reinforced before and after damage). The results of these tests, in addition to providing an assessment of the current characteristics of the structure, if compared can give an estimate of the damage suffered from the application of the thrusts, and on the improvement brought about by the application of the reinforcement. The

monitoring was carried out using eight mono axial piezometric accelerometers (PCB 352C04) with sensitivity 10 mV / g, dynamic range ± 0.5 g and a bandwidth ranging from 0.5 Hz to 1000 Hz, attached to the structure with screw connectors. The wired sensors sent the signal to a Kyowa PCD-320 data acquisition device and a PCB 482A22 signal conditioner. In each configuration, two ambient vibration tests were performed lasting five minutes each and with a sampling rate of 1000 Hz. The sensors' layout is showed in Figure 4.7 (referred to as "An", where n identifies the number of the sensor). The sensors loacations were chosen on the points where the greatest displacements were expected.

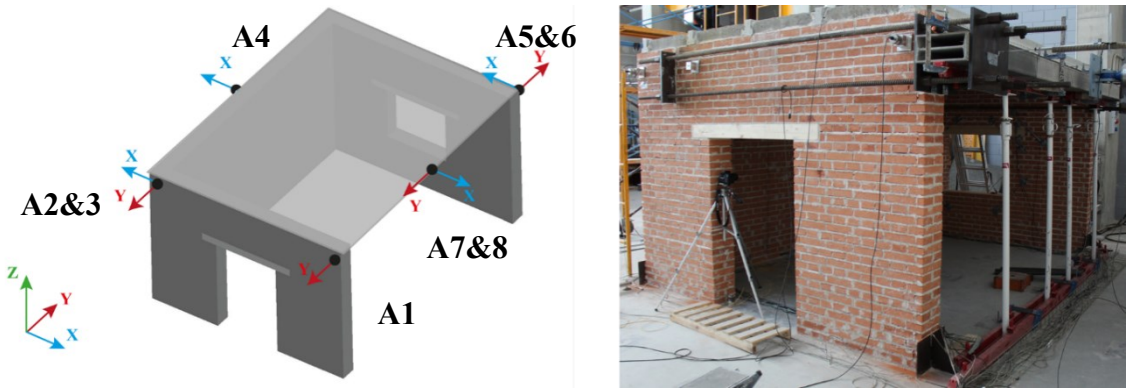

Figure 4.7 Accelerometers sensors layout

ARTeMIS software was used to obtain the dynamic parameters. The frequencies and modal shapes were obtained with Enhanced Frequency Domain Decomposition (EFDD) after the signals were suitably cleaned, filtered and decimated between 0-500Hz. The results extracted from Bru et al. (2019) were used in the present study to calibrate the subsequent FE model. The frequencies and damping recorded for each configuration are summarized in Table 4.5, which gives an average reduction of the frequencies equal to 29% and 42% for the URM and TRM structures between the pre-damage and damage scenarios, respectively. This reduction reflects the loss of stiffness due to cracking. Comparing the URM and TRM pre-damage scenarios, it can be seen that the TRM brought about a slight increase in frequencies of about 6% for the 1st, 2nd and 4th modes, while a substantial decrease of about 26% was recorded for the 3rd mode. In Figure 4.8 modal shapes of the structure pre-damage without reinforcement and post-damage with reinforcement are showed.

Table 4.5 Frequencies and damping of the unreinforced and reinforced structures considering different test scenarios.

Structures / Scenarios	Unreinforced structure				TRM Reinforced structure			
	Pre-damage		Post-damage		Pre-damage		Post-damage	
Results	Freq. [Hz]	Damping [%]	Freq. [Hz]	Damping [%]	Freq. [Hz]	Damping [%]	Freq. [Hz]	Damping [%]
1st mode	13.728	2.41	10.375	4.26	14.461	1.23	9.613	3.32
2nd mode	22.539	1.53	16.507	3.46	24.517	1.51	15.854	2.35
3rd mode	38.507	0.74	25.636	2.19	48.647	0.35	24.429	1.39
4th mode	65.097	0.50	45.445	0.86	68.517	0.69	35.210	1.16

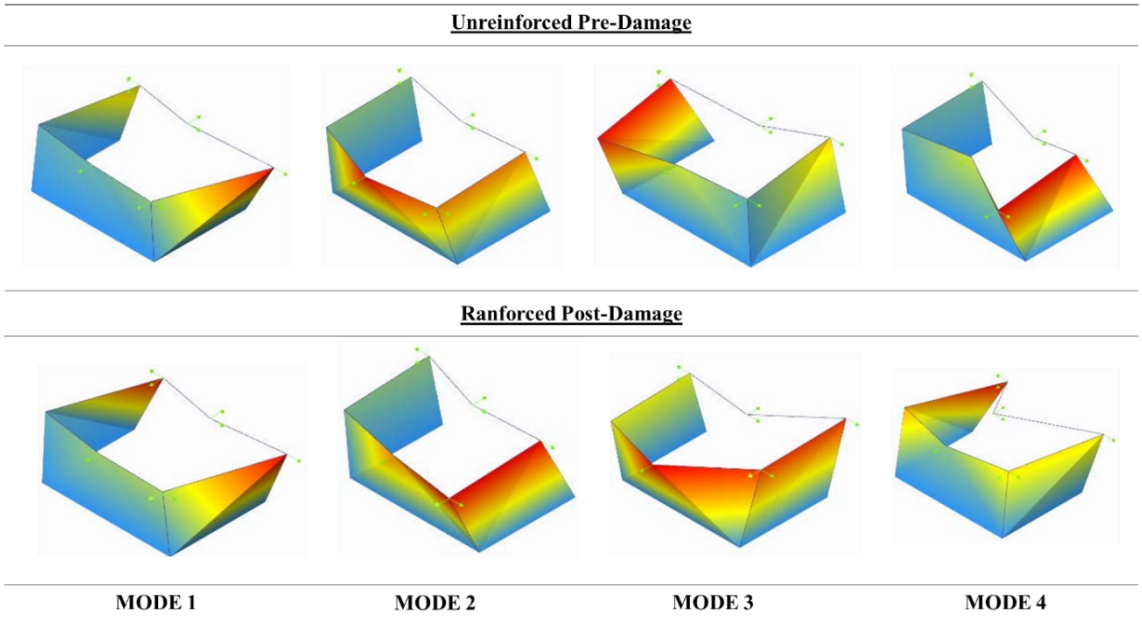

Figure 4.8. Modal shapes of the undamaged unreinforced structure and the damaged reinforced structure.

4.5.2 Force-displacement curves

To identify the influence of the TRM on the structure, the hysteresis cycles plotted in Figure 4.9 were used, considering the displacements recorded by the four LVDTs on the top corners and the forces recorded by the load cell. From a first observation of the hysteretic cycles, a clear transition from an elastic to an anelastic behaviour is identified for a displacement equal to +/- 4 mm and a frequency of 4 Hz (test 22), while for the reinforced structure this is visible for one displacement of +/- 6 mm and a frequency of 0.64 Hz (test 16). This step indicates a reduction in stiffness which is justified by the widening of the cracks. As expected, such a transition is delayed when analyzing the behavior of the TRM reinforced structure.

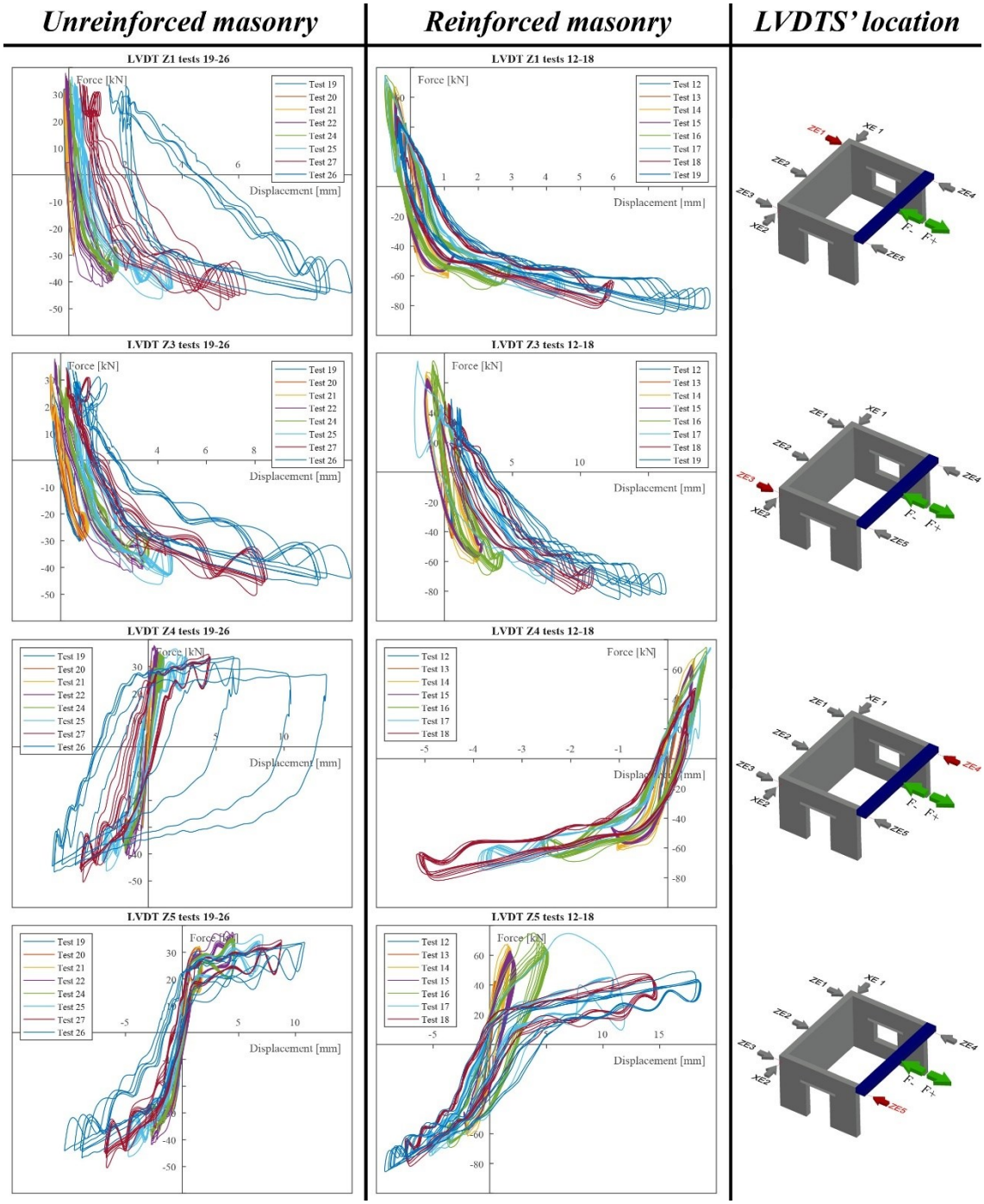

Figure 4.9 Hysteretic curves obtained from LVDT Z1, LVDT Z3, LVDT Z4, and LVDT Z5.

Figure 4.10 depicts the force-displacement curves presented in Figure 4.9 superposed with the experimental envelopes and the calculated idealized elastic-plastic responses [109]. The grey dashed lines represent the hysteretic curves obtained during the whole investigation, whereas the dashed blue and red lines refer respectively to the envelopes constructed considering the as-built structure and the TRM strengthened one. The envelopes curves have been obtained connecting the points characterized by the

maximum force in each cycle, and the corresponding displacements recorded by the LVDTs. The equivalent bi-linear response, instead, is drawn by three parameters, namely: the critical force, the ultimate force, and finally the ductility. The critical force, herein labeled as F_{cr}, corresponds to the 70% of the peak force obtained from the envelopes considering independently the push and pull directions. Similarly, the ultimate force (F_u) has been computed as 90% of the peak force. These two parameters have been associated with a displacement capacity of the structure. In detail, F_{cr} has been used to calculate the elastic displacement (d_e), while F_u has been adopted to find the ultimate displacement, stopping the plot when the force decreased by 80% (d_u). The values corresponding to the four LVDTs mentioned above have been listed in Table 4.6. Comparing the URM behavior with the TRM one, it is visible an increment of the peak forces equals to approximately 69% considering the push direction and 97% for the pull one.

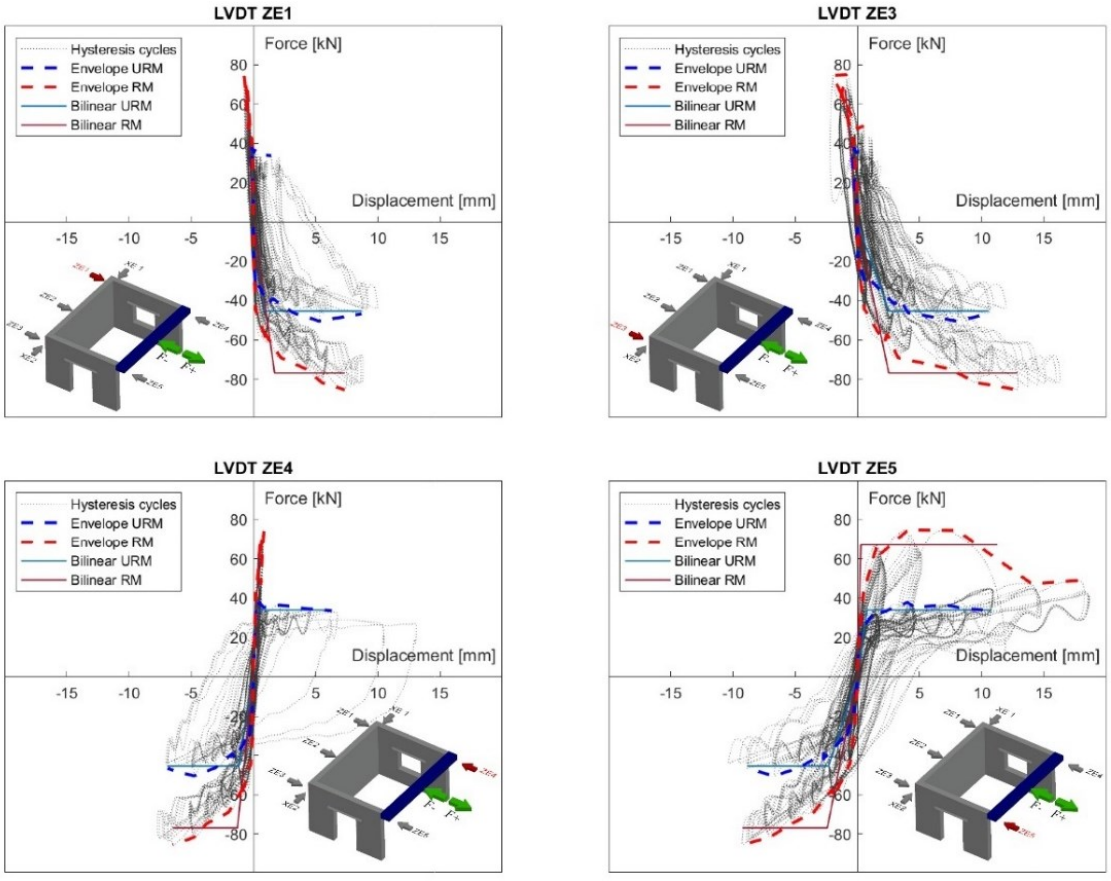

Figure 4.10 Superposition between experimental force-displacement curves, experimental envelopes and idealized elastic-plastic response obtained considering LVDTs Z1, Z3, Z4 and Z5.

Table 4.6 Parameters adopted to generate the idealized elastic-plastic response of the tested structure

Struture	Direction	F_{max} [kN]	F_{cr}=70% F_{max} [kN]	F_u=90% F_{max} [kN]
URM	**Push**	50.48	35.34	45.44
	Pull	37.82	26.34	34.04
TRM	**Push**	84.66	59.26	76.20
	Pull	74.88	52.42	67.40

4.5.3 Secant stiffness degradation

The secant stiffness degradation is obtained as the ratio between the maximum force recorded in each series of dynamic excitation and the corresponding displacement in both directions. Figure 4.11 depicts the secant stiffness degradation calculated as mentioned above considering only the LVDTs Z4 and Z5 for both push and pull directions. To allow a better evaluation of the effect of the TRM reinforcement, the values calculated considering the URM building have been plotted in blue and have been superimposed to the red ones computed considering the presence of the strengthening. The maximum stiffness of 916.38 kN/mm has been obtained for the TRM reinforced structure at an imposed displacement of 0.2 mm considering LVDT Z4 in the pull direction. Whereas, LVDT Z5 recorded a maximum value equal to 478.86 kN/mm at 0.5 mm in the push direction. The secant stiffness gradually decreased during the experimental tests, probably due to the formation of the cracking mechanisms (See Section 4.5.4). These trends can be observed both in the URM and in the reinforced masonry structure. It is also important to underline that, the presence of the TRM produced a not negligible increment of the stiffness visible in each set. In addition, comparing the stiffnesses recorder by LVDTs Z4 and Z5 it is possible to note that the masonry structure showed the development of torsional effects. As expected, the elastic stiffnesses calculated considering the LVDT Z4 showed always bigger values with respect to LVDT Z5. This can be justified by the opening ratio of the panel with the door which is almost double concerning the windowed wall.

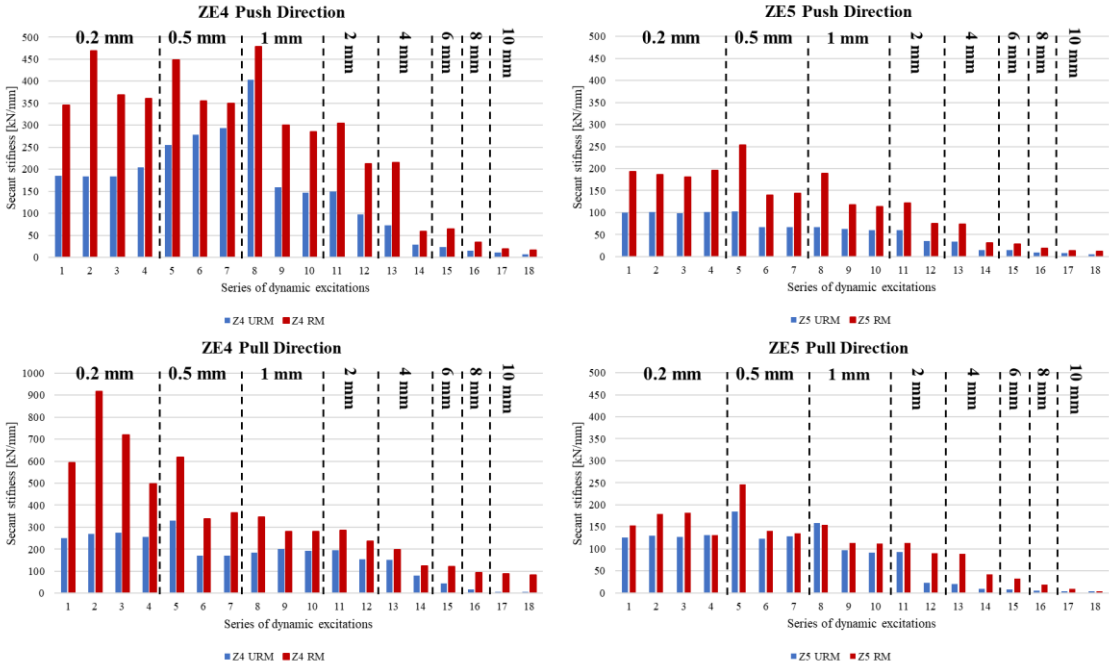

Figure 4.11 Stiffness degradation obtained considering LVDTs Z4 and Z5

4.5.4 Cracking mechanism

As showed in Figure 4.11, during the two tests the building evidenced a progressive degradation of the secant stiffness which has been probably produced by the formation of a cracking mechanism. This behaviour is also confirmed by the plots in Figure 4.12. Indeed, Figure 4.12-a shows the cumulative variation of the displacement (herein labeled as residual displacement) read at the beginning and the end of each set of excitation monitored by six LVDTs namely LVDTs 1-3-4-6-12 and 14. When the relative displacement is different from zero, an inelastic deformation takes place with the probable widening of cracks.

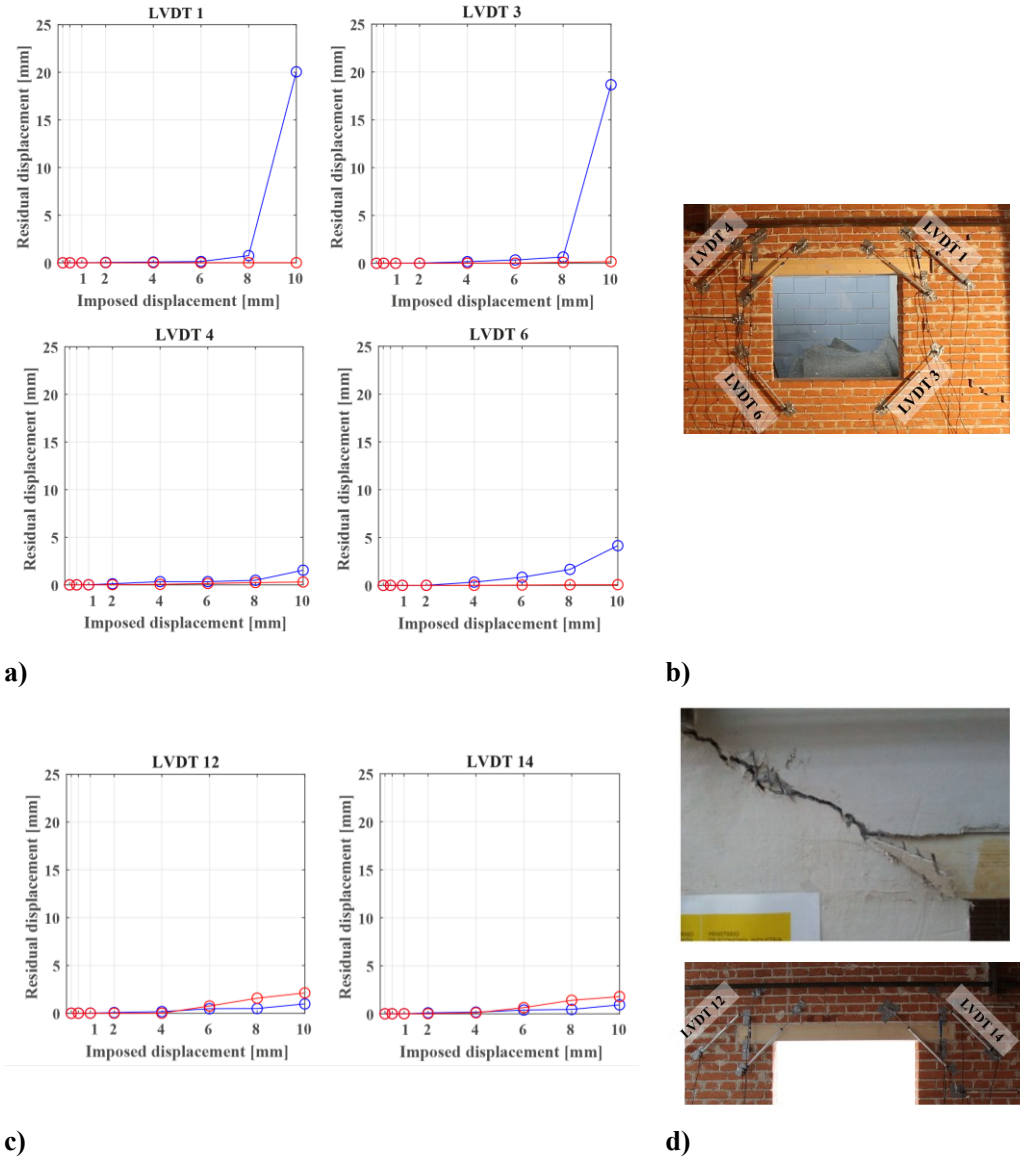

Figure 4.12 Residual displacements read by LVDT 1-3-4-6-12 and 14 (a), the crack pattern of the URM structure in the windowed wall (b), and of the TRM strengthened masonry in the door wall (c).

As clearly visible from Figure 4.12-a, the inelastic behaviour of the URM building has been captured by LVDTs 1 and 3 reaching 20 mm of displacement. It is worth mentioning that, LVDTs 1 and 3 are two of the sensors placed at the top and bottom right corners of the windowed panel. As visible in Figure 4.12-b and Figure 4.13-a-b, that wall experienced the formation of stepped cracks along both head and bed mortar joints which developed from the corner of the window to the free edge of the building. A similar behavior characterized by the opening of stepped cracks has been noted on the corners of the windowed wall near the solid transversal wall. In that case, the residual displacements

read by LVDTs 4 and 6 reached lower values probably due to the presence of this solid transversal wall (see Figure 4.12-b). Globally, the TRM reinforced building behaved better due to the effect of the reinforcement which can extend the elastic limit of the construction increasing the collapse loads of the masonry. Indeed, no cracking mechanisms have been observed along the windowed wall when considering the strengthened structure.

Conversely, LVDTs 12 and 14, which have been placed on the opposite side of the building (wall with door) (see Figure 4.12-c), monitored a different behavior. As a matter of fact, the higher values of the residual displacements have been observed for the TRM reinforced structure. It is also important to underline, that due to the torsional effect of the building the displacements at which the wall with the door was subjected were bigger respect to the windowed wall. This provoked the different behaviour between URM and TRM construction. For the URM, a delay in the formation of the cracking mechanism in the panel with the door was registered, precede by the widening of cracks in the windowed wall (see Figure 4.12-a and –b). For the TRM construction, no cracks were identified in the windowed wall, whereas displacements and cracking were accumulated in the panel with the door (See Figure 4.12-c). In the latter, the failure mechanism was characterized by the formation of finer cracks in the mortar binder and then a partial tensile failure of the glass fiber was observed. From Figure 4.13.a it is noted that the structure under large displacements also underwent a sliding at the base.

Figure 4.13 Cracking pattern at the end of the tests for unreinforced (a-b) and reinforced (c-d) structures

4.6 Numerical analysis

To further investigate the influence of the mechanical properties and the efficiency of TRM reinforcement, an FE model was calibrated from the experimental data. This section describes the FE model, the calibration carried out with the help of the ambient vibration results, and the parametric static nonlinear study performed.

4.6.1 Finite element model

The numerical models were created by Midas FEA NX Software [101]. The geometry of the masonry, lintels, plates, and steel beam was carefully reproduced and subsequently discretized with four-node tetrahedral elements with a size of 0.1 m (the value was chosen based on a study on a structure of similar size [110]). Tie rods and props were modeled as truss elements, considering the former non-reactive to compression and the latter non-reactive to tension. In total, the URM model featured 43100 elements, 34146 degrees of freedom, and 11020 nodes (Figure 4.14.a). The TRM reinforced structural model was created by URM one and adding the TRM strengthening material using an ambitious modeling technique consisting of two layers of solid tetrahedral elements for the mortar,

interspaced by membrane elements to represent the fiberglass mesh. In total, the TRM-reinforced structural model consisted of 57288 elements, 56220 degrees of freedom, and 17247 nodes (Figure 4.14.b).

The one-way roof slab was considered as a superimposed additional mass which unloads 95% of the weight on the sidewalls and 5% on the façade wall. The adopted boundary conditions comprised the constraining of: (i) translations along x, y, and z directions simulating the anchoring bottom steel plates, and (ii) all degrees of freedom in correspondence of the tie rods.

Wood lintels were considered elastic throughout the study with an elastic modulus of 15 GPa, Poisson's ratio equal to 0.4, and a density of 380 kg/m^3. Similarly, steel elements were also considered elastic with an elastic modulus of 210 GPa, Poisson's ratio 0.3, and density 7850 kg/m^3.

The linear parameters of the masonry were deduced from laboratory tests on the individual components Table 4.3. The elastic modulus was estimated as $E = 1000\ f_c$, where f_c was calculated with Eq. (4.1), i.e. using the formulation of Eurocode 6 (EN 1996-1-1 2005), where K is a constant that depends on blocks and mortar (in this case equal to 0.45 considering traditional joints) f_b the compressive strength of the block and f_m the compressive strength of the mortar:

$$f_c = K\ f_b^{0.7}\ f_m^{0.3} \tag{4.1}$$

Considering the parameters listed above, f_c was estimated equal to 4.41 MPa, while the elastic modulus was 4410 MPa.

The masonry's density was taken equal to 1656 kg /m^3. The masonry nonlinear behavior was represented by the Concrete Smeared Crack Model (CSCM) [111] attributing suitable constitutive laws to tensile (Hordijk), compression (parabolic), and shear (linear) responses (Figure 4.14.c).

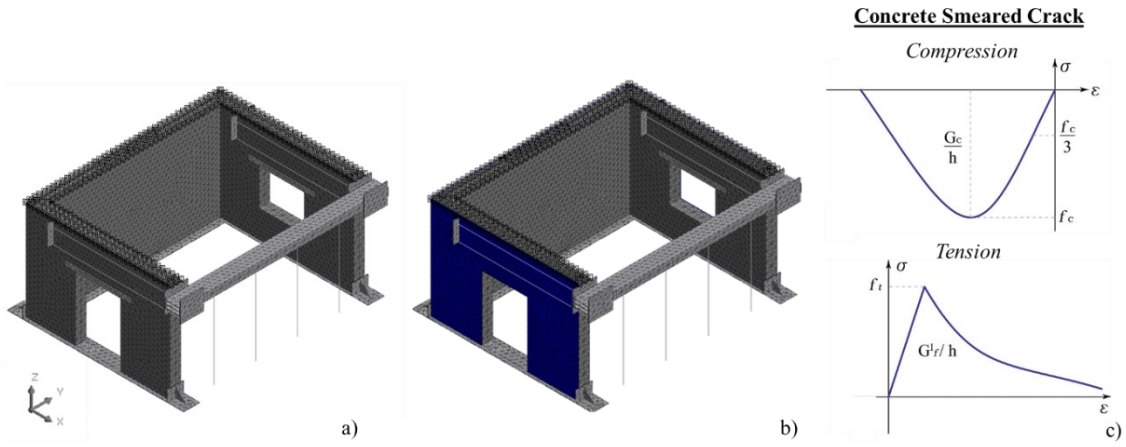

Figure 4.14. Numerical model for URM (a) and RM structure(b), and nonlinear constitutive laws assigned to masonry (c)

4.6.2 Calibration of the numerical model

The calibration of the elastic modulus of the as-built structure (corresponding to the undamaged URM scenario) was carried out through the ambient vibration test results. The mechanical parameters given in the previous subsection were first employed. Starting from the undamaged and unreinforced numerical model, the modal parameters were evaluated based on the ambient vibration tests (Section. 4.5.1). obtaining the frequencies and modal shapes shown in Figure 4.15 for the four experimental modal shapes.

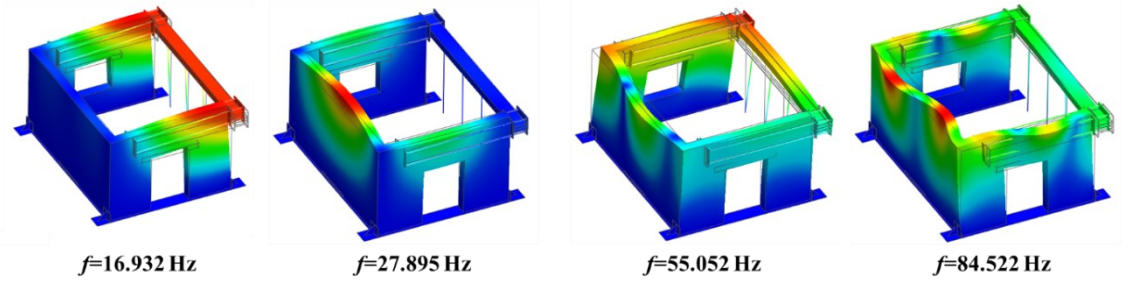

Figure 4.15. Modal shapes and frequencies of the URM with the elastic parameters directly obtained from the experimental tests

In comparison with the experimental frequencies (see Table 4.7), the frequencies have an average deviation of 30%. The 3rd vibration mode had a maximum deviation with a percentage difference of 43 (Table 4.7).

Table 4.7. Comparison between the experimental frequencies and those obtained from the starting numerical model

Mode	f_{exp}[Hz]	f_{num}[Hz]	Δf [%]
1st	13.73	16.93	23%
2nd	22.54	27.90	24%
3rd	38.51	55.05	43%
4th	65.10	84.52	30%

To improve the correlation between the experimental and numerical results, it was necessary to reduce the masonry elastic modulus to 2727 MPa (38%). It was then possible to obtain deviations of less than 5% for the frequencies of all modes except the 3rd, which presented a percentage difference of 15% (see Table 4.8). The numerical modal shapes depicted in Figure 4.16 fit well with those experimentally recorded (Figure 4.8[108]).

Table 4.8. Comparison between the experimental and numerical frequencies of the undamaged URM model after calibration

URM undamaged updating model		
f_{exp} [Hz]	f_{num} [Hz]	Δf [%]
13.728	13.712	0%
22.539	22.421	1%
38.507	44.104	15%
65.097	67.338	3%

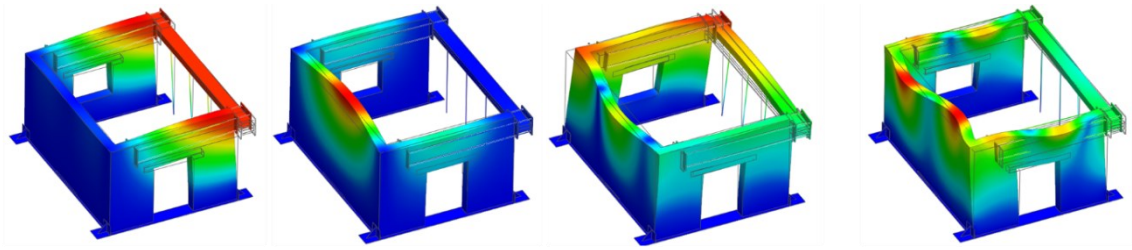

Figure 4.16. Modal shapes and frequencies of the calibrated numerical model of the as-built structure

The author then analyzed the following scenario, which comprised the restoration of the initial conditions of the URM damaged structure after repairing the cracks and then applying an external layer of TRM materials. The numerical model used to simulate this situation is that calibrated by the unreinforced pre-damage structure to which the TRM was applied, assuming the individual material's characteristics to be as reported in Table

4.1. Table 4.9 summarizes the results obtained in terms of experimental and numerical frequencies and their differences, showing a good correlation. Figure 4.17 shows the numerical modal shapes obtained.

Table 4.9. Comparison of the experimental and numerical frequencies of the pre-damage RM structure

RM pre-damage updating model		
fexp [Hz]	*fnum* [Hz]	Δf [%]
14.461	14.461	3%
24.517	24.517	0%
48.647	46.915	4%
68.517	72.473	6%

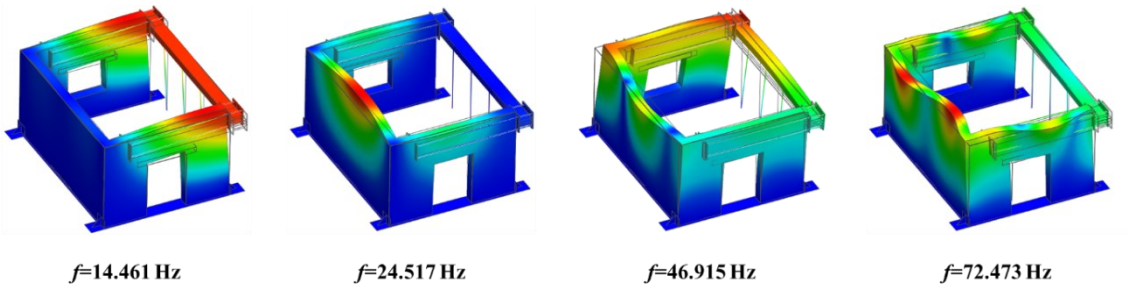

Figure 4.17. Modal shapes and frequencies of the numerical model of the pre-damage RM structure

4.6.3 Nonlinear static analysis

Following the identification of the main dynamic characteristics of the structure subjected to four damage and reinforcement scenarios, a parametric study with the non-linear mechanical parameters was performed using non-linear static analysis for three different purposes: (i) to analyze the structural response with different mechanical parameters, (ii) to determine the most appropriate combination of parameters to reproduce the experimental behavior, and (iii) to evaluate the effectiveness of the TRM reinforcement technique.

In addition to the described model and that used for the modal analysis, the effect of the jack connected to the steel beam was also simulated by locking the translational and rotational degrees of freedom of the nodes in the middle of the steel beam (except for the rotation around the vertical axis). At this point, the maximum displacements imposed during the tests were then assigned and raised monotonously. The analyses were carried

out in displacement control divided into 50 steps with a maximum number of 200 iterations using the Full Newton-Raphson solution procedure.

The first URM analysis was performed to identify the correct nonlinear masonry parameters. The initial values of the nonlinear parameters were obtained as a function of the elastic modulus that allowed the frequency calibration cited in Section 4.5.1. The compressive strength of the masonry (f_c) was estimated as 1‰ of Young's modulus [26], the tensile strength was firstly evaluated as 10% of f_c, and the fracture energies were estimated according to the classic formulas for concrete [102], which have also been shown to appropriately describe masonry behaviour [112,113]. The values assigned to the starting model are shown in Table 4.10.

Table 4.10. Parameters used to initially define the nonlinear constitutive laws of the URM structure

E [MPa]	f_c [MPa]	f_t [MPa]	G_c [N/mm]	G_f [N/mm]
2727	2.727	0.273	2.336	0.023

The capacity curves were extracted as in the experimental tests, considering the horizontal reaction of the nodes representing the jack and the displacements of the control points taken in the positions of LVDTs ZE1-ZE3-ZE4-ZE5, considering only the push direction.

Figure 4.18 shows the curves (in blue) obtained with the nonlinear values initially assumed (Table 4.10). The displacements are seen to be comparable with the experimental ones (in red) while the resistance is much greater than that registered experimentally.

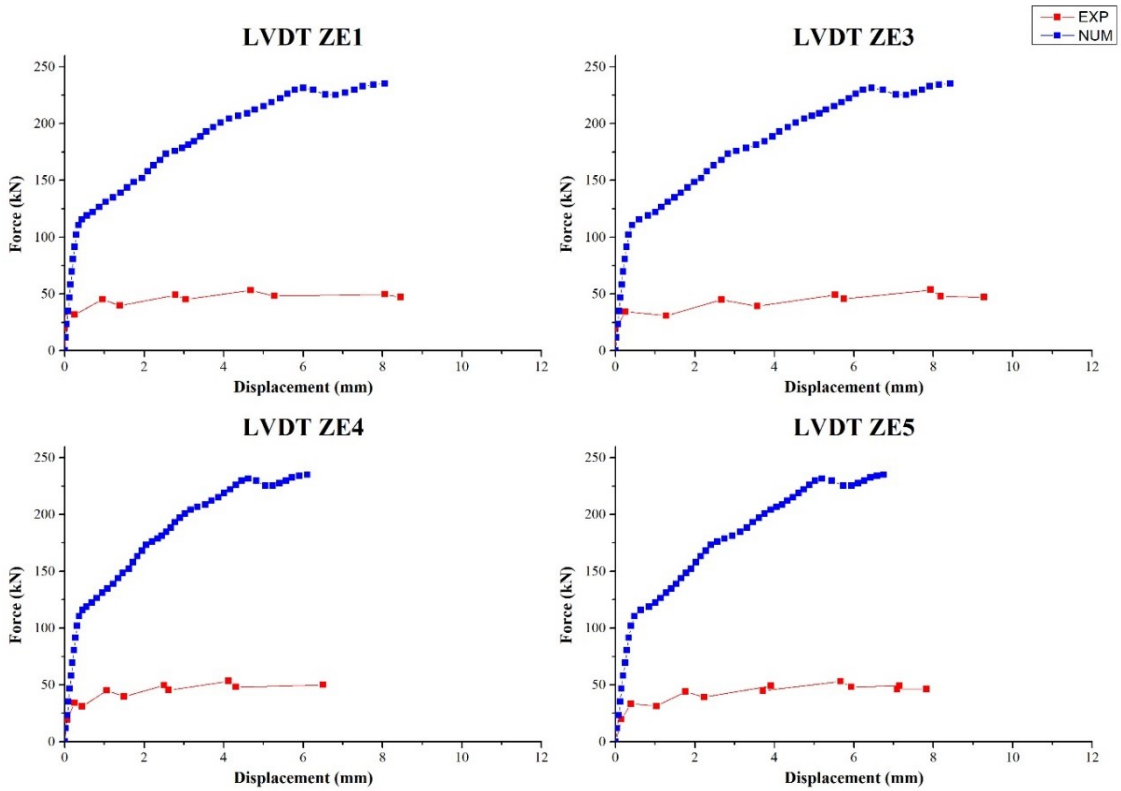

Figure 4.18. Comparison between experimental and numerical curves with the deduced starting parameters of URM structure

For a better understanding, a parametric analysis was performed based on the response of the structure, taking as a reference to the curve of the LVDT ZE4 (red curve in Figure 4.19). Firstly, several non-linear analyses were performed for the parameters f_t, f_c, G_f, and G_c, varying one parameter at a time by 2.5% increases/reductions compared to the starting values, reaching no significant influence on the structural response. Larger reductions were then considered for each parameter. Figure 4.19 shows an example of the structural response when varying one parameter at a time with a value of 20% of the starting value (80% reduction).

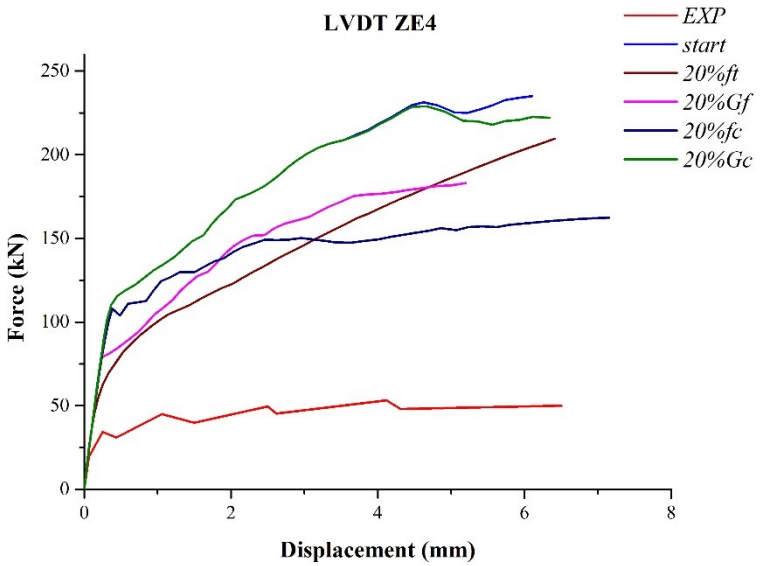

Figure 4.19 Influence of nonlinear parameters on the structural response of the URM structure

The compressive fracture energy G_c is the parameter that has less influence, and which only induces variations in the final part of the curve at high damage levels (governing parameter). A variation in the tensile fracture energy, G_f, reduces the overall ductility and force. Comparing the results, it can be seen that the f_t reduction produces a moderate variation in resistance but allows a marked hardening behavior.

The reduction of only the masonry tensile strength f_t to the value given in Table 4.11 (0.016 MPa) made it possible to adjust the force and displacement values until the stiffness was significantly changed in the test (displacements of LVDTs around 1 mm). This can be explained by the reduced tensile strength of the interface between mortar and bricks after cracking.

Subsequently, after stiffness changed, with several cracked and failed sections in the experimental test, only by varying the value of more parameters was it possible to fit the numerical results to the experimental readings. This can be explained by the almost free movement of the damaged/broken masonry structure. From this point on, the numerical modeling became pointless, although it could have been reproduced numerically by varying other parameters, such as compressive strength f_c, tensile fracture energy G_f and compressive fracture energy G_c. f_c and G_f were first varied to reduce the maximum force recorded in the numerical plastic field. G_c was also reduced to adjust the softening branch.

The nonlinear mechanical parameters obtained are shown in Table 4.11, while Figure 4.20 contains the numerical and experimental curves. Figure 4.20 also shows the strain maps for different points of the numerical response (green, orange, and black) as representative of the computed structural damage.

Table 4.11. Nonlinear parameters of the masonry which allowed to calibrate the experimental curves of URM structure

E [MPa]	f_c [MPa]	f_t [MPa]	G_c [N/mm]	G_f [N/mm]
2727	0.163	0.016	0.1	0.012

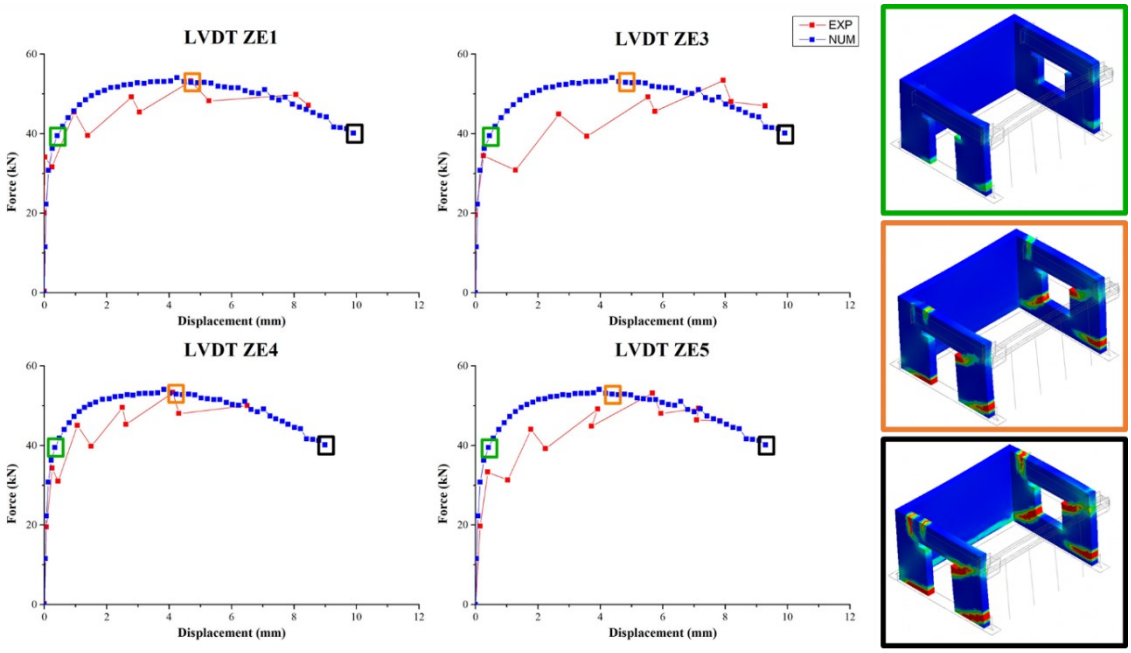

Figure 4.20. Comparison between experimental and numerical curves with updated nonlinear parameters of URM structure

The next step comprised: (i) the application of the final mechanical parameters obtained by the URM model (Table 4.11) to simulate the behavior of the TRM reinforced structure; and (ii) the comparison with the capacity curves of the second experimental test. The nonlinear behavior of the strengthening was simulated by adopting the Concrete Smeared Crack Model (CSCM), attributing only brittle tensile behavior to the fiber and the matrix parabolic behavior in compression and Hordjik in tension, as in the URM analysis. The parameters used (Table 4.12) in the model were assumed to be equal to the experimental values or data sheets and those adopted in Ismail and Ingham (2016). The fracture energies for the matrix (see Table 4.12) were deduced using [102]. Comparing the new numerical curves and experimental TRM reinforced structure curves, it can be seen that

the two responses show a clear hardening behavior with the numerical model giving stronger values than the experimental data. Figure 4.21.

Table 4.12. Initial parameters adopted for the TRM-reinforced structure

FIBER			MATRIX			
E_f [MPa]	f_t [MPa]	E_m [MPa]	f_c [MPa]	G_c [N/mm]	f_t [MPa]	G_f [N/mm]
72 000	1276	8000	15	7.04	0.8	0.077

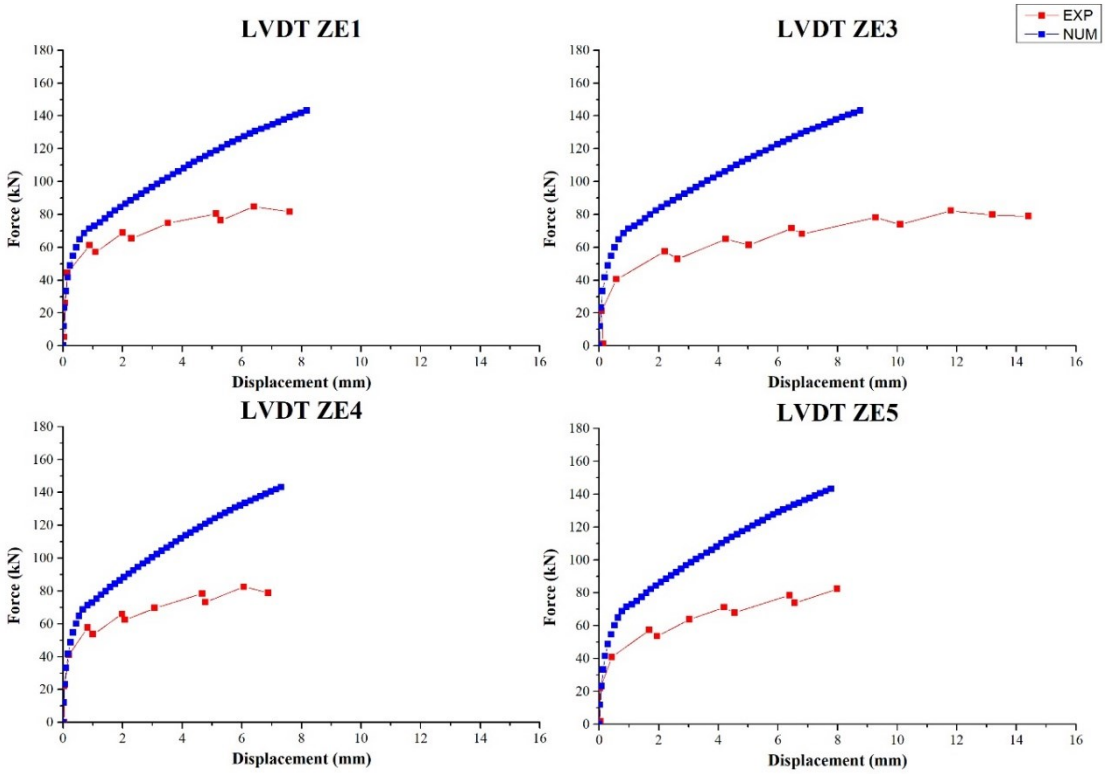

Figure 4.21. Comparison of experimental and numerical curves with initial parameters of the TRM structure

It was thus necessary to proceed with the parametric analysis by updating the mechanical parameters and evaluating the influence of each one on the post-elastic behavior of the reinforced structure, leaving the parameters of the underlying unreinforced masonry unchanged.

Some of the results of the parametric analysis are reported in Figure 4.22 considering an 80% reduction of the properties listed in Table 4.12 and varying only one at a time. Given the influence of the TRM mechanical parameters (see Figure 4.22) and the differences of the experimental and numerical values, the influence of the TRM elastic modules on the

overall behavior of the structure was also analyzed. As expected, variations of E_f affect the slope of the plastic branch, since the matrix, in this case, is no longer reactive while the variations of E_m affect the entire curve since it acts on the initial slope.

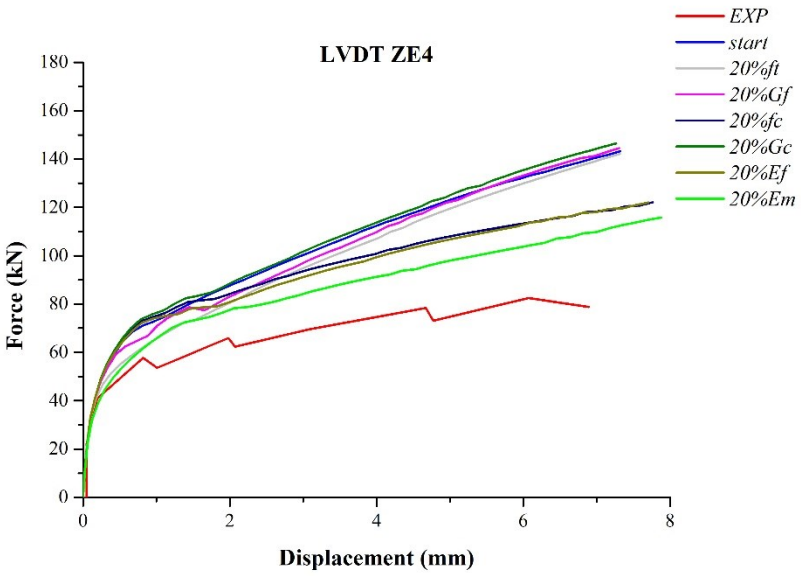

Figure 4.22. Influence of reinforcement parameters on the overall response of the TRM reinforced structure

The next step is represented by the combined variation of the parameters to fit the experimental curve. Considering TRM only, f_t was reduced to better fit the first part of the curve, followed by a reduction in f_c to better fit the numerical plastic part of the curve. As the variation of these two parameters was not enough to reproduce the experimental curves, it was taken into account that at a certain point the fiber had delaminated in various areas of the reinforced surface. In order not to introduce further finite elements, in particular the interfaces that would only be a burden to the analysis process without real advantages, it proceeded with a non-linear static analysis with construction stages in which it disconnected various areas according to the events during the experimental tests as recorded on the videos. The criterion used to select the disconnected areas followed what occurred in the test itself by watching the many available video recordings. The final result is shown in Figure 4.23, while the mechanical parameters that allowed this response and the good correlation between the numerical model and the experimental results are shown in Table 4.13

Table 4.13. Final parameters adopted for the TRM reinforced structure

FIBER			MATRIX			
E_f [MPa]	f_t [MPa]	E_m [MPa]	f_c [MPa]	G_c [N/mm]	f_t [MPa]	G_f [N/mm]
72 000	1276	8000	3	7.04	0.1	0.077

Figure 4.23 compares the numerical and experimental responses showing a good correlation. It also shows the strain maps for different points of the numerical response (green, orange, and black) as representative of the computed structural damage. Overall, the application of the TRM reinforcement improved the hardening behavior with a notable increase of 30% in the maximum force compared to the unreinforced case (see Figure 4.20 and Figure 4.23).

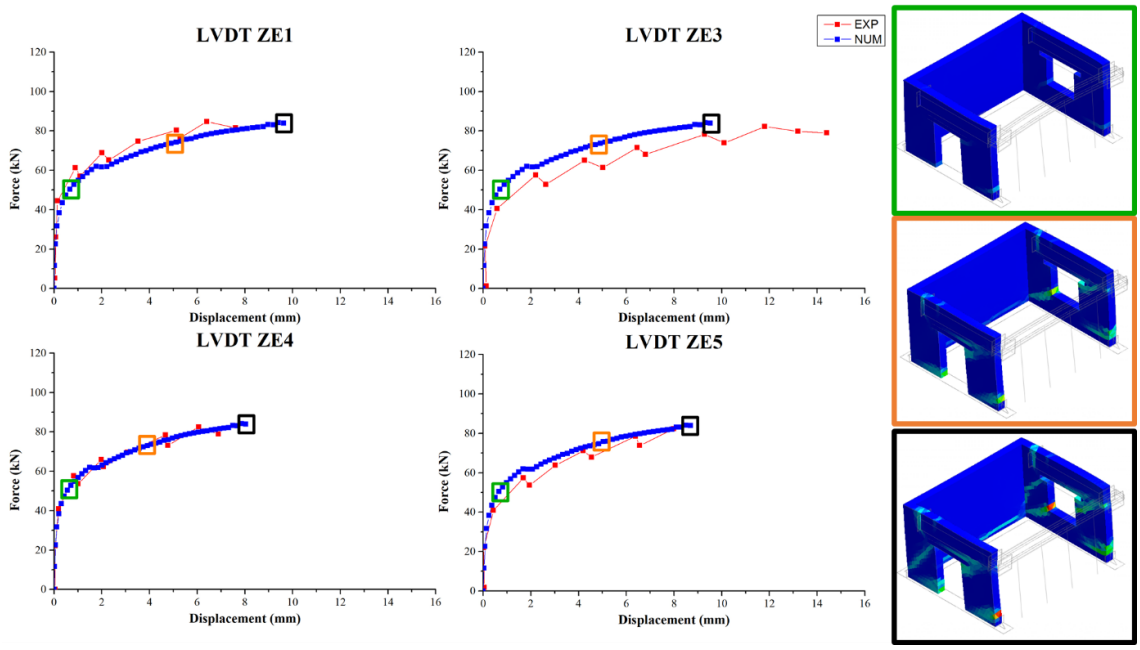

Figure 4.23. Comparison of experimental and numerical curves with updated nonlinear parameters considering the TRM-reinforced structure.

4.7 Conclusion

In conclusion, this chapter groups together the experimental and numerical test results, carried out on a reinforced and non-reinforced structure, performed to evaluate the potential benefits of using TRM to improve the seismic response of masonry structures.

From the data obtained the following main conclusions emerged:

- The TRM can increase the resistance of the structure without excessively affecting its stiffness
- The improvement made by the TRM is visible both by comparing the force-displacement curves and by observing the crack pattern between the reinforced and non-reinforced structure
- The ambient monitoring has confirmed that the TRM, together with the restoration of the cracks, is able to completely reestablish the original load-bearing capacity of the structure.
- Comparing the frequencies of the structure in its different configurations, the low-frequency values are the most affected by the damage
- The mechanical properties were based on fitting the structural response within the numerical values and experimental results. This process confirmed that a good correlation could be found by simply reducing the mortar's tensile strength until the structure reached a notable failure. This can be explained by the reduced tensile strength of the mortar-brick interface concerning the tensile strength of the mortar itself.
- Once the structure reached a considerable level of damage, the only way to reproduce the experimental behavior in the numerical modeling was by unrealistically reducing some parameters, showing the possible limitations of the modeling technique adopted and the good correlation with reasonable mechanical property values until notable failure mechanisms were found.
- The repair and application of TRM strengthening were able to completely restore the initial structural capacities, which in fact was even able to increase its resistance to horizontal loading

However, from the observation of the pseudo-dynamic and environmental test results, several problems were identified that prevented the identification of a damage index:

- To estimate damage there weren't enough measuring points to have enough spatial resolution of the mode shapes.
- It would have been appropriate to monitor the structure at the end of each cycle to follow the variation of the dynamic parameters as the damage increased
- The structure is lightly loaded, this can be seen in the sliding phenomena at the base

Therefore, due to these problems and due to the presence of too many variables, it was decided to calibrate the damage index on a simpler model: an arch subjected to incremental displacement cycles applied to 1/3 of the span.

Chapter 5: Experimental tests and numerical models of masonry arches unreinforced and reinforced with TRM

5.1 Introduction

In this chapter, the study of a new damage quantification index is presented. The study was carried out on experimental data of masonry arched unreinforced and reinforced with TRM. The arched was tested under pseudo-static test apply incremental displacements on 1/3 of the span, during all the test duration the structure was monitored with nine LVDT, meanwhile after each step of the test dynamic monitoring was performed. The index was obtained crossing both the information. The index was at the end validate on a numerical model. [115]

5.2 Construction of the arches

The six masonry arches were realized in the Structural Laboratory of the University of Minho (Guimarães, Portugal). They were built to study the structural capacity of typical adobe bottle vaults located in the historical construction of Yard, a central city in Iran. The main object of the laboratory study was to obtain the structural capacity of vaults and to figure out if the use of Textile Reinforced Matrix was a good technique to improve their residence both in the pre-damage that in post-damage condition. The large number of sensors used during in this test have permitted to use it also to carry out the study of a new damage index to estimate faster and easily the actual residual capacity of vaults.

The dimensions of the tested arches were chosen with reference to the 'Talar' rooms because their geometry is visible, since they look out directly on external courtyards. After careful historical research it was found that the most typical configuration is that reported in Figure 5.1 composed of five vaults of which one is large central. Once the typology was identified, the average dimensions were recognized.

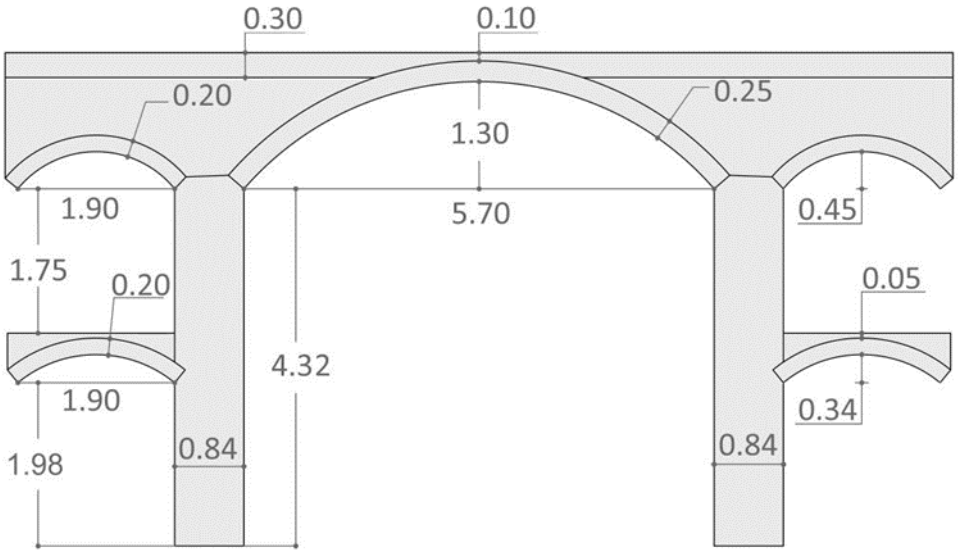

Figure 5.1 Main dimensions of vaults on 'Talar' rooms[116]

Amongst these five vaults, the bigger one was chosen to be analysed. To be easier to realized and tested in the laboratory, the dimensions of the samples were scaled of 1/3 and, since a barrel vault is nothing more than a succession of arches, a depth of 1 m was considered. The final arches' dimensions are shown in Figure 5.2.

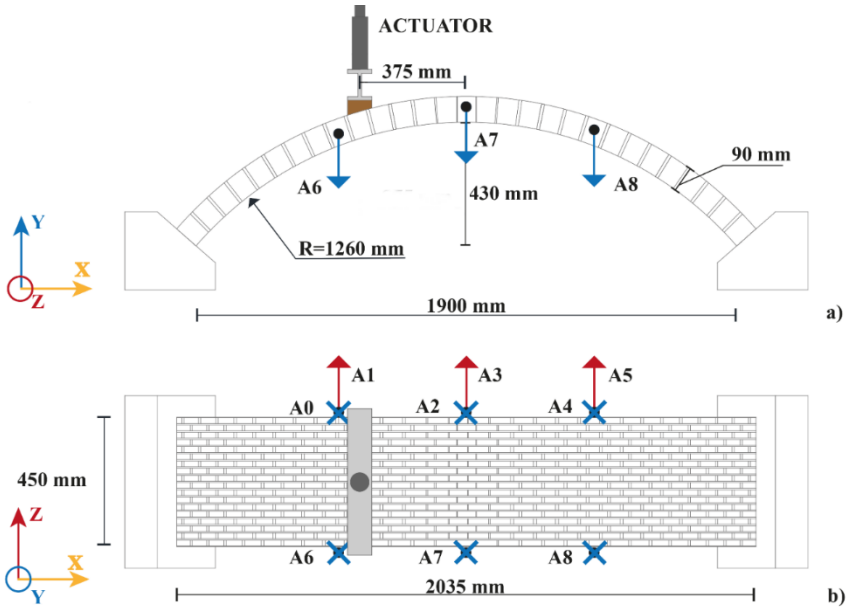

Figure 5.2 Geometric dimensions of the adobe arches and test layout with sensors location: a) Front view; b) Top view

To be accurate, also the masonry bricks were realized in the UniMinho's laboratory in the same scale with dimensions 90 x 65 x 20 mm^3 (height x width x thickness). The construction took place using wooden outlines on which the bricks were laid vertically

with earthen mortar following a running bond pattern, keeping the joints' thickness less than 6 mm. The arches rested on concrete bases fixed to the floor of the laboratory. The filling was not carried out due to the difficulty of installation, its contribution was considered by placing two cement bags at the top, for a total of 25kg.

Six arches were built, four were reinforced with a glass Textile Reinforced Mortar (TRM) covered with earth-based mortar, aiming at testing the effectiveness of this relatively recent affordable strengthening solution to improve the overall structural capacity of adobe arches. Specifically, two arches were strengthened with the TRM at the intrados and two other arches were reinforced with this same material at the extrados. In the intrados TRM application, four spike connectors were added to prevent the early detachment. After the pseudo-static tests, the unreinforced adobe arches were repaired by repointing the cracked joints with earth-based mortar and strengthened with TRM at the intrados, aiming at evaluating the effectiveness of the methods to recover the previously damaged elements. In Table 5.1 are report the acronyms used later in the text to identify the different samples.

Table 5.1 List of tests performed on the six adobe arches with their relative acronyms. [39]

Arch Type	Test Acronym	No. Cycles
Unreinforced	UN (1-2)	8
Strengthened at the Extrados	SE (1-2)	12 (SE1), 14(SE2)
Strengthened at the Intrados	SI (1-2)	10
Repaired and Strengthened at the Intrados	RSI (1-2)	10

5.3 Tests set up

The arches were subjected to loading-unloading cycles until collapse, except for the UN arches' tests, which were stopped before repair and strengthening becoming unfeasible, allowing conducting two further destructive tests; thus, a total of eight pseudo-static tests were performed. The number of cycles applied to each arch is reported in Table 5.1, where it is possible to observe a slightly different behaviour for SE1 and SE2 arches, related to a distinct collapse: the former due to delamination, the latter due to rupture of the fibre-glass. The pseudo-static tests were carried out by applying controlled displacements, by stages of increasing amplitude, at the arch third span through a hydraulic jack. To prevent a concentrated application point, the displacement-imposition system consisted of a steel beam connected to a wooden beam shaped according to the arch curvature. The displacements were applied in progressive stages in order to reach different Damage

Scenarios (DSs). Table 5.2 shows the displacement rate imposed at each cycle together with the loading and unloading velocities used during the tests for each damage scenario.

Table 5.2 Summary of displacement rates and velocities adopted for the pseudo-static tests. [55]

Cycle	Maximum displacement [mm]	Loading speed [μm/s]	Unloading speed [μm/s]
DS 1	0.48	10	10
DS 2	0.62	10	10
DS 3	0.80	10	10
DS 4	1.18	10	10
DS 5	4	10	30
DS 6	6	10	30
DS 7	8	10	50
DS 8	10	10	50
DS 9	14	10	50
DS 10	18	15	50
DS 11	22	15	50
DS 12	26	15	50
DS 13	34	15	50
DS 14	42	15	50

5.4 Testing campaign and results

5.4.1 Pseudo-static tests

A series of pseudo-static loading-unloading cycles were progressively applied to induce damage in the arches. During the tests, the reaction forces corresponding to the imposed displacements were recorded using the 10kN load cell of the actuator. Moreover, eight Linear Variable Displacement Transducers (LVDTs) were deployed to measure each arch's displacements at relevant locations. A detailed description of these instrumentation of the arches is available in [55] and [116]. The force-displacement curves presented and discussed hereafter refer to the data monitored at third-span by the LVDT and load cell operating simultaneously on the hydraulic jack.

Before starting with the tests, the arches were pre-stressed by placing two cement bags of 25 kg each at midspan. The loading-unloading cycles were applied consecutively until the collapse condition was reached, except for the unreinforced arches UN 1 and UN 2, whose tests were stopped once a 20% decrease of the maximum force was recorded, thereby limiting the visible induced damage and facilitating their repair by means of TRM at the intrados.

The outcome of the pseudo-static tests conducted on each arch is plotted in Figure 2 in terms of force-displacement capacity curves. For comparison purposes with the UN arches, two quantities are computed for each group, namely the average maximum force and the average ductility, where the latter is calculated as the ratio between the displacement recorded in correspondence of the maximum force and the displacement measured upon reaching in the following cycles 80% reduction of the maximum force [117]. Observing the curves, the application of TRM at the extrados of the undamaged adobe arches appears to be the best technique to increase both the ductility and structural resistance. In fact, an increase of about 395% (29.98 SE vs. 6.05 UN) and 130% (2.67 kN SE vs. 1.16 kN UN) is observed in terms of ductility and maximum force, respectively, as compared to the UN specimens. On the other hand, the application of the TRM reinforcement at the intrados of the arches leads to a decrease of ductility equal to 49% (3.63 SI vs. 6.05 UN), but proves to be effective to increase the load capacity of about 118% (2.53 kN SI vs. 1.16 kN UN). In what concerns the arches previously damaged and then reinforced with TRM at the intrados, their capacity curves show the smallest increase in terms of resistance, around 27% as compared to its unreinforced configuration (1.48kN RSI vs. 1.16 kN UN), and a 90% decrease in ductility (0.59 RSI vs. 6.05 UN). The different increment of resistance between SI and RSI arches is due to the lack of perfect continuity of the material after cracking appears. For a thorough analysis of the strengthening capabilities provided by the TRM reinforcement, the reader is referred to [55,116,118]. As far as this work is concerned, only the results reported above are of interest for the comprehension of the damage index presented next.

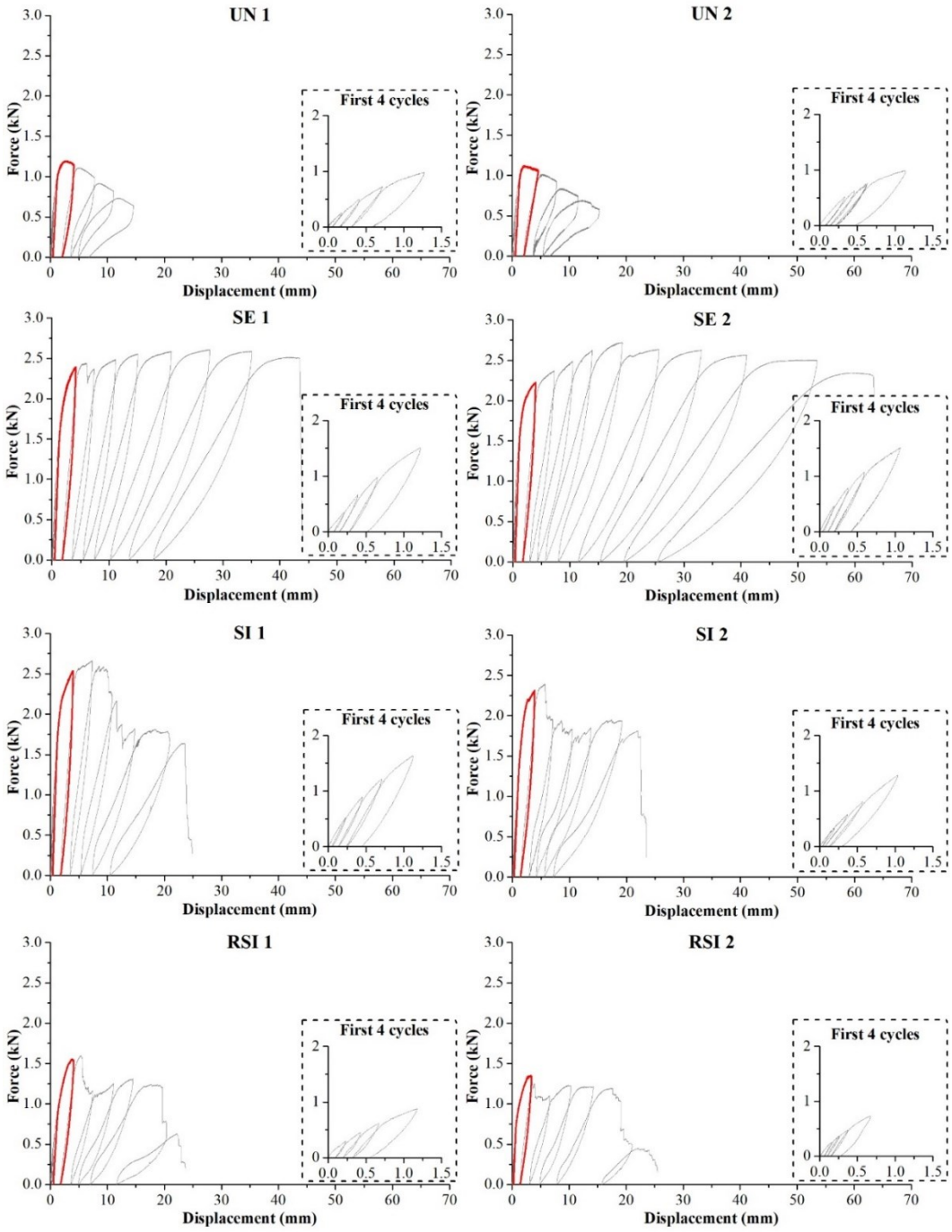

Figure 5.3 Force-displacement curves obtained from the pseudo-static tests per each arch analysed (in red the fifth cycle that corresponds to the first visible cracks). A close-up of the first four cycles is provided on the right.

For all the tested samples, regardless of the presence of the strengthening, the first cracks became visible during damage scenario DS 5 (Figure 5.3, red lines) for an imposed displacement of 4 mm, even though the maximum force attained in this cycle did not always correspond to the maximum resistance of the arch. Nevertheless, the force-

displacement curves show a clear non-linear behaviour since the first cycles (Figure 5.3), meaning that micro-cracks still not visible to the naked eye had already developed. The crack pattern after DS 5 varied in each arch according to the presence and position of the TRM (Figure 5.4). In the unreinforced arches UN 1 and UN 2, four and three cracks appeared (Figure 5.4a-b), respectively, proving their very low resistance against imposed vertical displacements. As for the strengthened arches SE (1-2) and SI (1-2), only a single crack opened after DS 5: at the intrados, in correspondence of the displacement-imposition system, for the arch reinforced at the extrados (Figure 5.4c-d), and at the extrados, symmetrically opposite to the displacement application point, for the arch strengthened at the intrados (Figure 5.4e-f). The variation on the position of the crack hinges depends clearly on to the different reinforcement solutions adopted. Finally, in regard to the repaired and strengthened arches RSI 1 and RSI 2, the first visible cracks after DS 5 varied in number and location, probably because of the inherent difficulties in performing identical repairs in the two samples, but also because of the imperfections typical of manually assembled geometries. Indeed, a slight difference in the number of cracks was already evident in the corresponding unstrengthen models. However, it is noted that none of the RSI arches showed cracks in correspondence of the displacement-imposition system given the presence of the TRM (Figure 5.4g-h).

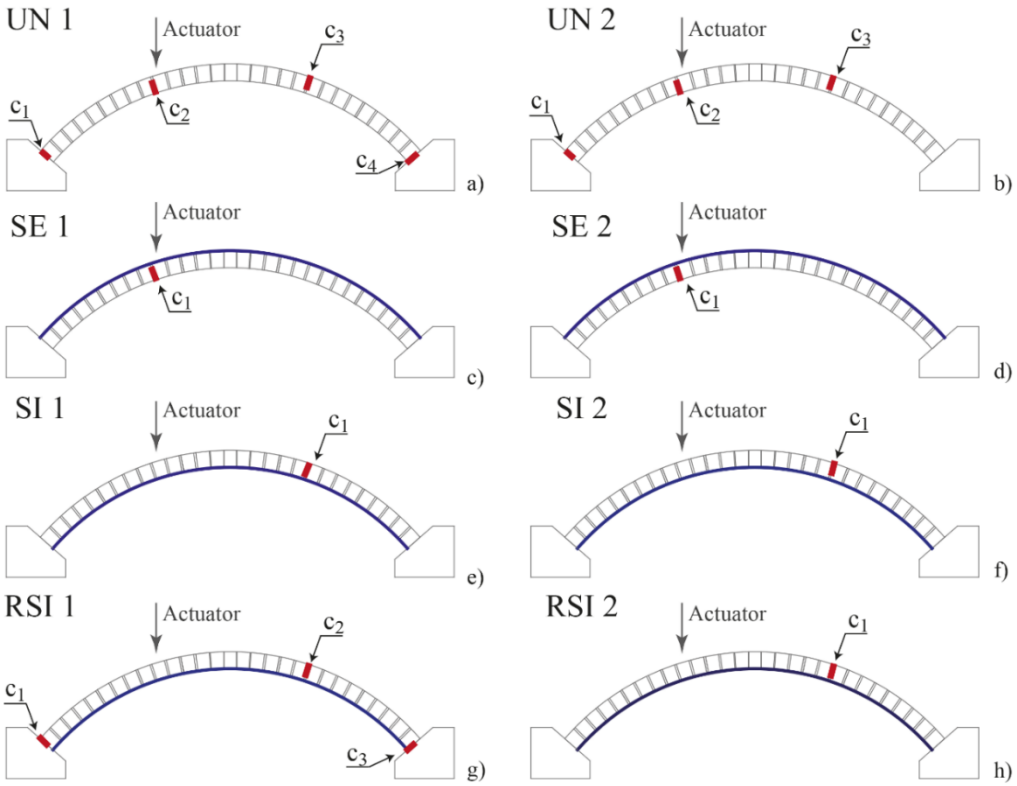

Figure 5.4 First visible cracks for each tested arch (the number to identify the cracks does not correspond to their sequence of occurrence):a) Unreinforced; b) Reinforced at the extrados; c) Reinforced at the intrados; d) Repaired and reinforced at the intrados.

As the displacements increased, all adobe arches, except for UN 1 and UN 2 (four hinges), developed three hinges collapse mechanism. In particular, the reinforced arches collapsed following the detachment of the TRM strengthening (Figure 5.5).

Figure 5.5 Collapse due to the TRM detachment: a) arch strengthened at the extrados (SE1); b) Arch strengthened at the intrados (SI1); c) Repaired arch strengthened at the intrados in the damage scenario before the collapse (RSI1). [116]

5.4.2 Dynamic identification tests

Before starting with the pseudo-static tests and at the end of each displacement cycle, dynamic identification tests were carried out with the aim of following the evolution of the modal response of the arches and recording any possible change in their dynamic properties as the damage developed. Nine uniaxial piezoelectric accelerometers (model PCB 393B12), with a sensitivity of 10V/g, a dynamic range of ± 0.5 g and a bandwidth

ranging from 0.15 Hz to 1000 Hz, were used to acquire in one setup the time-dependent responses of six measurement points, for a total of nine degrees of freedom (DOFs): six sensors were placed along the back edge of the arch, three in vertical direction (Y) and three in horizontal direction (X), and three sensors were positioned along the front edge of the arch in vertical direction (Figure 5.2). The sensors were distributed where the modal curvature usually assume their maximum values.

The acquisitions were made using ambient noise as a source of excitation, being this the most common technique employed nowadays for the dynamic characterization of in-situ and laboratory structures, given the relatively low cost of the equipment and the possibility to perform the tests during the actual operational conditions of the structure. As for the present case, the ambient vibration tests were performed in laboratory environment, thus with controlled background noise and constant temperature-humidity conditions. The response signals were acquired with a sampling frequency of 400 Hz through a multichannel data acquisition system provided with a 24-bit ADC and anti-aliasing filters and connected by cables to the accelerometers. Each acquisition lasted 20 minutes, providing acceleration time-series longer than 2000 times the period of each arch's fundamental mode.

The recorded signals were then processed and analysed using the ARTeMIS software [119] by means of a time-domain output-only modal identification technique: the Stochastic Subspace Identification with Unweighted Principal Component (SSI-UPC) [86]. For all the analysed arches, three vibration modes in the frequency range 20-40 Hz were unequivocally identified in the undamaged condition: one dominant out-of-plane bending mode (Z direction) and two vertical bending modes (Y direction), of which one asymmetrical and one nearly-symmetrical (Figure 5.6).

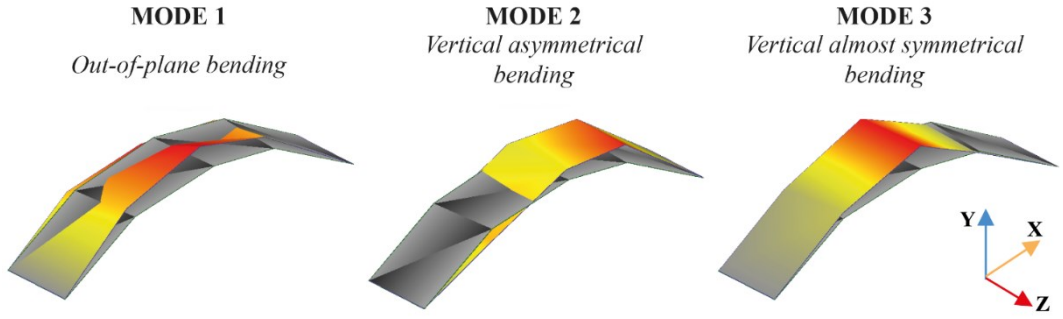

Figure 5.6 First three typical mode shapes of the adobe arches in their undamaged condition (in grey the undeformed shape).

The first three frequencies estimated for the Reference Scenario (RS; undamaged) of each specimen are reported in Table 5.3. By observing their values, it is possible to notice that, despite of the direct relationship between stiffness and frequency, the introduction of the TRM reinforcement has very little or null influence on the first modal frequency, being this frequency associated with an out-of-plane bending mode shape; on the contrary, a beneficial effect is remarked as far as the frequencies of the second and third modes are concerned, when the TRM is applied on the intrados surface of the arch. The highest variations on the frequencies occur to the RSI 2 (repaired and strengthened arch). The SI and RSI arches do not show the same frequencies because, as widely known, it is difficult to reproduce the perfect continuity in cracked structures with this type of intervention, since the performed repair may not be able to close all cracks.

Table 5.3 Frequencies of the first three vibration modes estimated for all adobe arches in their undamaged condition.

	Frequency [Hz]							
	UN 1	**UN 2**	**SE 1**	**SE 2**	**SI 1**	**SI 2**	**RSI 1**	**RSI 2**
MODE 1	23.97	24.27	23.32	23.15	23.58	23.50	24.27	21.97
MODE 2	29.74	28.99	28.98	29.68	31.38	31.42	30.47	31.37
MODE 3	36.49	34.82	34.30	34.35	36.46	37.86	38.82	34.39

The mode shapes identified in the undamaged condition were taken as references for the identification of the first three dominant vibration modes in the subsequent scenarios. The Modal Assurance Criterion (MAC) [86] between compatible modes of the damaged and subsequent undamaged conditions was used as statistical indicator to assess the degree of similarity of the candidate modal vectors. This allows to identify the actual corresponding

vibration modes between different scenarios based on the highest MAC value, according to the well-known formulation Eq. (5.1):

$$MAC(\{\varphi_{RS}\},\{\varphi_{DS}\}) = \frac{\left|\{\varphi_{i,RS}\}^T\{\varphi_{i,DS}\}\right|^2}{(\{\varphi_{i,RS}\}^T\{\varphi_{i,RS}\})(\{\varphi_{i,DS}\}^T\{\varphi_{i,DS}\})} \quad \textbf{(5.1)}$$

where $\varphi_{i,RS}$ and $\varphi_{i,DS}$ indicate the mode shape vectors of the i-th mode of the reference and damaged condition, respectively. This led to obtain a consistent comparison in terms of estimated frequency decay among consecutive damage scenarios. A visual insight into the frequency changes induced by the stiffness degradation of the adobe arches with progressive damage is provided in Figure 5.7.

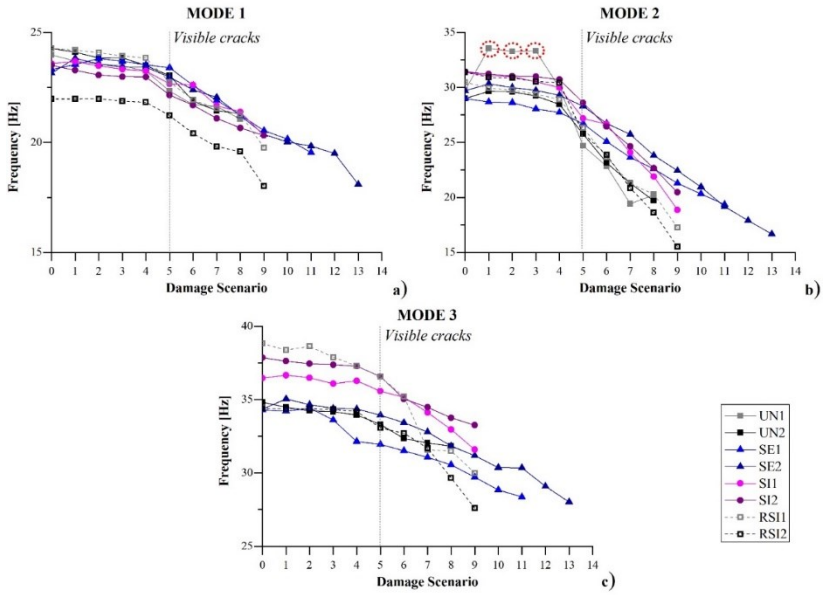

Figure 5.7 Frequencies variation over progressive damage scenarios. Due to the collapse, the frequencies of DS 14 have not been recorded.

As expected, the frequencies of all three identified modes tend to decrease as the damage increases; their average variations, considering all arch types, are: 16% for the 1st and 3rd mode, and 39% for the 2nd mode. Unexpected 11% frequency increments are observed for the 2nd mode of arch UN 1 during the first three DSs, probably due to an initial adjustment of the earthen masonry. For this reason, the three values circled in red in Figure 5.7-b will not be considered in this study. Comparing the frequency drops of all three modes, it is evident how the most significant downshifts are recorded for mode 2, i.e. the asymmetrical vertical bending mode, which is therefore assumed as the most

representative of the damage evolution in all arch typologies (47% decrease for UN 1, 51% for UN 2, 50% for SE 1, 66% for SE 2, 66% for SI 1, 54% for SI 2, 77% for RSI 1 and 102% for RSI 2). In fact, following DS 5, that is the scenario in which the first visible cracks were detected, mode 2 results to be the one suffering the most abrupt variation in the frequency slope (the average reduction with respect to DS 4 is of 8%, against the 3% and 1% of modes 1 and 3). Even though the SI specimens featured higher frequency values for the same mode in the initial scenarios, the arches showing the highest frequencies at the end of the experimental campaign are those with extrados strengthening (SE, light and dark blue lines in Figure 5.7). The 2nd mode of the SI arches (see purple and pink curves) shows a sudden change passing from DS 4 to DS 5, becoming parallel to UN arches (black and grey filled curves). The decrease of the stiffness is directly associated with the sudden damage occurred at the interface with the intrados strengthening due to the high radial stresses, quickly leading to the condition of UN arches. These results are in agreement with the force-displacement curves obtained from the pseudo-static tests (see Section 5.4.1), confirming the efficacy of the TRM strengthening solution when applied to the extrados of arched structures.

5.5 Development of simplified damage indicators

5.5.1 Stiffness loss based on experimental tests

The reduction in frequencies during the experimental campaign was a clear indication of the presence of damage. Indeed, as widely known, if controlled environmental conditions are guaranteed, frequency changes may be associated either to mass or stiffness variations. In what concerns the adobe arches, the observed frequency downshifts are directly related to the loss of stiffness, since no mass variation did occur during the tests. Therefore, starting from the capacity curves discussed in Section 5.4.1, different types of tangent and secant stiffnesses are calculated and compared, in order to find the most appropriate description of the decreasing arch capability and assess the seriousness of the damage. They are the tangent stiffness K_{BS} evaluated according to the BS 1881-121:1983 [120]; the tangent stiffness K_{ASTM} calculated according to the ASTM C469/C469M [121]; the loading secant stiffness K_{load} (slope of the force-displacement curve passing through the points of zero force and maximum force of each cycle); the unloading secant stiffness K_{unload} (slope of the curve passing through the load point corresponding to the maximum displacement of the considered cycle and the point corresponding to the initial

displacement at zero force of the following cycle) [122]; and the secant stiffness K_{sec}, namely the slope of the force-displacement curve passing through the origin (condition of zero force and zero displacement) and the point corresponding to the maximum force in each following cycle. Figure 5.8a illustrates how each slope has been determined.

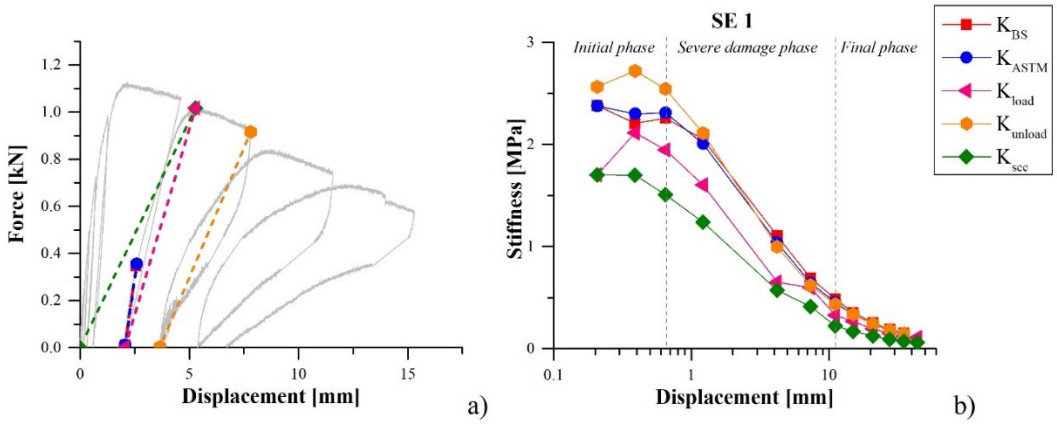

Figure 5.8 Stiffness loss analysis: a) graphical description of the evaluation of each type of stiffness; b) stiffness decrease for SE1 arch during the pseudo-static tests.

As an example, Figure 5.8b shows for arch SE 1 the trend of all considered stiffnesses as a function of the imposed displacements. From this comparison, it is possible to observe that only the tangent stiffnesses K_{BS} and K_{ASTM} provide a consistent description of the damage evolution, since three clear phases can be distinguished: i) stable initial phase, where even if hidden cracks occur these are not soundly affecting the overall arch stiffness; ii) severe damage phase, corresponding to the appearance of visible cracks and a clear stiffness loss; iii) stable final phase, when crack hinges are well formed, the stiffness tends to zero and the arch resists only for static equilibrium. Since the tangent stiffnesses calculated with the two methodologies were very similar, only K_{ASTM} was used for the subsequent evaluations.

5.6 Correlation between stiffness and frequency variation

The following Section presents the formulation of a new damage index for arched systems able to reproduce the progressive stiffness reduction using only the frequency variation.

5.6.1 Formulation of the damage index

In general terms, the stiffness K_d of a damaged structure can be defined as a function of a scalar degradation parameter D_k, which represents the reduction of stiffness with respect

to its initial value K_0, i.e. the stiffness of the undamaged structure as also reported in [123]:

$$K_d=(1-D_k)K_0 \quad (5.2)$$

$$D_k=1-K_d/K_0 \quad (5.3)$$

The damage identification method hereafter applied stems from the observation that the damage scenarios induced during the testing campaign mainly affected the bending behaviour of the arches. As a result, the bending stiffness turns to be the key parameter for the estimation of the damage degree.

Let us consider a geometrically planar beam, i.e. a beam whose undeformed axis is assumed to be a circle lying on the plane of the beam, in order to have a constant, unique curvature. The cross section is assumed constant and with the same orientation with respect to the plane of the beam.

In the curved beam the action of a planar bending produces a variation of curvature, passing from an initial value $k_i=1/R_i$ to a final one $k_f=1/R_f$, satisfying the classical Euler–Bernoulli hypothesis. Considering a generic fibre at distance y with respect to the neutral axis, the strain along the x-beam is:

$$\varepsilon_x=\frac{l_f-l_i}{l_i}=\frac{(R_f+y)d\beta_f-(R_i+y)d\beta_i}{(R_i+y)d\beta_i}=(k_f-k_i)\frac{y}{1+k_iy} \quad (5.4)$$

where $d\beta_i$ and $d\beta_f$ are the angle at the center in the initial and final configurations, and at the neutral axis $R_i d\beta_i = R_f d\beta_f$. The bending moment is equal to:

$$M_z=\int_A \sigma_x y\, dA = E(k_f-k_i)\int_A \frac{y^2}{1+k_iy}dA \quad (5.5)$$

and the constitutive law for a bending curved beam is:

$$(k_f-k_i)=\frac{M_z}{EJ_z} \; where \; J_z=\int_A \frac{y^2}{1+k_iy}dA \quad (5.6)$$

In the case of a beam with weak curvature the term k_iy is negligible; the neutral axis is centroidal and the classical Navier formula is still valid [124]. Therefore, the bending stiffness (K) is comparable to that of a straight beam. In the initial phase, the stress state induced by the bending moment varies linearly along the thickness of the arch, t, reading

the maximum stress values at the top and bottom edges. When the tensile strength of the material is reached, cracks start to occur; assuming damage as a linear perturbation, it can be described as a cross-section loss of the area moment of inertia due to a reduction of the arch thickness (materials and boundary conditions being unvaried). Thus, from the equations above it is deduced that the scalar degradation parameter D_k depends on the thickness variation between the *i-th* damage scenario (t_i) and the reference scenario (t_0), resulting a variation of cubic order:

$$D=1-\left(\frac{t_i}{t_0}\right)^3 \rightarrow D=1-\left(\frac{K_d}{K_0}\right)^3 \qquad (5.7)$$

Considering the relation between stiffness K and natural frequency f of a SDOF system of mass m:

$$K=f^2 m\, 4\,\pi^2 \qquad (5.8)$$

and replacing Eq. (5.8) into Eq. (5.7), the following index D_f has been defined for assessing the structural damage:

$$D_f=1-\left(\frac{f_{j,i}}{f_{j,0}}\right)^6 \qquad (5.9)$$

where $f_{j,i}$ and $f_{j,0}$ are the frequency values corresponding to the *j-th* mode in the considered damaged and undamaged configurations, respectively. It is noted that this is a practical formulation aimed at simplifying the evaluation of the damage degree in masonry arches, and its efficiency is validated through experimental and numerical results.

5.6.2 Stiffness-based vs. frequency-based damage index

With the purpose of assessing the consistency of the formulation illustrated above and its agreement with the experimental results, the frequency-based damage index D_f introduced in Eq. (5.9) is computed for the second experimental mode (vertical asymmetrical bending) in progressive stages for all the adobe arches and compared with the damage parameter D_k of Eq. (5.3), in which the stiffness of the arch for the damaged and undamaged conditions is calculated according to the ASTM standards [121], considering as K_0 the tangent stiffness of the first loading branch of the test and as K_d the tangent stiffness estimated in the loading branch of the cycle following the DS under consideration. The results are shown in Figure 5.9, where the percentage variation of both damage factors (D_k, D_f) is represented over progressive scenarios.

Observing the trend of D_k, which is inversely related to K_d, it is noted that in the initial stages there is an increase in terms of stiffness, likely generated by the material type that tends to adjust [123]. Afterwards, the stiffness gradually decreases up to reaching the first visible cracks, when the slope changes abruptly. In the final phase, corresponding to the last equilibrium condition, the stiffness variation stabilizes, reading the highest damage percentage value. As previously mentioned, this last stability phase is less evident in the unreinforced arches (UN 1-2) because the tests were stopped before collapse in order to repair the models. By comparing the curves of the SE and SI arches, the latter's show a greater slope in the final phase, confirming the less effectiveness of this strengthening solution as compared to the formers. However, it is interesting to note that in almost all cases the first visible cracks occur when the stiffness-based damage factor D_k exceeds the threshold value of 50%, in agreement with what reported by Kubica [125].

By inspecting the trend of D_f, it is evident how the new index is able to consistently follow the stiffness degradation process affecting the arches. The percentage difference between D_f and D_k becomes smaller and smaller as the damage severity increases and cracks become visible, tending to 0% towards the last displacement cycles, with the exception of arch SE 2 and UN 1 that display anomalous values for DS 5 and DSs 1-2-3, respectively. On the contrary, the difference between the two indices is higher before visible damage, especially in the arches where the initial adjustment was more remarkable. It seems that this effect is not caught by the frequencies in the early stages, since they do not increase, except for SE 2.

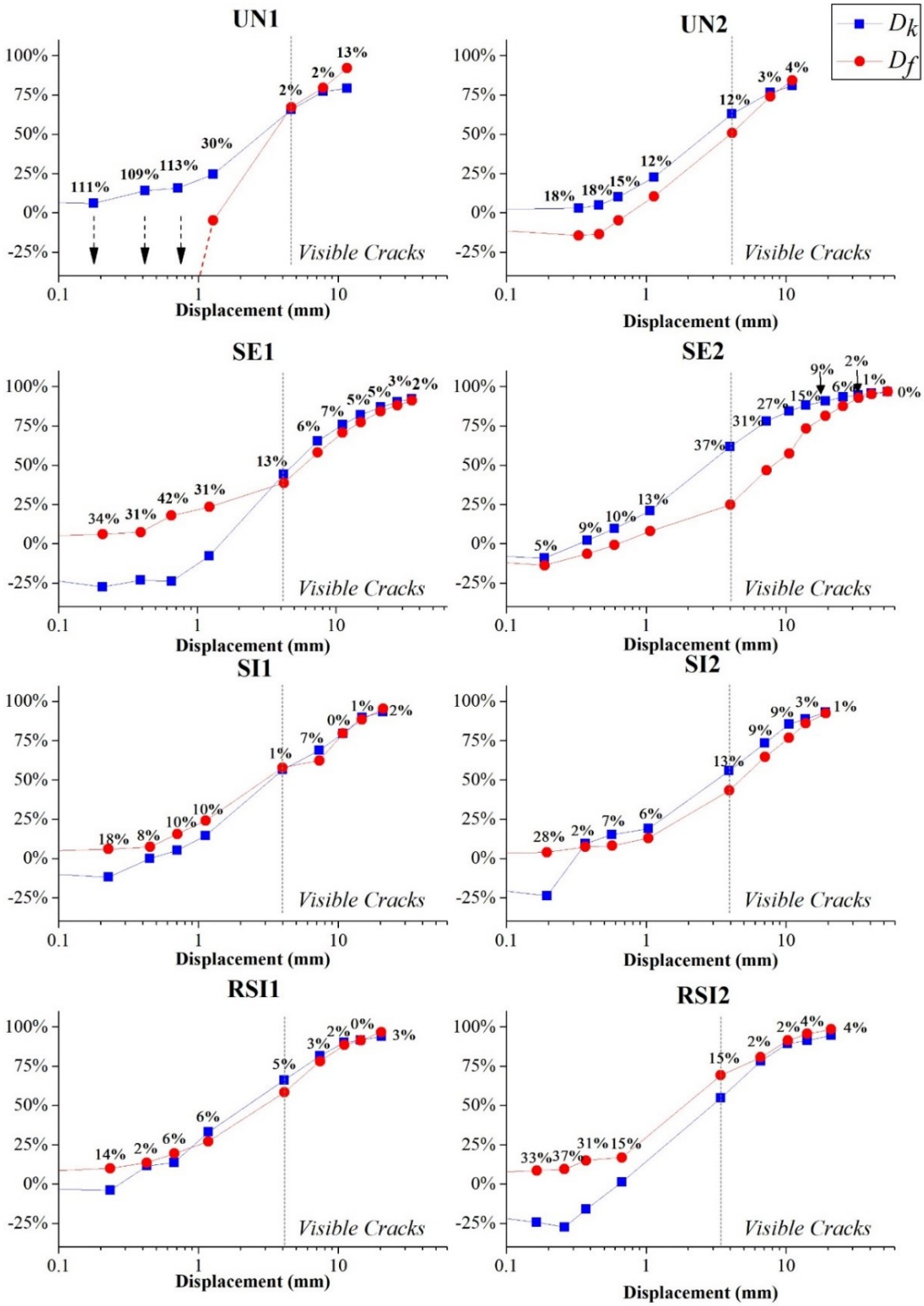

Figure 5.9 Comparison between the stiffness-based damage factor and the frequency-based damage factor for all adobe arches (in black the percentage difference between the two factors).

5.7 Numerical Validation

To verify the replicability and broader applicability of the proposed damage index D_f to other types of arch collapse mechanisms, the experimental validation procedure described in the previous section is here repeated using the numerical results from a similar masonry arch reproduced numerically, while analysing different collapse modes.

DIANA FEA software [126] is employed to build the numerical model of an adobe arch with the same dimensions as those of the tested specimens. The geometric domain is discretized using twenty-node brick elements (CHX60), for a total of 8,480 elements, 42,053 nodes and 124,425 degrees of freedom (Figure 5.10). The 25 kg cement bags used during the experiment to apply pre-compression at the arch key are numerically simulated through added masses. Although the simplicity of the arch geometry could allow for a 2-D analysis, a 3-D model was preferred for this study in order to estimate both in-plane and out-of-plane vibration modes and consider the most significant ones for the damage identification process in terms of frequency reduction. (Figure 5.10)

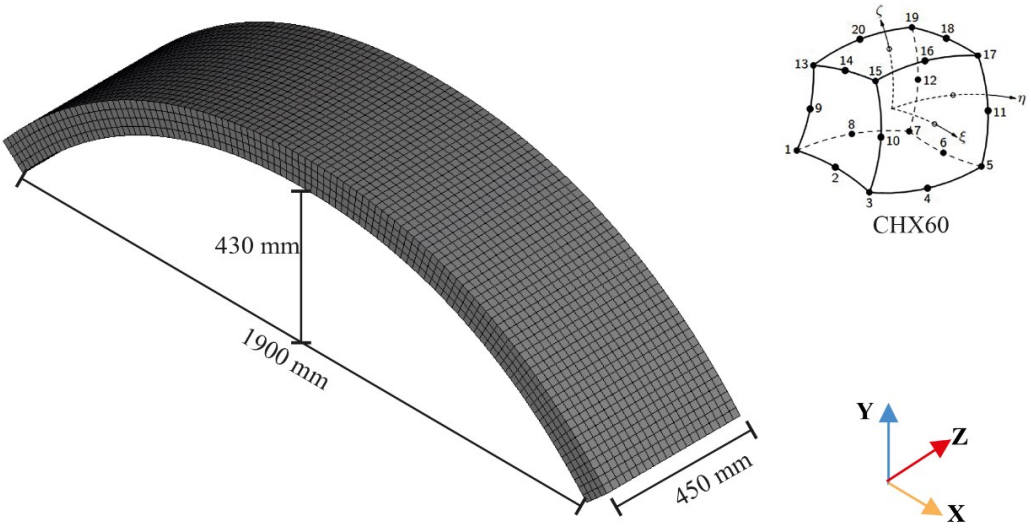

Figure 5.10 Finite element model of the arch.

5.8 Calibration of the numerical model

Aiming at identifying the actual mechanical properties of the materials used for the experimental tests, the first operation performed on the numerical model was its calibration, taking the unreinforced arch in undamaged condition (UN 1) as reference. To this end, a modal-based model updating procedure based on the Douglas and Reid methodology (DR) [127] was carried out on the FE model to match the first three numerical vibration modes with their experimental counterpart. The DR's approach

consists in identifying the values of the uncertain parameters of the model by minimizing an objective function, which is based on the difference between numerical and experimental frequencies.

As starting hypotheses, both the specific weight, whose value was obtained during the experimental campaign [55,116,118], and the Poisson's coefficient were considered as fixed parameters for the updating process with values equal to 1.48 kN/m^3 and 0.2, respectively. As for the adobe material, an orthotropic behaviour was assumed; hypothesis that is in line with what demonstrated in the literature for rammed earth [128,129], i.e. the importance of considering different Young's modules in the three directions if this material is lightly loaded.

From these assumptions, the unknown parameters to calibrate the model are the Young's moduli (E_x, E_y, E_z) and the shear moduli (G_{xy}, G_{yz}, G_{zx}) of the adobe masonry. As indicated in the DR's methodology, reasonable ranges based on literature values [130,131] were defined for the afore-mentioned variables, setting for each of them an initial value X^0, an upper bound X^U and a lower bound X^L (Table 5.4).

Table 5.4 Range of updating parameters set for the numerical model calibration.

	X^0 [MPa]	X^L [MPa]	X^U [MPa]
E_x	1150	1050	1250
E_y	275	250	300
E_z	80	50	110
G_{xy}	300	275	325
G_{yz}	70	50	90
G_{zx}	260	220	300

A step-by-step sensitivity analysis was performed first in order to understand which of the unknown parameters influenced most the modal behaviour of the arch model. Starting from the numerical model with all X^0 values set for the updating variables, subsequent eigenvalue analyses were run changing only one parameter at the time, namely beginning with their maximum and minimum values and then gradually reducing the range around the initial value. Figure 5.11 shows, for each parameter reported in Table 5.4, the percentage errors of the first three frequencies of the numerical model with respect to the experimental values. It is worth noting that the 1st vibration mode, i.e. the out-of-plane bending in Z direction (Figure 5.12), is mainly influenced by the shear stiffness of the

adobe material, especially by the shear modulus G_{yz}, while the 2nd mode, i.e. the asymmetrical vertical bending in Y direction (Figure 5.12), is mainly sensitive to E_x and E_y, as expected given its in-plan deformation, but also to G_{xy}. Finally, the 3rd vibration mode (Figure 5.12) results strongly dependent on E_x and G_{xy} variations.

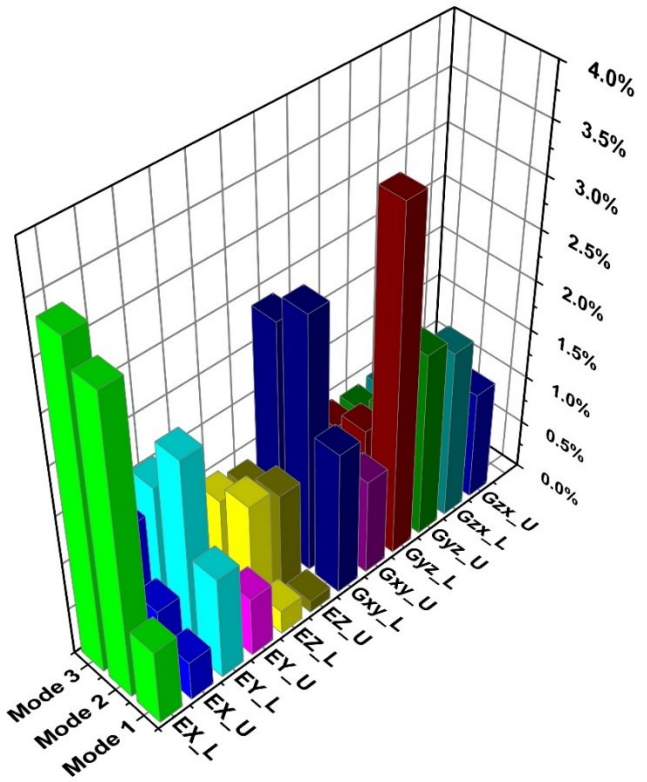

Figure 5.11 Sensitivity of the numerical model to variations in the updating parameters. The influence of each parameters is expressed as percentage difference between numerical and experimental frequencies of the first three modes.

This procedure allowed to progressively tune the numerical model, minimizing the difference with the experimental results up to reaching an average frequency error of 0.36%. The final values of the updating parameters are reported in Table 5.5.

Table 5.5 Updated parameters of the calibrated numerical model.

E_x [MPa]	E_y [MPa]	E_z [MPa]	G_{xy} [MPa]	G_{yz} [MPa]	G_{zx} [MPa]
1155.5	276.2	80.1	308.8	64.3	262.8

In addition to the calibration of the frequencies, the degree of correlation between experimental and numerical modal vectors was also checked using the MAC. The computed values showed a very good correlation between mode shapes, having an

average MAC of 0.99 for the second and third mode, and a minimum MAC value equal to 0.98 for the first mode. Figure 5.12 shows the modal results of the calibrated numerical model in terms of frequencies, mode shapes and MAC values along with the percentage frequency error with respect to the experimental values.

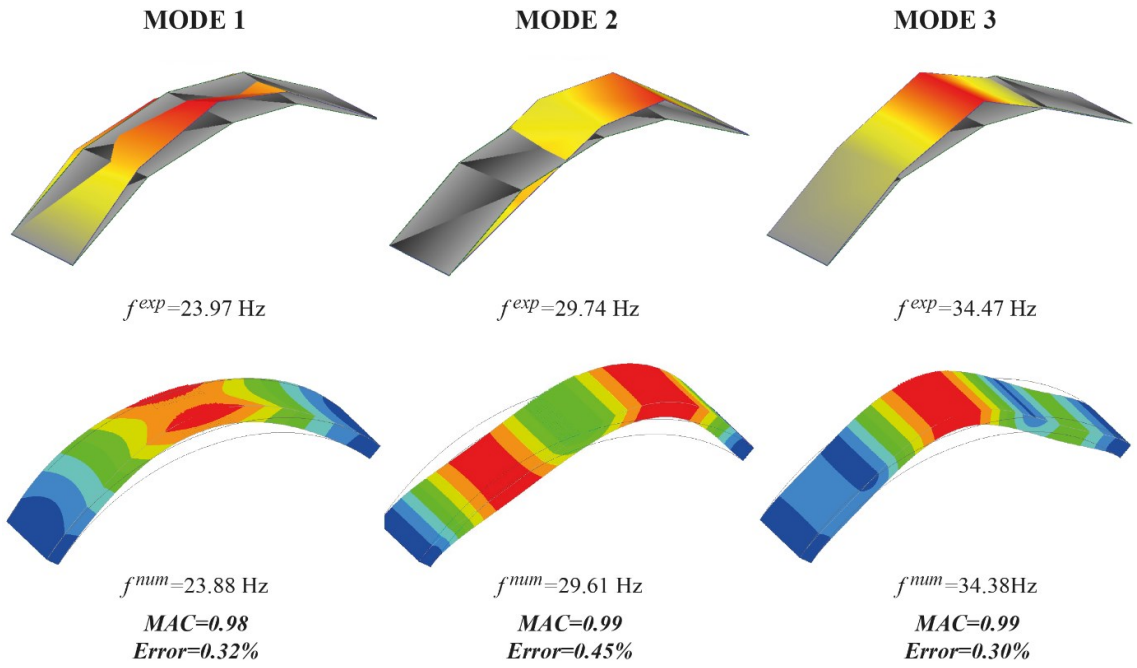

Figure 5.12 Comparison between experimental (top) and numerical (bottom) modes of vibration for the reference arch.

5.9 Nonlinear static analysis

After calibration, different nonlinear static analyses were carried out in order to verify that the experimentally validated damage index was also applicable to other types of collapse mechanisms that may occur in vaults and arches.

In order to represent damage-induced changes in the modal frequencies of the arch model, a nonlinear behaviour was defined for the adobe material. Given the impossibility to adopt the total strain crack model for the orthotropic materials, since it was not yet implemented in the software used, the adobe masonry was modelled as isotropic. First, the cracked value of the E_x ($E_x/2$ = 578 MPa), based on a displacement-based approach for the structural assessment of existing masonry structures (simulation of an arch in an ancient structure) was considered. Then, the Young's modulus obtained from destructive laboratory tests performed on adobe prisms (480 MPa) was also considered [116]. Furthermore, the average value of E_x, E_y and E_z (504 MPa) was calculated. Since all the values are similar, a Young's modulus equal to 578 MPa was adopted. It is noted that this

numerical application represents a theoretical case study adopted only for the evaluation of the damage index. Both mass density and Poisson's coefficient were not changed. For the nonlinear analyses, the weight of the cement bags was modeled as a load applied at the arch extrados. The alterations on the mode shapes and frequencies, with respect to the model with orthotropic behaviour (Figure 5.12), can be observed in the Figure 5.15, which are not relevant for the validation of the damage index.

The nonlinear behaviour of the adobe was described using the Total Strain Rotating Crack model with a parabolic stress-strain curve in compression and a Hordijk stress-strain curve in tension (Figure 5.13), being these the common relationships used when describing the masonry constitutive behaviour [112,132]. In these constitutive laws, it was necessary to define the tensile (f_t) and compressive (f_c) strength as well as their respective fracture energies (G_f, G_c).

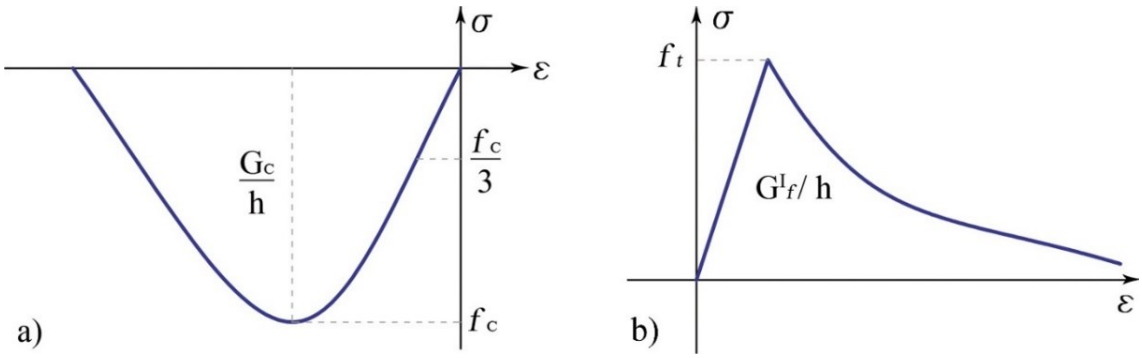

Figure 5.13 Constitutive laws adopted for the adobe material: a) stress-strain curve in compression; b) stress-strain curve in tension

To this end, the value of compressive strength f_c obtained from previous laboratory tests [116] was adopted in the model; while the tensile strength f_t was considered equal to 10% of f_c; as for the fracture energies, the values were defined taking into consideration those reported in previous studies on analogous material [133,134]. Table 5.6 summarizes both the linear and nonlinear parameters adopted for the numerical analysis.

Table 5.6 Material properties adopted in the numerical model for the nonlinear static analyses.

Elastic linear parameters			
ρ [kg/m^3]	1480		
E [MPa]	578		
ν	0.2		
Nonlinear parameters			
Parabolic law		**Hordjik law**	
f_c [MPa]	0.65	f_t [MPa]	0.065
G_c [N/mm]	1.04	G_f [N/mm]	0.02
h [mm]	22.14		

Two nonlinear static analyses were carried out: i) one to simulate a failure condition due to symmetrical horizontal displacement at both supports (out-of-plane deformation of walls or abutments); and ii) one to replicate a collapse mechanism due to a distributed load. For the first condition analysed, opposite horizontal displacements of +/- 1 mm were imposed at the base nodes. In the second case, a uniform distributed load (q) of 1 kN/m^2 was applied on the arch and increased until collapse, causing a five hinges mechanism.

5.10 Discussion of the results

The load-displacement capacity curves of a selected node in the keystone were first assessed (Figure 5.14a-b). Observing the curve representative of the three hinges mechanism induced by the horizontal displacement at the supports, it is noted that the arch presents a brittle behaviour with a sudden collapse after reaching the maximum load capacity. The maximum displacement obtained in the analysis is equal to 6 mm. In what concern the curve representative of the five hinges mechanism, activated by the increased vertical distributed load, a different behaviour is observed, being the collapse reached only for an ultimate vertical displacement of 14 mm after a long stability phase, in which the thrust line still lied inside the arch profile.

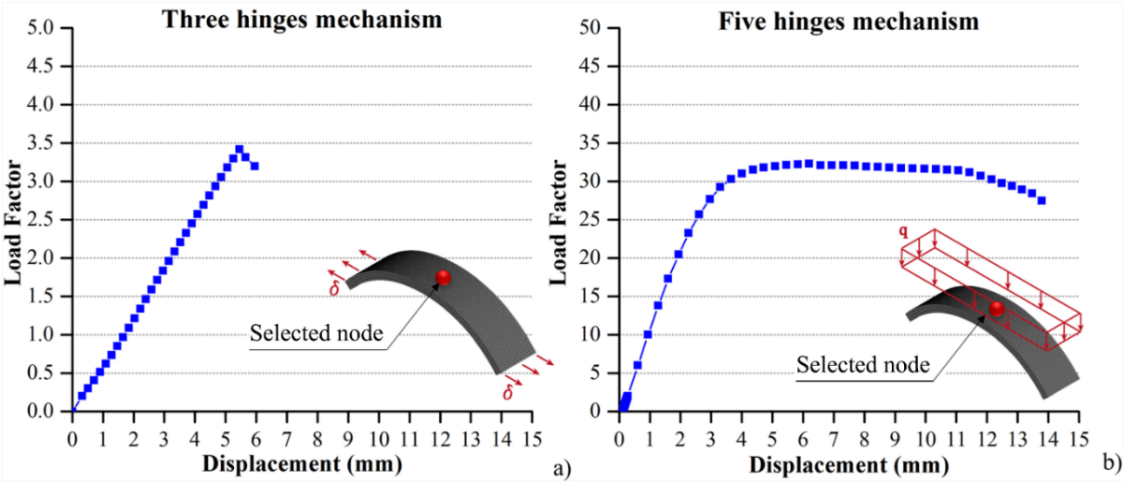

Figure 5.14 Arch capacity curves: a) Three hinges mechanism; b) Five hinges mechanism.

In order to proceed with the numerical validation of the proposed damage index, based on the capacity curves, several load steps (31 for the three hinges mechanism and 39 for the five hinges mechanism) were chosen and the damaged model corresponding to each of these steps was subjected to eigenvalues analysis, considering the tangent stiffness matrix with respect to the previous state. This allowed to estimate the modal properties of the arch over progressive damage conditions. For comparison purposes, only the first three vibration modes were considered: (i) asymmetrical vertical bending; (ii) out-of-plane lateral bending; (iii) symmetrical vertical bending. Frequency values and modal shapes of the arch in its initial state are displayed in Figure 5.15. Although the numerical mode sequence and frequencies in this case did not correspond exactly to the experimental one, this discrepancy was not relevant in the framework of the index validation.

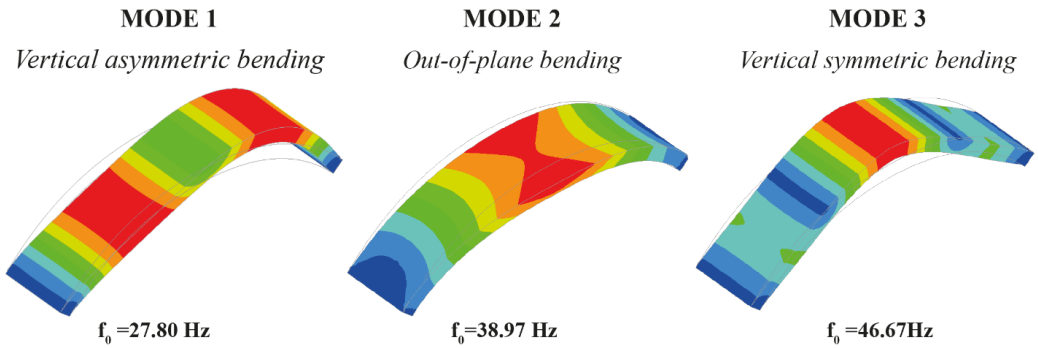

Figure 5.15 Initial modes of the numerical model.

For each analyzed step, the numerical frequencies of the damaged model were estimated and used to compute the damage index D_f according to Eq. (5.9), taking the frequencies shown in Figure 5.15 as reference values for the denominator. Once again, the damage

index seems able to adequately represent the global stiffness degradation of the arch for both types of mechanisms (Figure 5.16).

In the case of horizontal displacements at the supports, the most affected mode by the stiffness loss is the first one (Figure 5.16a, black line), which corresponds to the asymmetrical vertical bending, presenting a damage index already higher than 50% for a vertical displacement of 1.47 mm (load factor 0.85) in contrast with the second and third modes that reached this value for 1.84 mm and 1.66 mm (load factors 1.09 and 0.97), respectively. The first cracks occur at the extrados of both supports, for a vertical displacement of 0.5 mm (load factor 0.3) and D_f = 6%, and then they increase simultaneously with the formation of the crack at intrados (first intrados slits occur for a load factor of 0.73 and D_f = 45%). From Figure 5.16.a, it is observed that no concentration of stresses occurs at the intrados. The stresses are distributed over an extended area, hence the remarkable high value of the damage index for all three modes.

On the other hand, the collapse due to vertical distributed load is more complex. In the initial stages, modes 1 and 3, i.e. the asymmetrical and symmetrical vertical bending modes, respectively, are those showing a greater stiffness decrease, thus higher values of D_f; then, as damage becomes more severe and high stresses are simultaneously reached at all crack hinges (D_f = 50%), the damage index records an abrupt increase, especially as far as the second mode is concerned, reaching a D_f = 90% at the collapse limit (Figure 5.16.b). The first cracks occur at the intrados of the supports for a vertical displacement of 2.96 mm (load factor of 27.68) (D_f = 16% for the first mode, D_f = 3% for the second mode and D_f = 9% for the third mode); subsequently, these cracks continue to increase and a third hinge appears at the intrados of the keystone (D_f = 29% for the first mode, D_f = 16% for second the mode and D_f = 27% for the third mode). Finally, for a vertical displacement of 11.07 mm (load factor of 31.42), two symmetric cracks begin to form at the extrados of the arch haunches (D_f = 58% for the first mode, D_f = 60% for the second and third mode). From this stage on, the stiffness loss due to the five cracks mainly affects the symmetrical modal response of the arch, both out-of-plane (mode 2) and in-plane (mode 3). In any case, the damage index based on the first mode is also a good indicator to evaluate loss stiffness of the arch, mainly for the initial damage, including for the damage index equal to 50%.

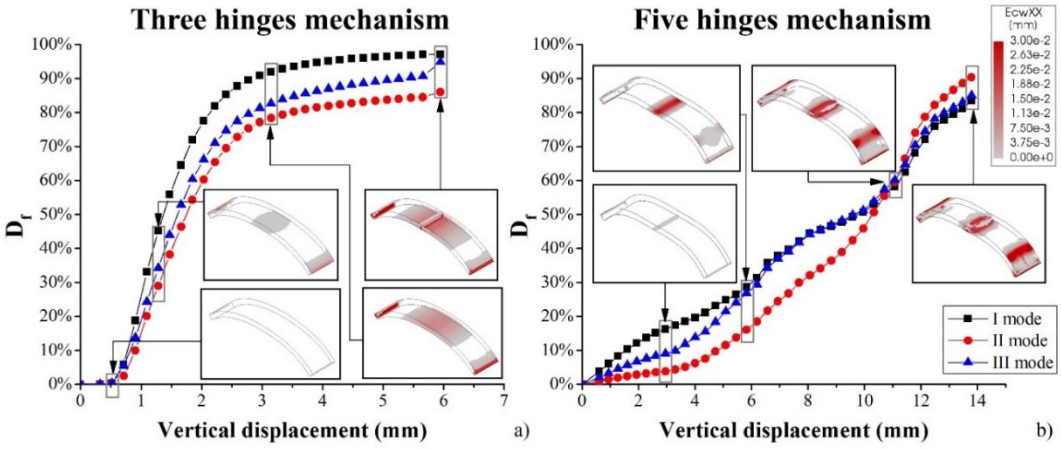

Figure 5.16 Damage index evolution with progressive cracking: a) three hinges mechanism; b) five hinges mechanism.

5.11 Conclusions

The main objective of this work was to elaborate an index capable of following and assessing the structural damage in arched systems using a supervised approach, i.e. with respect to a reference condition, considering that these structures are mainly damaged by bending moments. The aim was driven by the necessity to find a simple yet effective damage index, applicable in the engineering practice to keep these structural systems under control during their entire life cycle (monitoring) and assess the real need of intervention when an anomalous stiffness reduction is observed, before severe damage occurs. Since the dynamic parameters of structures are sensitive to damage, the frequencies were chosen as key modal indicators for the definition of the index, considering also that these parameters are easily identifiable even with a reduced number of sensors.

To achieve this goal experimental and numerical data were used. The experimental data were obtained by pseudo-static laboratory tests executed on six adobe arches, either unstrengthen or strengthened with TRM. The arches were subjected to increasing cycles of vertical displacement at third span to induce different damage scenarios; at the end of each cycle, a dynamic identification test was performed for the progressive evaluation of modal parameters. The estimated frequencies were used to elaborate and verify the reliability of a new damage index D_f, expressed as a function of the frequency ratio between damaged and undamaged scenarios. The direct comparison with a stiffness-based degradation index D_k, calculated as a function of the reduction of the tangent

stiffness along the tests, demonstrated that in most cases the D_f index is able to satisfactorily follow the stiffness loss of the arches due to progressive damage.

To evaluate the applicability of the proposed index also for other types of collapse mechanisms of arched structures, a numerical work was carried out. Two common arch failures were simulated following the same procedure of the experimental tests. The loading cycles were reproduced by non-linear static analyses and the varying frequencies were obtained at each cycle from an eigenvalue analysis, carried out considering the residual tangent stiffness after each non-linear analysis. The results of the numerical models validated the capability of the index to follow the stiffness degradation and strength reduction of the adobe arches.

In conclusion, it is shown that the proposed frequency-based index is able to identify and quantify the structural damage in all analyzed arched systems, both experimentally and numerically, using just a few sensors, provided that they are sufficient in number to capture the first and most meaningful vibration modes for the considered/expected damage scenario. In fact, for the present case studies, the sole identification of the vertical asymmetric bending mode – which turned out to be the most susceptible to the induced damage – could be enough for damage identification purposes.

Chapter 6: Conclusion

There are many masonry structures around the world since this has always been one of the main construction techniques. The features that made this a frequently used construction technique are: appearance, strength, durability, thermal and acoustic comfort, and fire resistance. Although they may appear to be massive structures, some of their features make them prone to severe damage when subjected to horizontal loads, such as those generated by earthquakes. Its wide use over the centuries has meant that a large part of the world's historical heritage was built with it, which makes these buildings very vulnerable in the event of an earthquake. These structures often present absent or scarce interlocking between floors and walls, openings too close to the corners of the buildings, or excessively slender elements, factors that make the structures subdivide into an assemblage of macro-elements that respond differently to the horizontal actions.

Given the need to preserve these structures, to be able to pass them on to future generations, it is essential to find intervention techniques capable of improving their capacity, without affecting their artistic value, and to elaborate easy and fast methods able to analyses in real or nearly-real time the structural capacity, to intervene promptly in case of damage onset, thereby avoiding expensive belated restoration works.

Over the years, many restoration techniques have been used to improve the buildings' response both at the local and global levels. The most frequently used of these are: metal chains, concrete or steel curbs, reinforced concrete plaster, and Fiber Reinforced Polymer composites (FRP). In recent years, a new composite has been introduced, the TRM, to overcome the problems related to the use of FRP on masonry structures. Two features differentiate TRM materials from FRP: (i) the matrix, which is cementitious rather than polymeric and can work better in a masonry structure, and (ii) the arrangement of fiber bundles in the form of textiles to improve adhesion to the matrix. This strengthening material has further advantages compared to FRP, such as being completely reversible, heat resistant or permeable, and applicable to damp surfaces.

As part of the following doctoral thesis, a cognitive survey of the capabilities of the TRM was carried out, passing from experimental tests to numerical analyses. Starting from qualification tests on a TRM with PBO fibers and creating the respective numerical models, it was observed that when both mortar and matrix are subjected to the same stresses, no relative sliding occurs within the composite. On the contrary, it was essential

to consider this phenomenon to reproduce the debonding test in numerical modeling, a test in which the fiber tends to slip inside the matrix. Still using these qualifying tests, a sensitivity analysis was carried out, aimed at evaluating whether there were variations in the results as the degree of detail of the modeling varied. The results showed that accurate modeling (fiber modeled with 3D elements following the real geometry) returns a more truthful distribution of the tensions at the microscopic level, on the contrary, more approximate modeling (fiber with 2D elements and matrix with 3D elements), also if it fails to grasp these perfectly, it able to reproduce the overall response of the composite equally. For this reason, the latter modeling was considered the most appropriate when it is necessary to shape it on a structure since it requires less time both in the modeling and in the calculation phases.

The evaluation of the effectiveness of the TRM in improving the structural response of masonry structures was performed using two experimental tests carried out respectively by the University of Valencia and the University of Minho:

- The test carried out at the University of Valencia, in the ICITECH laboratory, concerned a U-shape masonry structure subjected to pseudo-dynamic horizontal displacements. The prototype was tested in two different stages: (i) on the as-built structure and (ii) after the repair and the application of TRM.
- The test carried out at the University of Minho, in the ISISE laboratory, concerned six arches damaged up to collapse using pseudo-static test cycles carried out by applying progressive vertical displacements. Four out of six arches were reinforced with TRM. Specifically, two arches were strengthened at the intrados and two other arches were reinforced at the extrados After the pseudo-static tests, also the unreinforced adobe arches were repaired and strengthened with TRM at the intrados.

From the analysis of the experimental and numerical data of the U-shaped structure, it emerged that the TRM, together with the closure of the cracks, can restore load-bearing capacity and increase the structural capacity to horizontal actions, both in the push and in the pull direction. The application of the TRM also allowed a more monolithic response of the structure.

The same improvement was also observed for the adobe arches. In fact, the use of the composite on the arches, both intact and pre-damaged, has made it possible to increase

their structural capacity. However, this increase is more evident in intact arches, since it is very difficult to reconstruct perfect continuity in damaged structures. From these tests it was shown that the TRM is more effective if applied to the extrados of the arches, allowing in this case also an increase in ductility, since as illustrated in literature, compressive stresses are triggered which improve the friction between matrix and substrate.

In addition to analyzing the effectiveness of TRM in improving the capabilities of masonry structures, this thesis had another objective, that of finding an index that would allow the identification and quantification of damage in masonry structures. To identify it, the pseudo-static tests, the Operational Modal Analysis tests, and numerical models of the two different experiments were used.

The U-Shape structure turned out not to be suitable for calibrating a damage index because the dynamic information was not sufficient, both as regards the frequencies and the modal shapes and because this experiment included a large number of variables difficult to control and to reproduce on numerical models.

On the contrary, the tests on arches, being more controllable, having a high number of sensors, and having been monitored at the end of each cycle, proved to be optimal for the purpose. From the analysis of the modal shapes and the observations of the frequency variations of the first three modes as the damage increases, it emerged that the modes most affected by the damage were the asymmetrical vertical bending. For this reason, starting from the bending stiffness, a damage index was developed as a function of the frequency ratio between damaged and undamaged scenarios starting from the hypothesis that the environmental conditions had constant and that no mass variation had occurred. The index found was first validated with experimental tests, comparing it with the stiffness degradation index, and subsequently tested on other types of collapse, that can occur on the arches, using Finite element models. The results of the numerical models showed that also for the other types of collapse the asymmetric vertical flexural mode is the most suitable for identifying the presence of damage.

In the future, it will be possible to verify the index reliability by testing it on arches made of other materials.

Another possible future development could be the reconstruction of the U-Shape structure, trying to correct the problems that emerged, to test the possibility of applying this index and/or creating a new one.

References

[1] M. Valente, G. Milani, Seismic assessment of historical masonry towers by means of simplified approaches and standard FEM, Constr. Build. Mater. 108 (2016) 74–104. doi:10.1016/j.conbuildmat.2016.01.025.

[2] M. Acito, C. Chesi, G. Milani, S. Torri, Collapse analysis of the Clock and Fortified towers of Finale Emilia, Italy, after the 2012 Emilia Romagna seismic sequence: Lesson learned and reconstruction hypotheses, Constr. Build. Mater. 115 (2016) 193–213. doi:10.1016/j.conbuildmat.2016.03.220.

[3] S.W.S. Doebling, C.R.C. Farrar, M.B.M. Prime, D.W.D. Shevitz, Damage identification and health monitoring of structural and mechanical systems from changes in their vibration characteristics: a literature review, Los Alamos Natl. Lab. (1996). doi:10.2172/249299.

[4] A. Alvandi, C. Cremona, Assessment of vibration-based damage identification techniques, J. Sound Vib. (2006). doi:10.1016/j.jsv.2005.07.036.

[5] Y.J. Yan, L. Cheng, Z.Y. Wu, L.H. Yam, Development in vibration-based structural damage detection technique, Mech. Syst. Signal Process. 21 (2007) 2198–2211. doi:10.1016/j.ymssp.2006.10.002.

[6] S. Das, P. Saha, S.K. Patro, Vibration-based damage detection techniques used for health monitoring of structures: a review, J. Civ. Struct. Heal. Monit. 6 (2016) 477–507. doi:10.1007/s13349-016-0168-5.

[7] J.J. Sinou, A review of damage detection and health monitoring of mechanical systems from changes in the measurement of linear and non-linear vibrations, Mech. Vib. Meas. Eff. Control. (2009) 643–702.

[8] A. Rytter, Vibrational Based Inspection of Civil Engineering Structures, University of Aalborg, 1993.

[9] C. Gentile, A. Ruccolo, F. Canali, Long-term monitoring for the condition-based structural maintenance of the Milan Cathedral, Constr. Build. Mater. 228 (2019) 117101. doi:10.1016/j.conbuildmat.2019.117101.

[10] L.F. Ramos, P.B. Lourenço, G. De Roeck, A. Campos-Costa, Damage

identification in masonry structures with vibration measurements, Struct. Anal. Hist. Constr. Preserv. Saf. Significance - Proc. 6th Int. Conf. Struct. Anal. Hist. Constr. SAHC08. 1 (2008) 311–319. doi:10.1201/9781439828229.ch35.

[11] M. Dahak, N. Touat, M. Kharoubi, Damage detection in beam through change in measured frequency and undamaged curvature mode shape, Inverse Probl. Sci. Eng. 27 (2019) 89–114. doi:10.1080/17415977.2018.1442834.

[12] R. Brincker, P.H. Kirkegaard, J.P. Ulfkjaer, Damage Detection in laboratory concrete beams, 13th Int. Modal Anal. Conf. 1; (1995) 647–668.

[13] O. Yazdanpanah, S.M. Seyedpoor, H. Akbarzadeh Bengar, A new damage detection indicator for beams based on mode shape data, Struct. Eng. Mech. 53 (2015) 725–744. doi:10.12989/sem.2015.53.4.725.

[14] J.M. Ko, C.W. Wong, H.F. Lam, Damage detection in steel framed structures by vibration measurement approach, in: 12th Int. Modal Anal. Conf., 1994: pp. 280–286.

[15] C. Gentile, A. Saisi, Ambient vibration testing of historic masonry towers for structural identification and damage assessment, Constr. Build. Mater. (2007). doi:10.1016/j.conbuildmat.2006.01.007.

[16] N. Cavalagli, G. Comanducci, F. Ubertini, Earthquake-Induced Damage Detection in a Monumental Masonry Bell-Tower Using Long-Term Dynamic Monitoring Data, J. Earthq. Eng. 22 (2018) 96–119. doi:10.1080/13632469.2017.1323048.

[17] F. Ubertini, G. Comanducci, N. Cavalagli, A. Laura Pisello, A. Luigi Materazzi, F. Cotana, Environmental effects on natural frequencies of the San Pietro bell tower in Perugia, Italy, and their removal for structural performance assessment, Mech. Syst. Signal Process. (2017). doi:10.1016/j.ymssp.2016.05.025.

[18] M.G. Masciotta, L.F. Ramos, P.B. Lourenço, M. Vasta, Structural monitoring and damage identification on a masonry chimney by a spectral-based identification technique, Proc. Int. Conf. Struct. Dyn. , EURODYN. 2014-Janua (2014) 211–218.

[19] I. Venanzi, A. Kita, N. Cavalagli, L. Ierimonti, F. Ubertini, Earthquake-induced damage localization in an historic masonry tower through long-term dynamic monitoring and FE model calibration, Bull. Earthq. Eng. 18 (2020) 2247–2274.

doi:10.1007/s10518-019-00780-4.

[20] M.G. Masciotta, L.F. Ramos, M. Vasta, P.B. Lourenço, Extraction of damage-sensitive eigen-parameters for supervised SHM, Procedia Eng. 199 (2017) 2178–2183. doi:10.1016/j.proeng.2017.09.174.

[21] E. Bertolesi, M. Buitrago, E. Giordano, P.A. Calderón, J.J. Moragues, F. Clementi, J.M. Adam, Effectiveness of textile reinforced mortar (TRM) materials in preventing seismic-induced damage in a U-shaped masonry structure submitted to pseudo-dynamic excitations, Constr. Build. Mater. 248 (2020) 118532. doi:10.1016/j.conbuildmat.2020.118532.

[22] J. Daniell, Natural disasters since 1900: over 8 million deaths, 7 trillion US dollars, Sci. Dly. (2016) 1–5. https://phys.org/news/2016-04-natural-disasters-1900overmillion-deaths.html%0D.

[23] H.K. Hilsdorf, Investigation into the failure mechanism of brick masonry loaded in axial compression, FB Johnson (Gulf, Fluston, Tex.). (1969).

[24] Ministero delle Infrastrutture e dei Trasporti, DM 17/01/2018 - Aggiornamento delle “Norme Tecniche per le Costruzioni” (in italian), (2018) 1–198.

[25] Ministero delle infrastrutture e dei trasporti, Circolare 21 gennaio 2019 n. 7 C.S.LL.PP. Istruzioni per l’applicazione dell’aggiornamento delle “Norme Tecniche per le Costruzioni” di cui al D.M. 17/01/2018 (in Italian), Suppl. Ord. Alla G.U. n. 35 Del 11/2/19. (2019).

[26] EN 1996-1-1, Eurocode 6 - Design of masonry structures - Part 1-1: General rules for reinforced and unreinforced masonry structures, 2005.

[27] A. Giuffré, A Mechanical Model for Statics and Dynamics of Historical Masonry Buildings, in: Prot. Archit. Herit. Against Earthquakes, Springer Vienna, Vienna, 1996: pp. 71–152. doi:10.1007/978-3-7091-2656-1_4.

[28] P.B. Lourenço, Computational strategies for masonry structures, TUDelft, 1996. http://resolver.tudelft.nl/uuid:4f5a2c6c-d5b7-4043-9d06-8c0b7b9f1f6f.

[29] C. Wang, V. Sarhosis, N. Nikitas, Strengthening/Retrofitting Techniques on Unreinforced Masonry Structure/Element Subjected to Seismic Loads: A Literature Review, Open Constr. Build. Technol. J. 12 (2018) 251–268. doi:10.2174/1874836801812010251.

[30] M. Corradi, E. Speranzini, G. Bisciotti, Out-of-plane reinforcement of masonry walls using joint-embedded steel cables, Bull. Earthq. Eng. 18 (2020) 4755–4782. doi:10.1007/s10518-020-00875-3.

[31] M. Dolce, A. Cacosso, F. Ponzo, R. Marnetto, New Technologies for the Structural Rehabilitation of Masonry Constructions: Concept, Experimental Validation and Application of the CAM System, 2002.

[32] M. Corradi, A. Borri, G. Castori, R. Sisti, The Reticulatus method for shear strengthening of fair-faced masonry, Bull. Earthq. Eng. 14 (2016) 3547–3571. doi:10.1007/s10518-016-0006-5.

[33] Gibson, RF., Principles of composite material mechanics, McGraw-Hill, Inc, 1994.

[34] CNR-DT 200 R1/2013, Istruzioni per la Progettazione, l'Esecuzione ed il Controllo di Interventi di Consolidamento Statico mediante l'utilizzo di Compositi Fibrorinforzati (in italian), (2005).

[35] M. John, S. Thomas, Biofibres and biocomposites, Carbohydr. Polym. 71 (2008) 343–364. doi:10.1016/j.carbpol.2007.05.040.

[36] A. Lotfi, H. Li, D.V. Dao, G. Prusty, Natural fiber–reinforced composites: A review on material, manufacturing, and machinability, J. Thermoplast. Compos. Mater. (2019) 089270571984454. doi:10.1177/0892705719844546.

[37] CNR-DT200/2004, Istruzioni per la Progettazione, l'Esecuzione ed il Controllo di Interventi di Consolidamento Statico mediante l'utilizzo di Compositi Fibrorinforzati (in italian), (2005).

[38] L.C. Hollaway, A review of the present and future utilisation of FRP composites in the civil infrastructure with reference to their important in-service properties, Constr. Build. Mater. 24 (2010) 2419–2445. doi:10.1016/j.conbuildmat.2010.04.062.

[39] M. Motavalli, C. Czaderski, A. Schumacher, D. Gsell, Fibre reinforced polymer composite materials for building and construction, in: Text. Polym. Compos. Build., Elsevier, 2010: pp. 69–128. doi:10.1533/9780845699994.1.69.

[40] G. Croci, Strengthening the Basilica of St Francis of Assisi after the September 1997 Earthquake, Struct. Eng. Int. 11 (2001) 207–210. doi:10.2749/101686601780346869.

[41] S. De Santis, F.G. Carozzi, G. de Felice, C. Poggi, Test methods for Textile Reinforced Mortar systems, Compos. Part B Eng. 127 (2017) 121–132. doi:10.1016/j.compositesb.2017.03.016.

[42] M.A. Chiorino, Art and Science of Building in Concrete: The Work of Pier Luigi Nervi, in: Concr. Int. 34, 2012: pp. 32–40.

[43] G. de Felice, M.A. Aiello, C. Caggegi, F. Ceroni, S. De Santis, E. Garbin, N. Gattesco, Ł. Hojdys, P. Krajewski, A. Kwiecień, M. Leone, G.P. Lignola, C. Mazzotti, D. Oliveira, C. Papanicolaou, C. Poggi, T. Triantafillou, M.R. Valluzzi, A. Viskovic, Recommendation of RILEM Technical Committee 250-CSM: Test method for Textile Reinforced Mortar to substrate bond characterization, Mater. Struct. 51 (2018) 95. doi:10.1617/s11527-018-1216-x.

[44] B. Ghiassi, Mechanics and durability of lime-based textile reinforced mortars, RILEM Tech. Lett. 4 (2020) 130–137. doi:10.21809/rilemtechlett.2019.99.

[45] G. de Felice, T. D'Antino, S. De Santis, P. Meriggi, F. Roscini, Lessons Learned on the Tensile and Bond Behavior of Fabric Reinforced Cementitious Matrix (FRCM) Composites, Front. Built Environ. 6 (2020). doi:10.3389/fbuil.2020.00005.

[46] P. Bernardi, R. Cerioni, D. Ferretti, F. Leurini, E. Michelini, Experimental characterization of fiber-reinforced cementitious mortar under tension, Frat. Ed Integrità Strutt. 13 (2019) 97–104. doi:10.3221/IGF-ESIS.48.12.

[47] A. Dalalbashi, B. Ghiassi, D. Oliveira, Effect of Mortar Age on the Textile-to-Mortar Bond Behavior, in: XV Int. Conf. Durab. Build. Mater. Components. Eb. Proc., CIMNE, 2020. doi:10.23967/dbmc.2020.055.

[48] J. Donnini, V. Corinaldesi, A. Nanni, Mechanical properties of FRCM using carbon fabrics with different coating treatments, Compos. Part B Eng. 88 (2016) 220–228. doi:10.1016/j.compositesb.2015.11.012.

[49] M. Malena, G. de Felice, Debonding of composites on a curved masonry substrate: Experimental results and analytical formulation, Compos. Struct. 112 (2014) 194–206. doi:10.1016/j.compstruct.2014.02.004.

[50] S. De Santis, Bond behaviour of Steel Reinforced Grout for the extrados strengthening of masonry vaults, Constr. Build. Mater. 150 (2017) 367–382.

doi:10.1016/j.conbuildmat.2017.06.010.

[51] V. Alecci, M. De Stefano, F. Focacci, R. Luciano, L. Rovero, G. Stipo, Strengthening Masonry Arches with Lime-Based Mortar Composite, Buildings. 7 (2017) 49. doi:10.3390/buildings7020049.

[52] V. Alecci, F. Focacci, L. Rovero, G. Stipo, M. De Stefano, Intrados strengthening of brick masonry arches with different FRCM composites: Experimental and analytical investigations, Compos. Struct. 176 (2017) 898–909. doi:10.1016/j.compstruct.2017.06.023.

[53] V. Alecci, G. Misseri, L. Rovero, G. Stipo, M. De Stefano, L. Feo, R. Luciano, Experimental investigation on masonry arches strengthened with PBO-FRCM composite, Compos. Part B Eng. 100 (2016) 228–239. doi:10.1016/j.compositesb.2016.05.063.

[54] F.G. Carozzi, C. Poggi, E. Bertolesi, G. Milani, Ancient masonry arches and vaults strengthened with TRM, SRG and FRP composites: Experimental evaluation, Compos. Struct. 187 (2018) 466–480. doi:10.1016/j.compstruct.2017.12.075.

[55] N.H. Sadeghi, D. V Oliveira, R.A. Silva, N. Mendes, M. Correia, H. Azizi-bondarabadi, Performance of adobe vaults strengthened with LC-TRM: an experimental approach, in: Prot. Hist. Constr., Lisbon, Portugal, 2017.

[56] E. Bertolesi, B. Torres, J.M. Adam, P.A. Calderón, J.J. Moragues, Effectiveness of Textile Reinforced Mortar (TRM) materials for the repair of full-scale timbrel masonry cross vaults, Eng. Struct. 220 (2020) 110978. doi:10.1016/j.engstruct.2020.110978.

[57] L. Garcia-Ramonda, L. Pelá, P. Roca, G. Camata, In-plane shear behaviour by diagonal compression testing of brick masonry walls strengthened with basalt and steel textile reinforced mortars, Constr. Build. Mater. 240 (2020) 117905. doi:10.1016/j.conbuildmat.2019.117905.

[58] S. de Santis, G. de Felice, G.L. Di Noia, P. Meriggi, M. Volpe, Shake Table Tests on a Masonry Structure Retrofitted with Composite Reinforced Mortar, Key Eng. Mater. 817 (2019) 342–349. doi:10.4028/www.scientific.net/KEM.817.342.

[59] S. De Santis, P. Casadei, G. De Canio, G. de Felice, M. Malena, M. Mongelli, I. Roselli, Seismic performance of masonry walls retrofitted with steel reinforced

grout, Earthq. Eng. Struct. Dyn. 45 (2016) 229–251. doi:10.1002/eqe.2625.

[60] E. Grande, G. Milani, Numerical simulation of the tensile behavior of FRCM strengthening systems, Compos. Part B Eng. 189 (2020) 107886. doi:10.1016/j.compositesb.2020.107886.

[61] E. Bertolesi, F.G. Carozzi, G. Milani, C. Poggi, Numerical modeling of Fabric Reinforce Cementitious Matrix composites (FRCM) in tension, Constr. Build. Mater. 70 (2014) 531–548. doi:10.1016/j.conbuildmat.2014.08.006.

[62] F.S. Murgo, C. Mazzotti, Masonry columns strengthened with FRCM system: Numerical and experimental evaluation, Constr. Build. Mater. 202 (2019) 208–222. doi:10.1016/j.conbuildmat.2018.12.211.

[63] F. Valvona, J. Toti, V. Gattulli, F. Potenza, Effective seismic strengthening and monitoring of a masonry vault by using Glass Fiber Reinforced Cementitious Matrix with embedded Fiber Bragg Grating sensors, Compos. Part B Eng. 113 (2017) 355–370. doi:10.1016/j.compositesb.2017.01.024.

[64] G.P. Lignola, A. Bilotta, F. Ceroni, Assessment of the effect of FRCM materials on the behaviour of masonry walls by means of FE models, Eng. Struct. 184 (2019) 145–157. doi:10.1016/j.engstruct.2019.01.035.

[65] D. V. Oliveira, B. Ghiassi, Reza Allahvirdizadeh, X. Wang, G. Mininno, R.A. Silva, Macromodeling approach for pushover analysis of textile-reinforced mortar-strengthened masonry, in: Numer. Model. Mason. Hist. Struct., Elsevier, 2019: pp. 745–778. doi:10.1016/B978-0-08-102439-3.00021-X.

[66] X. Wang, B. Ghiassi, D. V. Oliveira, C.C. Lam, Modelling the nonlinear behaviour of masonry walls strengthened with textile reinforced mortars, Eng. Struct. 134 (2017) 11–24. doi:10.1016/j.engstruct.2016.12.029.

[67] A. Monaco, G. Minafò, J. D'Anna, M.C. Oddo, L. La Mendola, Constitutive Numerical Model of FRCM Strips Under Traction, Front. Built Environ. 6 (2020). doi:10.3389/fbuil.2020.00060.

[68] C.B. de Carvalho Bello, A. Cecchi, E. Meroi, D. V. Oliveira, Experimental and Numerical Investigations on the Behaviour of Masonry Walls Reinforced with an Innovative Sisal FRCM System, Key Eng. Mater. 747 (2017) 190–195. doi:10.4028/www.scientific.net/KEM.747.190.

[69] J. Scacco, B. Ghiassi, G. Milani, P.B. Lourenço, A fast modeling approach for numerical analysis of unreinforced and FRCM reinforced masonry walls under out-of-plane loading, Compos. Part B Eng. 180 (2020) 107553. doi:10.1016/j.compositesb.2019.107553.

[70] C. D'Ambra, G.P. Lignola, A. Prota, E. Sacco, Comparison of Different FE Modeling for In-Plane Shear Strengthening of Brittle Masonry with FRCM, Key Eng. Mater. 817 (2019) 65–72. doi:10.4028/www.scientific.net/KEM.817.65.

[71] E. Ricci, D. V. Oliveira, E. Sacco, B. Ghiassi, Modelling of masonry arches strengthened at extrados with FRCM, in: 10th IMC, Milan, 2018.

[72] G. Mazzucco, T. D'Antino, C. Pellegrino, V. Salomoni, Three-dimensional finite element modeling of inorganic-matrix composite materials using a mesoscale approach, Compos. Part B Eng. 143 (2018) 75–85. doi:10.1016/j.compositesb.2017.12.057.

[73] F.G. Carozzi, G. Milani, C. Poggi, Mechanical properties and numerical modeling of Fabric Reinforced Cementitious Matrix (FRCM) systems for strengthening of masonry structures, Compos. Struct. 107 (2014) 711–725. doi:10.1016/j.compstruct.2013.08.026.

[74] M. Basili, G. Marcari, F. Vestroni, Nonlinear analysis of masonry panels strengthened with textile reinforced mortar, Eng. Struct. 113 (2016) 245–258. doi:10.1016/j.engstruct.2015.12.021.

[75] A. Garofano, F. Ceroni, M. Pecce, Modelling of the in-plane behaviour of masonry walls strengthened with polymeric grids embedded in cementitious mortar layers, Compos. Part B Eng. 85 (2016) 243–258. doi:10.1016/j.compositesb.2015.09.005.

[76] G. Ramaglia, G.P. Lignola, A. Balsamo, A. Prota, G. Manfredi, Seismic Strengthening of Masonry Vaults with Abutments Using Textile-Reinforced Mortar, J. Compos. Constr. 21 (2017) 04016079. doi:10.1061/(ASCE)CC.1943-5614.0000733.

[77] M.G. Masciotta, Damage Identification of Structures based on Spectral Output Signals Trabalho efectuado sob a orientação do, (2015).

[78] O.S. Salawu, Detection of structural damage through changes in frequency: a review, Eng. Struct. 19 (1997) 718–723.

[79] R. Hou, Y. Xia, Review on the new development of vibration-based damage identification for civil engineering structures: 2010–2019, J. Sound Vib. 491 (2021) 115741. doi:10.1016/j.jsv.2020.115741.

[80] N. Cavalagli, A. Kita, V.L. Castaldo, A.L. Pisello, F. Ubertini, Hierarchical environmental risk mapping of material degradation in historic masonry buildings: An integrated approach considering climate change and structural damage, Constr. Build. Mater. 215 (2019) 998–1014. doi:10.1016/j.conbuildmat.2019.04.204.

[81] P. Cawley, R.D. Adams, The location of defects in structures from measurements of natural frequencies, J. Strain Anal. Eng. Des. 14 (1979) 49–57. doi:10.1243/03093247V142049.

[82] Y. Narkis, Identification of crack location in vibrating simply supported beams, J. Sound Vib. 172 (1994) 549–558. doi:10.1006/jsvi.1994.1195.

[83] J.M.. Silva, G. A.J.M.A, Crack identification of simple structural elements through the use of natural frequency variations: the inverse problem, in: Proc. 12th Int. Modal Anal. Conf., 1994: pp. 1728–1735.

[84] A. Messina, E.J. Williams, T. Contursi, Structural damage detection by a sensitivity and statistical-based method, J. Sound Vib. 216 (1998) 791–808.

[85] J.T. Kim, N. Stubbs, Crack detection in beam-type structures using frequency data, J. Sound Vib. 259 (2003) 145–160.

[86] D.J. Ewins, Modal testing: theory and practice, J. Vib. Acoust. Stress Reliab. Des. (1986).

[87] C. Dong, P.Q. Zhang, W.Q. Feng, T.C. Huang, The sensitivity study of the modal parameters of a cracked beam, in: Proc. 12th Int. Modal Anal. Conf., Honolulu, HI, 1994: pp. 98–104.

[88] A.K. Pandey, M. Biswas, M.M. Samman, Damage detection from changes in curvature mode shapes, J. Sound Vib. 145 (1991) 321–332.

[89] N. Stubbs, J.T. Kim, K. Topole, An efficient and robust algorithm for damage localization in offshore platforms, in: Proc. ASCE 10th Struct. Congr., 1992: pp. 543–546.

[90] M.M. Abdel Wahab, G. De Roeck, Damage detection in bridges using modal

curvatures: Application to a real damage scenario, J. Sound Vib. 226 (1999) 217–235. doi:10.1006/jsvi.1999.2295.

[91] A.K. Pandey, M. Biswas, Damage detection in structures using changes in flexibility, J. Sound Vib. 145 (1994) 321–332.

[92] Y. Zhang, L. Wang, Z. Xiang, Damage detection by mode shape squares extracted from a passing vehicle, J. Sound Vib. 331 (2012) 291–307. doi:10.1016/j.jsv.2011.09.004.

[93] S.H. Sung, H.J. Jung, H.Y. Jung, Damage detection for beam-like structures using the normalized curvature of a uniform load surface, J. Sound Vib. 332 (2013) 1501–1519. doi:10.1016/j.jsv.2012.11.016.

[94] F. Bianconi, G.P. Salachoris, F. Clementi, S. Lenci, A Genetic Algorithm Procedure for the Automatic Updating of FEM Based on Ambient Vibration Tests, Sensors. 20 (2020) 3315. doi:10.3390/s20113315.

[95] G. Standoli, E. Giordano, G. Milani, F. Clementi, Model Updating of Historical Belfries Based on Oma Identification Techniques, Int. J. Archit. Herit. (2020) 1–25. doi:10.1080/15583058.2020.1723735.

[96] E. Giordano, F. Clementi, A. Barontini, M. Giovanna, E. Chatzi, F. Luís, Damage detection and optimal sensor placement in health monitoring of " Collegiata di Santa Maria " in Visso (Central Italy) Damage detection and optimal sensor placement in health monitoring of " Collegiata di Santa Maria " in Visso (Central Italy), (2019) 44–53.

[97] I. Venanzi, A. Kita, N. Cavalagli, L. Ierimonti, F. Ubertini, Continuous OMA for Damage Detection and Localization in the Sciri tower in Perugia, Italy, in: IOMAC – Int. Oper. Modal Anal. Conf. 2019At Copenhagen, Denmark, Copenhagen, Denmark, 2019.

[98] A. Cabboi, C. Gentile, A. Saisi, From continuous vibration monitoring to FEM-based damage assessment: Application on a stone-masonry tower, Constr. Build. Mater. 156 (2017) 252–265. doi:10.1016/j.conbuildmat.2017.08.160.

[99] Consiglio Superiore dei Lavori Pubblici, Linea Guida per la identificazione, la qualificazione ed il controllo di accettazione di compositi fibrorinforzati a matrice inorganica (FRCM) da utilizzarsi per il consolidamento strutturale di costruzioni

esistenti, (2018) 43.

[100] Recommendation of RILEM TC 232-TDT: test methods and design of textile reinforced concrete, Mater. Struct. 49 (2016) 4923–4927. doi:10.1617/s11527-016-0839-z.

[101] Midas FEA NX, Analysis reference, (2020).

[102] Comité euro-international du béton, Thomas Telford Ltd, CEB-FIP Model Code 90, Thomas Telford Ltd. (1993) 460.

[103] EN 14580. Natural stone test methods. Determination of the static elastic moduls, (2005).

[104] EN 13412. Products and systems for the protection and repair of concrete structures - Test methods - Determination of modulus of elasticity in compression, (2008).

[105] EN 1015-11. Methods of test for mortar for masonry Determination of flexural and compressive strength of hardened mortar, (1999).

[106] MAPEI, (2018) http://www.mapei.com/.

[107] T. Rotunno, M. Fagone, E. Bertolesi, E. Grande, G. Milani, Single lap shear tests of masonry curved pillars externally strengthened by CFRP strips, Compos. Struct. 200 (2018) 434–448. doi:10.1016/j.compstruct.2018.05.097.

[108] D. Bru, S. Ivorra, M. Buitrago, E. Bertolesi, M. Buitargo, E. Bertolesi, Oma identification on a scaled masonry building pre and post reinforced with TRM, in: 8th IOMAC, Copenhagen, 2019: pp. 1–8.

[109] P.X. Candeias, A. Campos Costa, N. Mendes, A.A. Costa, P.B. Lourenço, Experimental Assessment of the Out-of-Plane Performance of Masonry Buildings Through Shaking Table Tests, Int. J. Archit. Herit. 11 (2017) 31–58. doi:10.1080/15583058.2016.1238975.

[110] A. Kita, N. Cavalagli, M.G. Masciotta, P.B. Lourenço, F. Ubertini, Earthquake-induced damage localization through non-linear dynamic analysis, in: COMPDYN 2015, Institute of Structural Analysis and Antiseismic Research School of Civil Engineering National Technical University of Athens (NTUA) Greece, Athens, 2019: pp. 1272–1289. doi:10.7712/120119.6996.18844.

[111] H.D. Hibbitt, A simplified model for concrete at low confining pressures, Nucl. Eng. Des. 104 (1987) 313–320. doi:10.1016/0029-5493(87)90209-3.

[112] E. Giordano, F. Clementi, A. Nespeca, S. Lenci, Damage Assessment by Numerical Modeling of Sant'Agostino's Sanctuary in Offida During the Central Italy 2016–2017 Seismic Sequence, Front. Built Environ. 4 (2019). doi:10.3389/fbuil.2018.00087.

[113] P.B. Lourenço, Structural masonry analysis : recent developments and prospects, in: University of Newcastle (Ed.), Australia, 2008.

[114] N. Ismail, J.M. Ingham, In-plane and out-of-plane testing of unreinforced masonry walls strengthened using polymer textile reinforced mortar, Eng. Struct. 118 (2016) 167–177. doi:10.1016/j.engstruct.2016.03.041.

[115] E. Giordano, N. Mendes, M.G. Masciotta, F. Clementi, N.H. Sadeghi, R.A. Silva, D. V. Oliveira, Expeditious damage index for arched structures based on dynamic identification testing, Constr. Build. Mater. 265 (2020) 120236. doi:10.1016/j.conbuildmat.2020.120236.

[116] N.H. Sadeghi, Conservation and Safety Assessment of Vaulted Adobe Architecture in Yazd , Iran., University of Minho, Portugal, 2018.

[117] O.P.C.M. 3431/5, Primi elementi in materia di criteri generali per la classificazione sismica del territorio nazionale e di normative tecniche per le costruzioni in zona sismica [in Italian].). First elements on general criteria for the seismic classification of the nati, (2005).

[118] N. H. Sadeghi, D. V. Oliveira, M. Correia, H. Azizi-Bondarabadi, A. Orduña, Seismic performance of historical vaulted adobe constructions: a numerical case study from Yazd, Iran, Int. J. Archit. Herit. 12 (2018) 879–897. doi:10.1080/15583058.2017.1422573.

[119] ARTeMIS Modal, Structural Vibration Solutions A/S, (2018).

[120] British Standard Institution, BS 1881:Part 121, Method for determination of static modulus of elasticity in compression, (1997).

[121] ASTM C469/C469M, Standard Test Method for Static Modulus of Elasticity and Poisson's Ratio of Concrete in Compression, Astm C469/C469M. (2014) 1–5. doi:10.1520/C0469.

[122] GB/T50081-2002, Standard for tests method of mechanical properties on ordinary concrete, Minist. House Urban-Rulal Dev. People's Repub. China, China. (2002).

[123] S. Lenci, Q. Piattoni, F. Clementi, T. Sadowski, An experimental study on damage evolution of unfired dry earth under compression, Int. J. Fract. 172 (2011) 193–200. doi:10.1007/s10704-011-9651-5.

[124] S. Lenci, F. Clementi, Simple mechanical model of curved beams by a 3D approach, J. Eng. Mech. 135 (2009) 597–613. doi:10.1061/(ASCE)0733-9399(2009)135:7(597).

[125] J. Kubica, Proposition of stiffness reduction in analysis of clay brick masonry under cyclic/seismic loads, J. Meas. Eng. 6 (2018) 226–233. doi:10.21595/jme.2018.20417.

[126] DIANA, User's maual, (2019).

[127] B.M. Douglas, W.H. Reid, Dynamic tests and system identification of bridges, J. Struct. Div. 108 (1982) 2295–12.

[128] R.A. Silva, N. Mendes, D. V. Oliveira, A. Romanazzi, O. Domínguez-Martínez, T. Miranda, Evaluating the seismic behaviour of rammed earth buildings from Portugal: From simple tools to advanced approaches, Eng. Struct. 157 (2018) 144–156. doi:10.1016/j.engstruct.2017.12.021.

[129] Q.-B. Bui, J.-C. Morel, Assessing the anisotropy of rammed earth, Constr. Build. Mater. 23 (2009) 3005–3011. doi:10.1016/j.conbuildmat.2009.04.011.

[130] R. Illampas, R.A. Silva, D.C. Charmpis, P.B. Lourenço, I. Ioannou, Validation of the repair effectiveness of clay-based grout injections by lateral load testing of an adobe model building, Constr. Build. Mater. 153 (2017) 174–184. doi:10.1016/j.conbuildmat.2017.07.054.

[131] D. Silveira, H. Varum, A. Costa, T. Martins, H. Pereira, J. Almeida, Mechanical properties of adobe bricks in ancient constructions, Constr. Build. Mater. 28 (2012) 36–44. doi:10.1016/j.conbuildmat.2011.08.046.

[132] E. Giordano, F. Clementi, G. Cocchi, L. Marcheggiani, On the nonlinear behaviour of unfired dry earth, in: 2019: p. 100007. doi:10.1063/1.5138013.

[133] P.B. Lourenço, Recent advances in masonry modelling: micromodelling and

homogenisation, in: Multiscale Model. Solid Mech. Comput. Approaches, 2009: pp. 251–294. doi:10.1142/9781848163089_0006.

[134] N. Mendes, P.B. Lourenço, Sensitivity analysis of the seismic performance of existing masonry buildings, Eng. Struct. 80 (2014) 137–146. doi:10.1016/j.engstruct.2014.09.005.